

2015 | Faculty of Sciences

DOCTORAL DISSERTATION

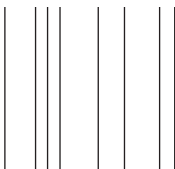
Advanced Scanning Probe Microscopy for Novel Generation Solar Cells

Doctoral dissertation submitted to obtain the degree of
Doctor of Science: Physics, to be defended by

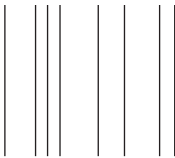
Jeroen Drijkoningen

Promoter: Prof. Dr Jean Manca | UHasselt

Co-promoter: Prof. Dr Jan D'Haen | UHasselt



D/2015/2451/02



Jury

Chair:	Prof. dr. K. Coninx Dean Faculty of Science Universiteit Hasselt
Promotor:	Prof. dr. J. Manca Universiteit Hasselt
Co-promotor:	Prof. dr. J. D'Haen Universiteit Hasselt
Members of the jury:	Prof. dr. W. De Ceuninck Universiteit Hasselt
	dr. ir. J.C. Bolsée
	dr. E. Bourgeois Universiteit Hasselt
	dr. ir. O. Douhéret Materia Nova Université de Mons
	dr. F. Piersimoni Universität Potsdam

Dankwoord

'Learn from yesterday, live for today, hope for tomorrow. The important thing is to not stop questioning.'

Albert Einstein

Dit citaat is voor mij een perfecte beschrijving van een doctoraat. Leer van de fouten van gisteren, leef voor de experimenten van vandaag en hoop dat ze morgen beter gaan. Maar voornamelijk, blij jezelf vragen stellen. Hierbij wil ik dan ook in eerste instantie mijn promotor, Jean, bedanken om me de mogelijkheid te geven om een doctoraat aan te vatten. Gedurende de voorbije vier jaren heb je me continu verbaasd met een niet eindigend optimisme met als resultaat dat ik na geen enkele vergadering slecht gezind vertrok.

De volgende persoon die ik hier wil bedanken is mijn co-promotor, Jan D'Haen. Jan, je hebt me bijgebracht wat het is om een kritische wetenschapper te zijn en om continue alle resultaten in vraag te stellen. Ook ben je er altijd in geslaagd om met een frisse blik op mijn (wetenschappelijke) vragen in te spelen. Geen monster was er teveel aan om "even rap in de SEM te steken" en te analyseren.

Mijn directe bureaugenoten Lien en Ilaria voor de aangename sfeer en gesprekken over vervallen muffins, de belangrijke verschillen in de te gebruiken koffiemaling voor espresso en koffie, dit zowel in de koffiekamer als op onze bureau. Dat brengt me dan bij mijn vorige bureaugenoten: Donato en Fortunato, you guys were always ready for a proper coffee with almond milk and conversations about Berlusconi and in general Italian pol-

itics.

Another former colleague always ready to initiate a conversation about (Belgian) politics is Jean Christophe, who I have to thank for the initiation in the field of atomic force microscopy.

Dat brengt me bij mijn huidige collega's in de ONE² groep. Tim hou je eeuwige optimisme, het is iets wat ik heb geapprecieerd gedurende de tijd die we samen hebben gewerkt. Koen, Jeroen en Glen, jullie zorgen off- en online altijd voor een vrolijke noot! Bert, van jouw werkethiek blijf ik onder de indruk, de nauwgezetheid die jij aan de dag legt is niet te onderschatten. Wouter, we hebben gelijk gestudeerd zowel in Diepenbeek als in Leuven, ook het doctoraat hebben we gelijk aangevat en nu leggen we samen af, over heel die periode ben ik onder de indruk geraakt van de motivatie die jij in werk en sport kan steken. Dat brengt me dan bij Sabine en Wim Deferme, altijd stond de deur van jullie bureau open voor raad en daad.

Van mijn andere collega's over de verschillende groepen is er één uitschieter, Wim Dexters. Wim, als ik terugdenk over de periode dat ik je ken dan kan ik er enkele legendarische avonden uithalen, maar je hebt er vooral voor gezorgd dat er altijd iemand was waar ik even tegen kon ventileren over alles en nog wat.

Als ik het heb over andere groepen, dan kan ik Jurgen ook niet vergeten. Als link tussen synthese en karakterisatie heb ik veel van je geleerd de voorbije vier jaar over o.a. polymeerchemie.

Jan en Lieven, jullie kunde en kennis is me gedurende mijn doctoraat zeker van pas gekomen wanneer ik weer eens een vraag had over LabView of wanneer ik een nieuwe sensorsetup nodig had aan de AFM. Natuurlijk kan ik Erik dan ook niet vergeten aangezien ik geregeld al wel eens kwam vragen of het niet mogelijk was om een grotere harde schijf of meer RAM geheugen in mijn computer te krijgen.

Christel en Hilde, ook jullie twee waren onontbeerlijk. Altijd klaar om monsters te prepareren voor de SEM of om bestellingen van AFM tips in goede banen te leiden.

En als we het toch hebben over de dagelijkse werking op het IMO: Johnny, hoe slaag je er continu in om iedereen zo goed te helpen? Een vallende kapstop of een nieuw vacuumsysteem met lek, altijd sta je klaar.

Kathia, la risa es el mejor remedio! I really enjoyed talking with you, you are always smiling and never in a bad mood. Bart, niet direct de persoon waar ik van gehoopt/gedacht had een bed mee te delen, maar je laat de dame in het gezelschap in één bed slapen en de heren met 2. Marloes, in Boston heb ik je van een andere kant leren kennen, het gaat je goed in Londen! Aan de rest van de Bios groep (Kasper, Matthias, Stijn) het waren aangename tijden met jullie op het IMO.

Van de leden van de WBGM groep steekt buiten Wim natuurlijk Sien er bovenuit. Dankjewel om naar mijn gebazel over wetenschap en alles anders te luisteren en om er tegenin te gaan wanneer nodig.

Wiebke, thanks for keeping me updated on all the different steps in the run up to the PhD defense.

Aan alle andere (niet bij naam genoemde) collega's, dankjewel voor de aangename sfeer tijdens mijn doctoraat. Ik heb werkelijk genoten van alle activiteiten en gesprekken.

Ook mijn ouders mag ik niet vergeten, dankjewel om me al die jaren te steunen gedurende mijn studies. Zonder jullie was dit zo goed als onmogelijk geweest.

Kiwi, dankje om er voor me te zijn, ook aan jou heb ik enorm veel steun gehad gedurende de voorbije twee jaren.

Jeroen

Nederlandstalige

Samenvatting

De huidige en nieuwe generatie organische en hybride zonnecellen hebben een gigantisch potentieel, niet alleen in kost reductie maar ook in mogelijke toepassingen. Echter, om een brede toepasbaarheid te bereiken dienen niet alleen nieuwe materialen ontwikkeld maar ook relevante en fysische parameters die bijdragen aan een hoge efficiëntie en stabiliteit gekarakteriseerd te worden. Een belangrijke parameter is de lokale morfologie en de bijhorende lokale elektrische eigenschappen. Om deze nanoschaal karakterisatie mogelijk te maken werd gebruik gemaakt van atomaire kracht microscopie en bijhorende afgeleide technieken zoals geleidende atomaire kracht microscopie en oppervlakte potentiaal microscopie. Hiertoe is dit werk verdeeld in verschillende onderdelen.

In een eerste stap proberen we te verklaren wat men juist meet met KPFM en C-AFM. De opgemeten data insinueert dat de oppervlakte potentiaal zoals gemeten met KPFM zeer sterk gerelateerd is aan het HOMO niveau van het polymeer. Deze analyse laat ons toe om de opgemeten oppervlakte potentiaal te interpreteren als een intrinsieke barrière tussen tip en monster. Stroom spannings curves zoals opgemeten met geleidende AFM tonen dan aan dat indien de barrière tussen tip en monster niet te groot is dit verloopt volgens "SCLC" gedrag echter, wanneer de barrière te groot wordt gaat de stroom zich volgens een Poole-Frenkel type contact gedragen. Ter controle werden stroom spanningscurves opgemeten op andere

polymeren ook uitgezet en blijkt dat deze ook het voorop genoemde gedrag vertonen.

In een tweede stap werden hoog efficiënte polymer zonnecellen gecreëerd door gebruik te maken van ionische tussenlagen. Deze werden verder gekarakteriseerd met behulp van atomaire kracht microscopie, uit deze meting bleek dat de gebruikte tussenlagen de actieve laag van de zonnecel niet volledig bedekken maar toch resulteren in een verhoging van de efficiëntie. Een diepere karakterisatie met geleidende AFM en belichte KPFM leert ons dat de best presterende interlaag niet alleen gaten transport tegengaat maar ook zorgt voor elektrontransport.

In een derde stuk passen we geleidende AFM toe op een nieuwe generatie van zonnecellen, namelijk perovskieten. Deze metingen tonen duidelijk aan dat in het geval van op lood halide gebaseerde perovskieten de korrelgrenzen niet geleidend zijn terwijl de korrels zelf zeer goed geleiden. Uit KPFM belicht en onbelicht volgt dat sommige korrelgrenzen actief zijn, terwijl de meeste echter geen speciaal effect onder licht vertonen. Een analyse van de lokale stroom spanningskarakteristieken toont aan dat deze te verklaren zijn door ladingsopbouw aan het raakvlak tussen de perovskietlaag en het titaanoxide.

In het laatste onderdeel werd KPFM toegepast om de degradatie van calcium/aluminium contacten in organische zonnecellen te bestuderen en te verklaren. Hiertoe werden polymeerzonnecellen geprepareerd met contact en zonder contact en hierna opgewarmd op relatief hoge temperaturen voor korte tijden. Door cellen uit deze twee experimenten te vergelijken werd duidelijk dat de degradatie voornamelijk beperkt bleef tot de contacten. De cellen opgewarmd met contact werden opgemeten met KPFM en vertoonden een lokale vervorming van het contact en een bijhorende stijging in oppervlakte potentiaal. Metingen gebruik makend van een elektronenbundel toonden aan dat de lokale vervorming van het contact te verklaren is door een (lokale) verdunning van het aluminium en mogelijks diffusie van het calcium in het aluminium.

Publications and Conference contributions

Publications

1. F. Piersimoni, G. Degutis, S. Bertho, K. Vandewal, D. Spoltore, T. Vangerven, **J. Drijkoningen**, M. K. Van Bael, A. Hardy, J. D'Haen, W., D. Vanderzande, M. Nesladek, J. Manca
Journal of Polymer Science Part B: Polymer Physics, **51** (16), 1209-1214 (2013).
2. J. Kesters, T. Ghooos, H. Penxten, **J. Drijkoningen**, T. Vangerven, D. M. Lyons, B. Verreet, T. Aernouts, L. Lutsen, D. Vanderzande, J. Manca, W. Maes.
Advanced Energy Materials, **3** (9), 1180-1185 (2013).
3. W. Maes, T. Ghooos, J. Kesters, **J. Drijkoningen**, W. Vanormelingen, O. Malinkiewicz, H.J. Bolink, L. Lutsen, J. Manca, D. Vanderzande
SPIE Organic Photonics + Electronics, (2013).

4. W. Vanormelingen, J. Kesters, P. Verstappen, **J. Drijkoningen**, J. Kudrjasova, S. Koudjina, V. Liégeois, B. Champagne, J. Manca, L. Lutsen, D. Vanderzande, W. Maes
Journal of Materials Chemistry A **2** (20), 7535-7545 (2014).
5. **J. Drijkoningen**, J. Kesters, T. Vangerven, E. Bourgeois, L. Lutsen, D. Vanderzande, W. Maes, J. D'Haen, J. Manca
Organic Electronics **15** (6), 1282-1289 (2014).
6. P. Robaeys, F. Bonaccorso, E. Bourgeois, J. D'Haen, W. Dierckx, W. Dexters, D. Spoltore, **J. Drijkoningen**, J. Liesenborgs, A. Lombardo, A. C. Ferrari, F. Van Reeth, K. Haenen, J. Manca, M. Nesladek
Applied Physics Letters **105** (8), 083306 (2014).
7. B. Z. Tedlla, F. Zhu, M. Cox, **J. Drijkoningen**, J. Manca, B. Koopmans, E. Goovaerts
Advanced Energy Materials (2014), accepted for publication.
8. H. Damm, P. Adriaensens, C. De Dobbelaere, B. Capon, K. Elen, **J. Drijkoningen**, B. Conings, J. Manca, J. D'Haen, C. Detavernier, P. C.M.M. Magusin, J. Hadermann, A. Hardy, M. K. Van Bael
Chemistry of Materials **26** (20), 5839-5851 (2014).
9. M. Buffiere, A. E. Zaghi, N. Lenaers, M. Batuk, S. Khelifi, **J. Drijkoningen**, J. Hamon, A. Stesmans, J. Kepa, V. V. Afanas'ev, J. Hadermann, J. D'Haen, J. Manca, J. Vleugels, M. Meuris, J. Poortmans
The Journal of Physical Chemistry C (2014), accepted for publication.

Conference contributions

1. J. Kesters, T. Ghooos, **J. Drijkoningen**, T. Vangerven, B. Verreet, T. Aernouts, L. Lutsen, D. Vanderzande, J. Manca and W. Maes. Efficiency enhancement by incorporation of imidazolium-substituted polythiophenes as electron transport layers in organic photovoltaics (Hybrid and organic photovoltaics 2013 - Seville, Spain)
2. J. Kesters, **J. Drijkoningen**, T. Vangerven, B. Verreet, T. Aernouts, L. Lutsen, D. Vanderzande, J. Manca and W. Maes. Imidazolium-substituted Polythiophenes as Efficient Electron Transport Materials Improving Photovoltaic Performance. (Belgian Polymer Group 2013 - Houffalize, Belgium)
3. **J. Drijkoningen**, J. Kesters, L. Lutsen, D. Vanderzande, W. Maes, J. D'haen and J. Manca. Advanced SPM characterization of novel interlayers as efficiency enhancing layers for bulk heterojunction solar cells (Next-Generation Organic Photovoltaics 2013 - Groningen, Netherlands)
4. **J. Drijkoningen**, J. Kesters, L. Lutsen, D. Vanderzande, W. Maes, J. D'haen and J. Manca. Probing the Morphological and Electrical Properties of Efficiency Enhancing Interlayers for BHJ Solar Cells by Advanced SPM Techniques (MRS 2013 - Boston, USA)
5. J. Kesters, **J. Drijkoningen**, T. Vangerven, B. Verreet, T. Aernouts, L. Lutsen, D. Vanderzande, J. Manca and W. Maes. Efficiency enhancement of organic photovoltaics by incorporation of interfacial layers. (MRS 2014 - San Francisco, USA)

6. J. Kesters, **J. Drijkoningen**, T. Vangerven, B. Verreet, T. Aernouts, L. Lutsen, D. Vanderzande, J. Manca and W. Maes. Efficiency enhancement of organic photovoltaics by incorporation of interfacial layers (Koninklijke Vlaamse Chemische Vereniging 2014 - Blankenberge, Belgium)
7. M. Buffiere, A.E. Zaghi, N. Lenaers, M. Batuk, S. Khelifi, **J. Drijkoningen**, V. Afanasiev, J. Kepa, A. Stesmans, J. Hadermann, J. D'Haen, J. Manca, J. Vleugels, M. Meuris and J. Poortmans. Influence of the binder content on the properties of printed CuInSe₂ solar cells (E-MRS 2014 - Strasbourg, France)

Poster contributions

1. M. Van Gompel, K. Schellens, **J. Drijkoningen**, M.K. Van Bael and P. Wagner. Towards an alternative for ITO: electrical properties of aluminium doped zinc oxide. (Belgian Physical Society 2011, Namur)
2. **J. Drijkoningen**, J. Kesters, L. Lutsen, D. Vanderzande, W. Maes, J. D'haen and J. Manca. Advanced nanoscale characterization of novel interlayers as efficiency enhancing layers for bulk heterojunction organic solar cells. (Orion Summer school 2013, Granada)
3. J. Kesters, T. Ghooos, **J. Drijkoningen**, T. Vangerven, B. Verreet, T. Aernouts, L. Lutsen, D. Vanderzande, J. Manca and W. Maes. High efficient organic photovoltaics by incorporation of an imidazolium-substituted conjugated polyelectrolyte. (Orion Summer school 2013, Granada)
4. M. Van Gompel, J. D'Haen, **J. Drijkoningen**, M.K. Van Bael and P. Wagner. Preparation of thin films of the transparent conductive oxide

Al:ZnO by reactive high-pressure sputtering in Ar/O₂ mixtures. (Engineering of Functional Interfaces 2013, Hasselt)

5. K.L. Jiménez-Monroy, **J. Drijkoningen**, J.P. Noben, D. Cortens, G. Degutis, P.Losada-Pérez, A.Y. Atalay, J. Manca, H.-G. Boyen, P. Wagner. Electrical characterization of molecular wires based on DNA (ENFI 2014, Aachen)

6. K.L. Jiménez-Monroy, **J. Drijkoningen**, D. Cortens, P.Losada-Pérez, A.Y. Atalay, J. Manca, P. Wagner. DNA electrical behavior at room temperature: I-V measurements on single molecules. (Belgian Physical Society 2014, Leuven)

Contents

Dankwoord	ii
Nederlandstalige Samenvatting	vi
Publications and Conference contributions	ix
Glossary	xix
I Research context and goals	1
1 Introduction	3
1.1 Renewable Energy	3
1.2 The development and applications of photovoltaics	6
1.3 Goal and structure of the thesis	8
1.3.1 Goal of the thesis	8
1.3.2 Structure of the thesis	10
Bibliography	11
2 (Organic) semiconductors for photovoltaic conversion	15
2.1 Working Principle	15
2.2 Charge injection and transport in organic thin films	19
2.2.1 Schottky emission	19
2.2.2 Poole Frenkel	20
2.2.3 Fowler-Nordheim Tunneling	21

2.2.4 Direct Tunneling	21
2.2.5 Space charge limited current	22
2.2.6 Ohmic conduction	22
2.2.7 Ionic conduction	23
2.3 The need for nanoscale characterization	23
Bibliography	27
3 Characterization techniques	33
3.1 Introduction	33
3.2 Basic Characterization Techniques	33
3.2.1 Dektak	33
3.2.2 Current-Voltage measurements	34
3.2.3 EQE	36
3.2.4 Proton NMR	36
3.3 Atomic Force Microscopy	37
3.3.1 Contact and Conductive AFM	38
3.3.2 Dynamic AFM	40
3.3.3 KPFM	41
3.3.4 PeakForce Tapping and TUNA	44
Bibliography	48
II Results and discussion	51
4 Results and Discussion	53
4.1 Charge injection and extraction in Polymer/Donor:acceptor blends	53
4.1.1 Introduction	53
4.1.2 Determining the tip/sample barrier for injection	54
4.1.3 Conduction mechanisms for pure films and blends	62
4.1.4 The effect of PEDOT:PSS on the local conduction	67
4.1.5 Conclusions	73
4.2 Scanning Probe Microscopy for interlayer characterization	74

<i>CONTENTS</i>	xvii
4.2.1 Introduction	74
4.2.2 Imidazolium-substituted polythiophenes as efficient electron transport materials	74
4.2.3 Thickness effect	83
4.2.4 Morphology and mechanical properties	88
4.2.5 PeakForce TUNA and Conductive AFM	90
4.2.6 KPFM	92
4.2.7 Conclusions	97
4.3 Advanced scanning probe microscopy for perovskite based solar cells	98
4.4 Visualizing thermally and atmospheric induced degradation of the cathode in polymer solar cells	107
4.4.1 Introduction	107
4.4.2 Results and Discussion	108
4.4.3 Conclusions	123
Bibliography	124
III Conclusions & Outlook	137
5 Conclusions and Future Work	139
5.1 Conclusions	139
5.2 Future Work	141
5.2.1 C-AFM on blends	141
5.2.2 Interlayers	141
5.2.3 SPM and Perovskites	142
5.2.4 Contact degradation	142
5.2.5 Illuminated KPFM	142
IV Appendix	143
Bibliography	151

Glossary

η	power conversion efficiency
AFM	atomic force microscopy
AM-AFM	amplitude modulated atomic force microscopy
AM-KPFM	amplitude modulated KPFM
AM1.5	air mass 1.5
BHJ	bulk heterojunction
C ₆₀	buckminsterfullerene
C-AFM	conductive atomic force microscopy
CH ₃ NH ₃ PbI _{3-x} Cl _x	methylammonium lead tri-iodide/chloride
CIGS	copper indium gallium sulphur/selenium
CPE	conjugated polyelectrolyte
CuPc	copper phthalocyanine
CZTS	copper zinc tin sulphur/selenium
D/A Interface	donor - acceptor interface
DMT	Darjaguin-Muller-Toporov
DTTzTz	2,5-dithienylthiazolo[5,4-d]thiazole
EBIC	electron beam induced current
EDX	energy dispersive X-ray spectroscopy
EQE	external quantum efficiency
ETL	electron transporting layer
FF	fill factor
FM-AFM	frequency modulated atomic force microscopy
FM-KPFM	frequency modulated KPFM
GRIM	Grignard metathesis
H-NMR	proton nuclear magnetic resonance
HOMO	highest occupied molecular orbital
ITO	indium tin oxide
IV	current - voltage
J _{sc}	short circuit current density
JV	current density - voltage

KFM	kelvin force microscopy
KPFM	kelvin probe force microscopy
LUMO	lowest occupied molecular orbital
MDMO-PPV	poly[2-methoxy-5-(3',7'-dimethyloctyloxy)-1,4-phenylenevinylene]
MEH-PPV	Poly[2-methoxy-5-(2-ethylhexyloxy)-1,4-phenylenevinylene]
MPP	maximum power point
OPV	organic photovoltaics
P3HT	poly(3-hexylthiophene-2,5-diyl)
PC ₇₁ BM	[6,6]-phenyl C71 butyric acid methyl ester
PCBM	phenyl-C61-butyric acid methyl ester
PCDTBT	poly[[9-(1-octylnonyl)-9H-carbazole-2,7-diyl]-2,5-thiophenediyl-2,1,3-benzothiadiazole-4,7-diyl-2,5-thiophene-diyl]
PCE	power conversion efficiency
PCNEPV	poly[oxa-1,4-phenylene-(1-cyano-1,2--vinylene)-(2-methoxy-5-(3,7-dimethyloctyloxy)-1,4-phenylene)-1,2-(2-cyano-vinylene)-1,4-phenylene]
PCPDT-DTTzTz	(poly[[4-(2'-ethylhexyl)-4-octyl-4H-cyclopenta[2,1-b:3,4-b']dithiophene-2,6-diyl]--alt-[2,5-di(3'-hexylthiophen-2'-yl)thiazolo[5,4-d]-thiazole-5',5"-diyl])
PCPDTBT	Poly[2,6-(4,4-bis-(2-ethylhexyl)-4H-cyclopenta [2,1-b;3,4-b']dithiophene)-alt-4,7(2,1,3-benzothiadiazole)]
PEDOT:PSS	poly(3,4-ethylenedioxythiophene) polystyrene sulfonate
PF-QNM	PeakForce quantitative nanomechanical property mapping
PF-Tapping	PeakForce tapping
PF-TUNA	PeakForce tunnelling AFM
PFN	poly[(9,9-bis(3'-(N,N-dimethylamino)-propyl)-2,7-fluorene)-alt-2,7-(9,9-dioctylfluorene)]
PPV	poly(1,4-phenylene vinylene)
Pt/Ir	platinum/iridium
PV	perylene tetracarboxylic derivative
PV technologies	photovoltaic technologies
R _s	series resistance

R_{SH}	shunt resistance
RF	radio frequency
SCLC	space charge limited current
SEM	scanning electron microscopy
SPM	scanning probe microscopy
STM	scanning tunnelling microscopy
TEM	transmission electron microscopy
UHV-KPFM	ultra high vacuum kelvin probe force microscopy
V_{CPD}	contact potential difference
V_{OC}	open circuit voltage
XPS	X-ray photoelectron spectroscopy

Part I

Research context and goals

Chapter 1

Introduction

1.1 Renewable Energy

Each increase in quality of power generation resulted in an increase of usability, where initially wood was burned for heat a transition was made to convert this heat into motion and subsequently motion was converted into electrical energy. With the development of grid-based types of energy the availability of energy increased while the generation could be centralized. However, all these technologies were based mainly on fossil fuels such as wood, coal, oil and gas and burning these traditional fuels resulted in increased carbon emissions which eventually could result in an increase of global temperatures. Additionally, as more and more fossil fuels are burned less will remain and as demand and supply theory dictates prices will rise. While nuclear technologies appear to be a short term solution they are not in the long term as there still is a dependence on nuclear materials, additionally, the waste generated has a half-life in the thousands of years.

Figure 1.1 clearly illustrates the difference in energy consumption per capita for developing countries, transition countries, newly industrializing countries and industrialized countries in 1997. The average percentage of world population in the group of industrialized countries is dwarfed by the

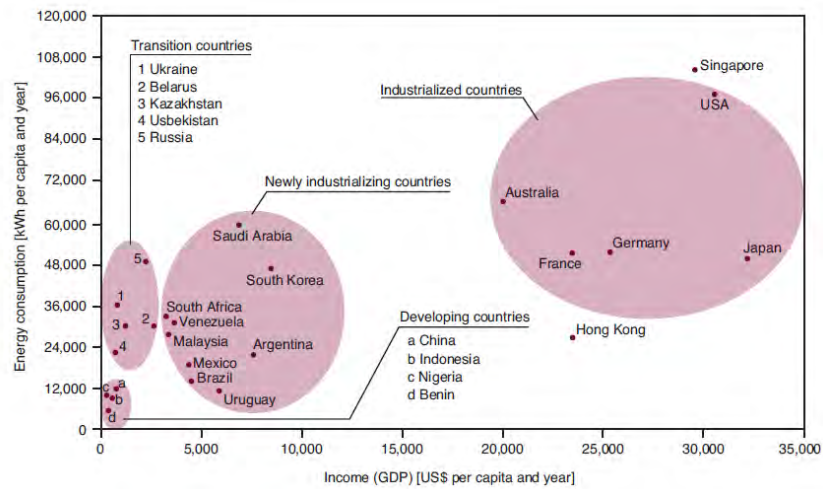


Figure 1.1: The relation between mean income (GDP per capita) and energy consumption (per capita demand in kWh) in 1997 for different country groups.^[5]

percentage of world population in the combination of what in 1997 were developing and transition countries. If all countries are to develop towards a similar state of industrialization it is of the utmost importance to have reliable and renewable energy sources.

The renewable energy sources which are actively being developed are in the form of hydropower, biomass, geothermal energy, wind power and solar energy. And while each technique has a specific upside, the potential of solar energy is huge as the average yearly solar flux sits at around 3850000 exajoules while the primary energy use in 2013 was "only" 533 exajoules.^[3,7] Figure 1.2 shows the amount of usable energy from different energy sources such as solar radiation, geothermal energy, biomass,... and of all of these sources solar energy has the highest potential. Especially when taking the possibility of delocalized energy generation and storage into account.

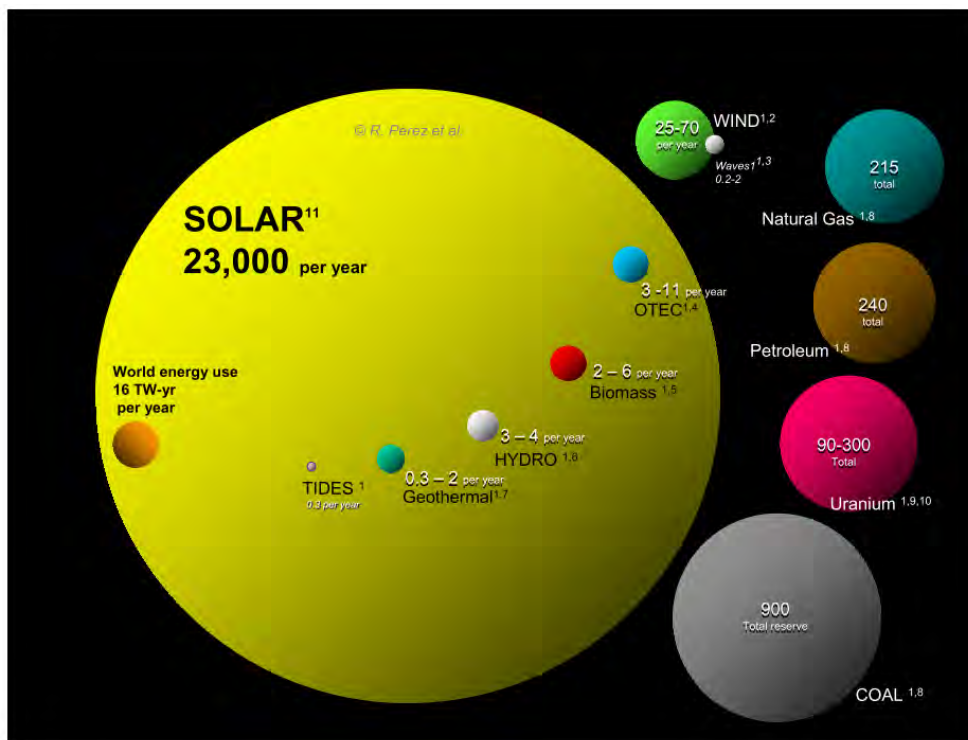


Figure 1.2: Direct comparison between the finite and renewable energy reserves. From^[16]

1.2 The development and applications of photovoltaics

Solar energy is convertible in three distinct forms: (1) solar thermal in which energy is converted into heat by collectors on roof tops or in deserts by concentrating incident light onto a single focus point.^[11] (2) Solar chemical power with the prime example of converting water into the individual elements of oxygen and hydrogen (2).^[6] (3) Direct conversion of light energy to electricity energy.^[12] Direct conversion into electricity is the application that has the best scaling factor of the aforementioned options. Individual solar cells can be made down to the millimeter scale or up converted to a size spanning 1.5 by 1 meter creating endless possibilities towards integration into present and future technologies.

However, to understand how photovoltaic devices can be implemented in future technologies it is important to take a look in the past and understand the progress that has been made since the discovery of the photovoltaic effect, by studying an electrode in a conductive solution exposed to light, by Alexandre-Edmond Becquerel in 1839. About 34 years later photoconductivity was found in selenium by Willoughby Smith and in 1883 a solar cell was developed based on selenium on a thin layer of gold. While the first solar cell had a performance of less than 1%, interest in the technology sparked and in 1888 patents "US389124" and "US389125" were awarded to Edwaed Weston.^[19,20]

The basic semiconductor-junction solar cell based on copper and copper oxide was developed in 1904 by Wilhelm Hallwachs, however, the biggest breakthrough was announced in 1954 on april 25th at Bell Labs with the invention of the first silicon solar cell with an efficiency of around 6%. And as time passed by silicon cell efficiencies rose steadily to 14% in 1960 and 20% in 1985 as illustrated in figure 1.3. currently devices based on silicon technologies are flirting with the border of 26%. This efficiency however, is close to the calculated Shockley-Queisser limit of 30% for single junction

solar cells.^[17] And while performance of silicon based solar cells is high, their production requires a multitude of processing resulting in a technology with a need for high initial investment and a corresponding rather high energy payback time.^[10]

Only 4 years after the announcement by Bell labs, the first report on an organic PV cell appeared in literature. An anthracene single crystal was studied and demonstrated a low photovoltage of 200 mV.^[8] Power conversion efficiency of these single active layer materials remained below 0.1% due to the strongly bound excitons which were not easily split to generate sufficient photocurrent.

The biggest breakthrough in the field of organic photovoltaics happened in 1986 with the work of Ching W. Tang with the demonstration of bilayer photovoltaic cells from organic semiconductors with offset energy bands. The cells reached efficiencies close to 1% due to the increased exciton dissociation at the donor acceptor interface.^[18] The effective limit in organic bilayer solar cells comes from the inherently low excitonic diffusion length, typically lower than 10 nm.^[13]

The next improvement in efficiency was obtained by replacing the bilayer with a bulk heterojunction in which the donor and acceptor materials were finely intermixed down to a scale of only a few nanometers hereby limiting the effect of the low excitonic diffusion length. This resulted in efficiencies surpassing the 2% and eventually led to power conversion efficiencies of up to 10% from commercially available polymers.^[21] However, to be able to reach these levels of power conversion efficiency a controlled morphology is needed, material phases can't be too large due to the limited exciton diffusion lengths while a too fine intermixing will hinder charge extraction.

Additionally, microstructure has been proven to be a decisive factor in other types of solar cells, more specifically thin film based technology. For example, conductive atomic force microscopy (C-AFM) led to the discovery of the increased grain boundary conductivity in chalcopyrite based absorber layers.^[1,9]

A tool to assess microstructure was developed in the form of scanning force microscopy or atomic force microscopy (AFM) in 1986 by Binnig, Quate and Gerber. They improved upon the idea of scanning tunnelling microscopy (STM) by replacing the wire of an STM with a simple lever made out of a diamond at the end of a thin gold strip.^[2] This first type of atomic force microscope was a contact type, in which the tip remained in contact during scanning. This contact technique was improved upon in the mid 1990's by the addition of current sensing capabilities.^[14]

Significant improvements towards lateral resolution were made with the development of dynamic mode AFM techniques.^[4] Moreover, Nonnenmacher et al. were able to combine dynamic mode AFM with the vibrating plate idea of Zismann to determine local potential differences.^[15,22]

It is on this premise that the work presented here is built, "How can morphology and electronic properties be studied in current and novel generation solar cells using advanced AFM techniques?"

1.3 Goal and structure of the thesis

1.3.1 Goal of the thesis

The goal of this thesis was to investigate the applicability of advanced atomic force microscopy techniques on novel materials as used in the most recent generation solar cells and possibly further quantify the results obtained by kelvin probe force microscopy (KPFM) and C-AFM through a deeper analysis of local current-voltage curves. The materials under investigation were conjugated polyelectrolytes (CPEs) - used as an intermediary layer between the cathode and the bulk heterojunction (BHJ) -, perovskite in the form of methylammonium lead tri-iodide/chloride ($\text{CH}_3\text{NH}_3\text{PbI}_{3-x}\text{Cl}_x$) as an absorber layer and the more standard poly(3-hexylthiophene-2,5-diyl) (P3HT) and poly[[9-(1-octylnonyl)-9H-carbazole-2,7-diyl]-2,5-thiophenediyl-2,1,3-benzothiadiazole-4,7-diyl-2,5-thiophene-diyl] (PCDTBT) donor polymers.

1.3.2 Structure of the thesis

Chapter two details the working principle of (organic) semiconductors as used in photovoltaic applications and it gives an overview of the possible charge injection mechanisms into organic thin films. It ends with an overview of the need for nanoscale characterization to elucidate the processes as observed on the macroscale.

Chapter three gives an overview of the basic and more advanced characterization techniques as used in this work. A short discussion on profilometry, analysis of current voltage curves and external quantum efficiency is given. A more in depth discussion on the working principles of atomic force microscopy is presented as the second part of this chapter.

Chapter four contains the results and discussion. The first section discusses the possible injection mechanisms and the applicability to study local current voltage curves as obtained by conductive AFM. Moreover, it relates the measured contact potential difference between tip and sample as measured by KPFM to the local injection mechanism.

The second section explicates the use of advanced atomic force microscopy techniques on conjugated polyelectrolytes as interlayers for high performance organic solar cells. A combined analysis of both the mechanical and electrical properties led to the conclusion that the interlayers studied in this work do not need full coverage to have a clear effect on the electrical properties.

The third section shows novel results on the nanoscale characterization of lead halide based perovskite. From conductive AFM it can be deduced that the local conduction does not appear to be uniform, moreover, the uniformity in this case is not linked to the local contact potential difference or grain orientation.

The fourth and final section shows how KPFM can be used to analyse the local degradation mechanisms of the cathode as used in standard organic

BIBLIOGRAPHY

solar cells. By analysing the surface potential of the calcium aluminium contact both on P3HT:PCBM (phenyl-C61-butyric acid methyl ester (PCBM)) and on indium tin oxide (ITO) it can be seen that the degradation detected can be attributed to the calcium layer and can be independently studied from the degradation of the organic layer.

The final chapter contains the conclusion and suggestions for future work and possible pitfalls when applying AFM (and derived techniques) to novel material systems.

The appendix contains all relevant information pertaining sample preparation and characterization.

Bibliography

- [1] R. Baier, J. Lehmann, S. Lehmann, T. Rissom, C. Alexander Kaufmann, A. Schwarzmann, Y. Rosenwaks, M. C. Lux-Steiner, and S. Sadewasser. Electronic properties of grain boundaries in Cu(In,Ga)Se₂ thin films with various Ga-contents. *Solar Energy Materials and Solar Cells*, 103:86–92, Aug. 2012.
- [2] G. Binnig, C. Quate, and C. Gerber. Atomic force microscope. *Physical review letters*, 56(9), 1986.
- [3] BP. Statistical Review of World Energy. Technical report, 2014.
- [4] F. Giessibl. Atomic resolution of the silicon (111)-(7x7) surface by atomic force microscopy. *Science*, (13):1–4, 1995.
- [5] H. Grassl, J. Kokott, M. Kulesa, J. Luther, F. Nuscheler, R. Sauerborn, H.-J. Schellnhuber, R. Schubert, and E.-D. Schulze. World in transition: Towards sustainable energy systems. 2003.
- [6] D. Gust, T. a. Moore, and A. L. Moore. Solar fuels via artificial photosynthesis. *Accounts of chemical research*, 42(12):1890–8, Dec. 2009.

BIBLIOGRAPHY

- [7] W. Hermann. Quantifying global exergy resources. *Energy*, 31(12):1685–1702, Sept. 2006.
- [8] H. Kallmann and M. Pope. Photovoltaic Effect in Organic Crystals. *The Journal of Chemical Physics*, 30(2):585–586, Feb. 1959.
- [9] G. Y. Kim, J. R. Kim, W. Jo, D.-H. Son, D.-H. Kim, and J.-K. Kang. Nanoscale observation of surface potential and carrier transport in $\text{Cu}_2\text{ZnSn}(\text{S},\text{Se})_4$ thin films grown by sputtering-based two-step process. *Nanoscale research letters*, 9(1):10, Jan. 2014.
- [10] F. Krebs and N. Espinosa. 25th Anniversary Article: Rise to Power - OPV-Based Solar Parks. *Advanced Materials*, pages 1–11, 2014.
- [11] K. Lovegrove and W. Stein, editors. *Concentrating solar power technology - Principles, developments and applications*. 2012.
- [12] A. Luque and S. Hegedus, editors. *Handbook of Photovoltaic Science and Engineering*. 2 edition, 2011.
- [13] D. Markov, C. Tanase, P. Blom, and J. Wildeman. Simultaneous enhancement of charge transport and exciton diffusion in poly(p-phenylene vinylene) derivatives. *Physical Review B*, 72(4):045217, July 2005.
- [14] M. P. Murrell, M. E. Welland, S. J. O’Shea, T. M. H. Wong, J. R. Barnes, A. W. McKinnon, M. Heyns, and S. Verhaverbeke. Spatially resolved electrical measurements of SiO_2 gate oxides using atomic force microscopy. *Applied Physics Letters*, 62(7):786, 1993.
- [15] M. Nonnenmacher, M. P. O’Boyle, and H. K. Wickramasinghe. Kelvin probe force microscopy. *Applied Physics Letters*, 58(25):2921, 1991.
- [16] R. Perez and M. Perez. A fundamental look at energy reserves for the planet. *The IEA SHC Solar Update*, pages 9–11, 2009.
- [17] W. Shockley and H. J. Queisser. Detailed Balance Limit of Efficiency of p-n Junction Solar Cells. *Journal of Applied Physics*, 32(3):510, 1961.

BIBLIOGRAPHY

- [18] C. W. Tang. Two-layer organic photovoltaic cell. *Applied Physics Letters*, 48(2):183, Jan. 1986.
- [19] B. Weston. Apparatus for utilizing solar radiant energy, 1888.
- [20] B. Weston. Art of utilizing solar radiant energy, 1888.
- [21] G. Yu, J. Gao, J. C. Hummelen, F. Wudl, and A. J. Heeger. Polymer Photovoltaic Cells: Enhanced Efficiencies via a Network of Internal Donor-Acceptor Heterojunctions. *Science*, 270(5243):1789–1791, Dec. 1995.
- [22] W. a. Zisman. a New Method of Measuring Contact Potential Differences in Metals. *Review of Scientific Instruments*, 3(7):367, 1932.

BIBLIOGRAPHY

Chapter 2

(Organic) semiconductors for photovoltaic conversion

The following chapter will describe the basic working principles of excitonic solar cells and perovskite based solar cells, starting from the familiar concept of a bilayer similar to the device layout as used in traditional silicon based photovoltaic technologies (PV technologies) moving onto the concept of bulk heterojunctions and ending with perovskite based solar cells. Additional attention will be given to the description of metal-semiconductor contacts as these are of the utmost importance when discussing conductive atomic force microscopy results.

2.1 Working Principle

The bilayer organic solar cell of Tang (figure 2.1 (a)) consisted of 30 nm of copper phthalocyanine (CuPc) and 50 nm of perylene tetracarboxylic derivative (PV) derivative deposited by vacuum deposition on ITO, the other electrode consisted out of silver. Upon illumination incident pho-

CHAPTER 2. (ORGANIC) SEMICONDUCTORS FOR PHOTOVOLTAIC CONVERSION

tons will generate excitons, mostly in the CuPc layer, which are thereafter separated in case they reach the interface between the two organic materials or recombine. After separation, holes are transported in the CuPc towards the ITO while the electrons are transported through the PV layer onto the Ag electrode.^[49] This paragraph illustrates the five essential processes in (organic) solar cells namely: (1) absorption, (2) exciton diffusion, (3) exciton separation, recombination, (4) charge transport and (5) charge collection at the electrodes.^[35] A novel concept was the introduction of the bulk heterojunction, in this approach donor and acceptor are finely intermixed (fig. 2.1 (b)). The discussion on the basic physics remains the same however.

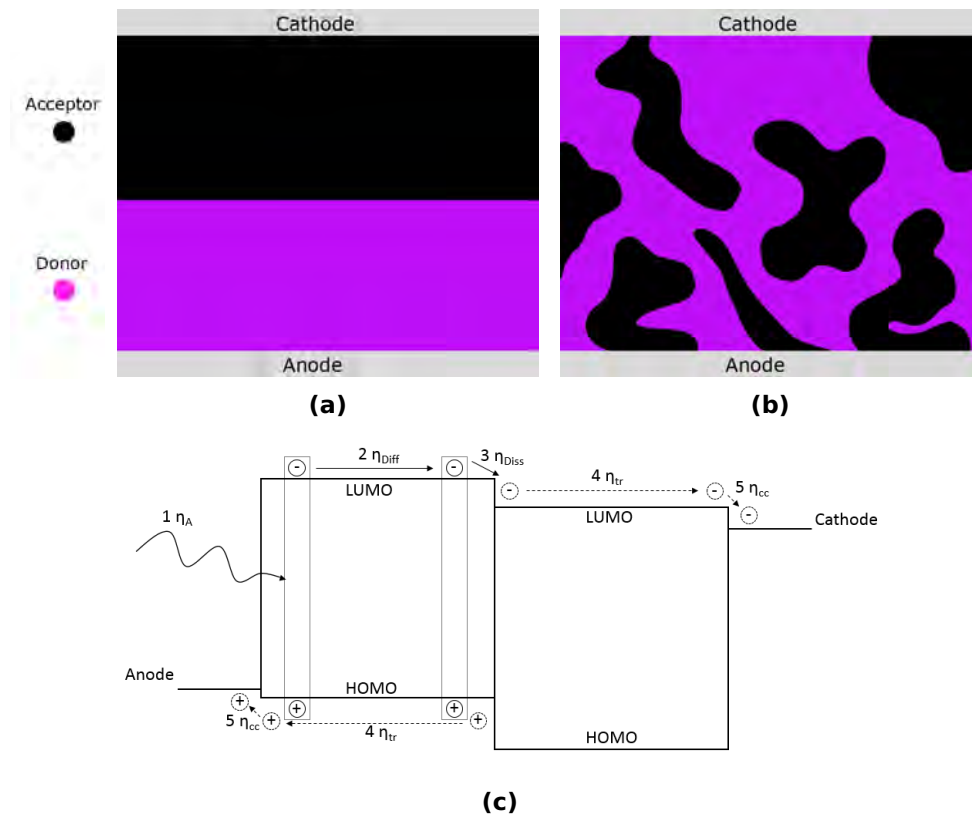


Figure 2.1: Working principle (c) and overview of the initial morphology (a) and of the currently used configuration for high efficient donor-acceptor blends (b).

CHAPTER 2. (ORGANIC) SEMICONDUCTORS FOR PHOTOVOLTAIC CONVERSION

The starting point for a highly efficient solar cell is a good absorption, as a high absorption will result in a high yield of exciton creation. Organic semiconductors typically have high absorption coefficients, thereby allowing devices with an active layer which is only a few hundreds of nanometers thick. However, compared to inorganic semiconductors the band gaps of organic semiconductors tend to be large and the corresponding absorption window narrow (Figure 2.2). The aforementioned band gap is defined by the energy difference between the highest occupied molecular orbital (HOMO) and the lowest occupied molecular orbital (LUMO) and typically for P3HT this is in the order of 2.0 eV (620 nm). Significant progress has been made towards creation of low band gap polymers and a prime example is the carbazole-based Poly[2,6-(4,4-bis-(2-ethylhexyl)-4H-cyclopenta [2,1-b;3,4-b']dithiophene)-alt-4,7 (2,1,3-benzothiadiazole)] (PCPDTBT) with a band gap of 1.5 eV.^[6,46]

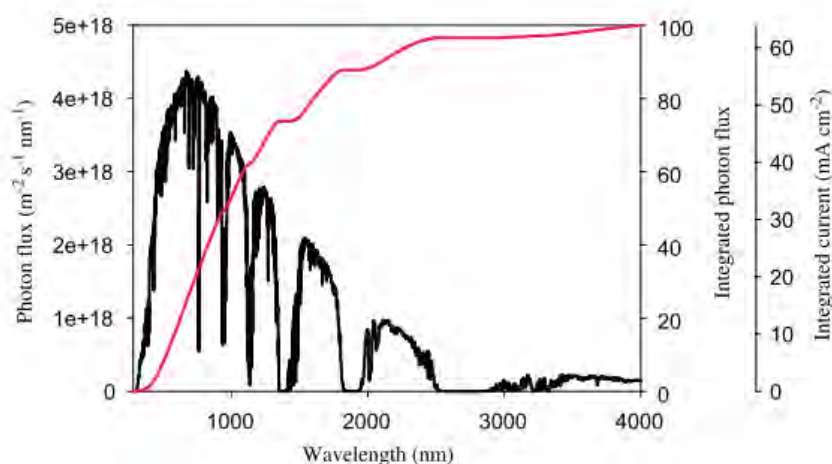


Figure 2.2: Air mass 1.5 (AM1.5) spectrum, combined with the integral of the spectrum showing as a percentage of total number of photons that can contribute to the current density. From^[9]

With proper absorption ensured, the generated excitons now need to be efficiently separated as otherwise the strongly bound electron-hole pair will decay either via a radiative or a non-radiative process. The generated

CHAPTER 2. (ORGANIC) SEMICONDUCTORS FOR PHOTOVOLTAIC CONVERSION

excitons will only properly dissociate at a donor - acceptor interface (D/A Interface) interface and thus as average diffusion lengths are quoted between 1 and 20 nm, the only option to maximize photocurrent from exciton dissociation is to have a D/A interface present within the exciton diffusion length.^[21,22,27,28,41,44]

Upon reaching the donor-acceptor interface, the exciton can dissociate into free charge carriers via the charge transfer state. This concept describes the process in which the holes remain in the HOMO of the donor material while the electron is transferred to the acceptor. Additionally, the charge transfer process is highly efficient due to its corresponding time scale in the femtosecond range and no competing recombination process exists on this time scale.^[7,20,42]

As separate free charges are now present in donor and acceptor phases the charges will start to move within these materials due to drift and diffusion. The applicable model strongly depends on the morphology of the D/A interface relative to the electrodes, e.g. diffusion will dominate in a bilayer while in a bulk-heterojunction device with a random distribution of donor and acceptor interfaces the net diffusion will be small and as a result drift will dominate.^[5,10,12,29] When the free charges are moving through the material they can encounter impurities, defects, bad pathways, . . . which will possibly act as recombination centers and thereby limit the photocurrent and open circuit voltage of the device.^[47] The efficiency of charge transport is therefore important as it is competing with (interfacial) recombination processes.

Eventually the generated charges will encounter the electrodes and either recombine at the interface between electrode and bulk heterojunction or be transported out of the device. The description of the charge extraction process heavily depends on the alignment of the Fermi levels of contacts with HOMO and LUMO levels of donor and acceptor respectively.^[36]

In the most simple picture for charge extraction either hopping or tunneling is the dominant process depending on the height of the energy barrier and temperature. However an exact description of the process is far more complex due the morphology at and chemical structure of the organic-electrode interface.^[4,34,43] Traditionally contacts are evaporated and ion or metal diffusion into the organic layer is possible, moreover, it has been proven that interfacial dipoles and band bending are possible effects that can affect the injection or charge extraction process.^[8]

2.2 Charge injection and transport in organic thin films

This section discusses some of the possible injection mechanisms at metal/semiconductor interfaces. The description as given here uses the electron in the conduction band (LUMO) as current contributing particle, however, the discussion is equally valid with the holes in the valence band (HOMO) as current carrying particles.

2.2.1 Schottky emission

Schottky emission is a mechanism in which an electron is thermally activated and thereby gains sufficient energy to overcome the energy barrier at the metal-organic interface. The energy barrier itself can be modified by an image force, which is called the Schottky effect.^[17,43] This type of conduction mechanism is mainly found at high temperatures. The general expression for Schottky emission is given by:

$$J = A^* T^2 \exp \left[\frac{-q(\phi_B - \sqrt{q(V/4d\pi\epsilon_r\epsilon_0)})}{kT} \right] \quad (2.1)$$

The term A^* is the effective Richardson constant and is given by the following relation:

$$A^* = \frac{4\pi q k^2 m^*}{h^3} = \frac{120 m^*}{m_0} \quad (2.2)$$

The other parameters are J the current density, m_0 the free electron mass, m^* is the effective electron mass in the thin film, T is the temperature in Kelvin, q the electronic charge, ϕ_B the Schottky barrier height, V the applied voltage, k the Boltzmann constant, h Planck's constant, d the thickness of the layer, ϵ_0 the permittivity in vacuum and ϵ_r the optical dielectric constant. The square root factor in the exponential term takes the effect of barrier lowering, due to charge transfer from the metal to the (organic) semiconductor, into account. From these equations it can be deduced that for true Schottky emission the plot of $\log(J/T^2)$ should increase linearly with $V^{1/2}$ and it is possible to determine the barrier height from the intercept of the Schottky plot.

2.2.2 Poole Frenkel

This type of conduction mechanism is similar to Schottky emission: it is due to a field enhanced thermal excitation of trapped electrons in the conduction band. The difference with Schottky emission is the height of the trap potential wall (the square root factor in the exponential term) which is smaller than in the case of Schottky emission.^[18] The field enhancement is expressed by the V/d factor in the equation. The current for the Poole Frenkel type conduction is given by the following equation:

$$J \sim V/d \cdot \exp \left[\frac{-q(\phi_B - \sqrt{qV/d\pi\epsilon})}{kT} \right] \quad (2.3)$$

The symbols as used here have the same definition as for Schottky emission.

2.2.3 Fowler-Nordheim Tunneling

Classical physics dictates that when electrons encounter an energy barrier they are not able to cross the barrier and are simply reflected. However, according to quantum mechanics the electrons are able to penetrate the barrier whenever the barrier is sufficiently thin. Fowler-Nordheim tunneling occurs whenever the applied electric field ($E = V/d$) is high enough so that electrons are able to penetrate a triangular potential barrier. The current in that case has the following relation to the potential barrier and applied electric field.

$$J = \frac{q^3 V^2}{8d^2 \pi h q \phi_B} \exp \left[\frac{-8d\pi(2qm_T^*)^{1/2}}{3hE} \phi_B^{3/2} \right] \quad (2.4)$$

In this case m_T^* is the tunneling effective mass while the other notations remain the same. Equation 2.4 shows that whenever $\ln(J/V^2)$ is plot versus $1/V$ the resulting curve should be linear. This theory is mostly valid at high electric fields due to the triangular barrier formed at high fields.^[23,26]

2.2.4 Direct Tunneling

Direct tunneling is quantum mechanical tunneling through a square barrier, which is valid at intermediate fields.^[26] The current density and the applied electric field have the following relation:

$$J \sim \frac{V}{d} \cdot \exp \left[-\frac{2d}{\hbar} \sqrt{2m^* \phi_B} \right] \quad (2.5)$$

Therefore, whenever a linear behaviour is found between the current and the applied bias direct tunneling is a possible injection mechanism. In addition to the notation as used above, \hbar is the reduced Plank constant and m^* is the effective mass.

2.2.5 Space charge limited current

When carriers can enter a material system and freely move through the system the resulting current and carrier densities will be higher than in the previous injection models. This higher charge carrier density will result in a field gradient and thereby limit the current density. Space charge limited current in the most general form is given by equation 2.6, often called the Mott-Gurney law, and can be derived from the expression of the drift current and Gauss's law.^[40]

$$J = \frac{9}{8} \epsilon_r \epsilon_0 \mu V^2 / d^3 \quad (2.6)$$

This equation describes a mobility dependent current density, moreover, it has been shown for organic layers that the mobility can be field dependent which in turn leads to the Murgatroyd equation (eq. 2.7).^[48]

$$J = \frac{9}{8} \epsilon \mu_0 \frac{V^2}{d^3} \exp \left[\frac{0.89 \beta \sqrt{V}}{\sqrt{d}} \right] \quad (2.7)$$

However, for the current to be space charge limited the contact barrier between metal and organic needs to be smaller than 0.3 eV.^[3] If this is not the case, the contact cannot be considered ohmic and the current will be injection limited.

2.2.6 Ohmic conduction

Ohmic conduction is the simple case in which the current varies linearly with the applied electric field, proportionally with the resistance of the material through which the current flows.

$$J = \sigma \frac{V}{d} = nq\mu \frac{V}{d} \quad (2.8)$$

$$n = N_C \exp \left[\frac{-(E_C - E_F)}{kT} \right] \quad (2.9)$$

The parameters in this equation are μ the mobility and n the charge density. The charge density is defined by equation 2.9 with E_F the Fermi energy, E_C the conduction band edge and N_C the effective density of states.

2.2.7 Ionic conduction

Ionic conduction is a mechanism in which the movement of ions contributes to the current, which is similar to a diffusion process. This type of conduction can be easily assessed from the time dependence of the conductivity. As the ions can't be injected or extracted, the dc conductivity generally speaking decreases in function of time as long as the electric field is applied. Moreover, this will result in charge build up near the electrodes and distorts the potential distribution. As the field is turned off or inverted hysteresis effects can be seen as the ions slowly move back to the equilibrium positions.^[11]

$$J \sim \frac{V}{dT} \exp\left[\frac{-\Delta E_{ai}}{kT}\right] \quad (2.10)$$

Equation 2.10 describes how the current varies in function of the applied voltage (V) and ΔE_{ai} is the activation energy of ions.

2.3 The need for nanoscale characterization

Optimization of devices heavily depends on tuning the electronic properties and interaction of the donor and acceptor materials as this will determine the eventual absorption, exciton generation and separation and charge transport while keeping recombination to a minimum. These processes heavily depend on the morphology of the donor/acceptor blend which in turn is tunable from several parameters during the deposition process.^[50]

CHAPTER 2. (ORGANIC) SEMICONDUCTORS FOR PHOTOVOLTAIC CONVERSION

An analysis of the finely intermixed layer of bulk heterojunction organic solar cells requires a high-resolution tool allowing a spacial mapping of the active layer. An apparatus extremely well suited to this goal is an atomic force microscope. Not only does it allow imaging at a 10 to 100 nm scale, the techniques derived from AFM such as conductive AFM and kelvin probe force microscopy give additional information on local composition, electric and electronic properties. Electron beam based analysis techniques such as scanning electron microscopy (SEM) and transmission electron microscopy (TEM) give information at a similar scale and additionally are able to study the exact composition however, they often induce structural changes or damage the sample. scanning probe microscopy (SPM) and electron beam based techniques are therefore mostly complementary. The mostly non-destructive nature of atomic force microscopy and derived techniques resulted in a more thorough understanding of the material systems currently used for organic photovoltaics (OPV).

The first conjugated polymers used in OPV were poly(1,4-phenylene vinylene (PPV) based polymers, these were also the first system on which advanced morphological studies were performed. An extensive TEM analysis of Poly[2-methoxy-5-(2-ethylhexyloxy)-1,4-phenylenevinylene] (MEH-PPV) mixed with buckminsterfullerene (C_{60}) revealed that a bicontinuous network formed at a 1:1 weight composition ratio evidencing the existence of a true bulk heterojunction.^[51] It was the work on PPV's that laid the basis for further research into the effect of morphology on the photovoltaic properties. With the further development of poly[2-methoxy-5-(3',7'-dimethyloctyloxy)-1,4-phenylenevinylene] (MDMO-PPV) efficiencies of up to 3% were reached. Moreover, further morphological analysis showed a strong dependence of the organic layers' morphology and structure on the used solvent and the duration of the subsequent annealing, affecting the photovoltaic properties.

CHAPTER 2. (ORGANIC) SEMICONDUCTORS FOR PHOTOVOLTAIC CONVERSION

A replacement for MDMO-PPV was found in P3HT which has a semi-crystalline structure and showed a strong dependence of the electro-optical properties on the crystallographic orientation of the P3HT. Moreover, the reduced bandgap of P3HT (1.9 eV) compared to MDMO-PPV (2.2 eV) allowed for a higher absorption and a corresponding higher short circuit current. Similar to MDMO-PPV the solvent had a large influence on the initial morphology of the bulk heterojunction and subsequent annealing further improved the morphology and the corresponding solar cell characteristics.

Glatzel and Hoppe et. al. used ultra high vacuum kelvin probe force microscopy (UHV-KPFM) to study the morphology and local work function of MDMO-PPV:PCBM blends both in dark and under a 675 nm laser diode illumination. They showed that the solvent had a significant impact on the local morphology, moreover, the discrepancy between morphology and KPFM images from the toluene casted blends showed that the PCBM clusters will be either covered by the surrounding matrix or uncovered resulting in very different photovoltaic behaviour for the two cases.^[19,24,25] Further work of Maturova et. al. developed a morphological device model in which the three dimensional nature of phase separation was developed into a two-dimensional model which was used to study and replicate the experimental results from drift-diffusion equations.^[30,31]

As KPFM is sensitive to local electric fields it can also be used to study local (induced) trap formation as presented by O.G. Reid et al. They showed that it was possible to correlate the local charging rate to the quantum efficiency of photochemically degraded areas of the film. However, the photovoltage as determined via KPFM did not show a direct correlation to any of the photochemically induced changes in the devices characteristics.^[38] In a different work, David Ellison was able to directly link the open circuit voltage of organic bilayers to the photovoltage response as measured with KFM.^[16] Siddiki et. al. further investigated the energy barriers between interfaces in double-junction organic solar cells and were able to

CHAPTER 2. (ORGANIC) SEMICONDUCTORS FOR PHOTOVOLTAIC CONVERSION

determine the effect of energy barriers and energetically favorable offsets for charge transport in interlayers.^[45]

The first report of nanoscale charge transport as studied with conductive AFM on organic layers was produced by Alexeev in 2006. The material under investigation was a mixture of MDMO-PPV and poly[oxa-1,4-phenylene-(1-cyano-1,2-vinylene)-(2-methoxy-5-(3,7-dimethyloctyloxy)-1,4-phenylene)-1,2-(2-cyanovinylene)-1,4-phenylene] (PCNEPV) and a clear contrast was seen between the MDMO-PPV donor and the PCNEPV acceptor.^[2] Further investigations mainly focused on the local morphology and phase separation of the materials in the bulk heterojunction blend.^[1,13-15,39] Additional research invested time in extracting physical properties from local current - voltage (IV) curves. Reid proposed a semi-empirical expression with a scaling factor to account for the tip-sample geometry.^[37] The experiments done by Moerman et. al. however indicated a different behaviour for P3HT nanofiber thin films. They showed via theoretical calculations and lateral C-AFM measurements on patterned channels with different widths that the space charge limited current (SCLC) type behaviour exists mostly in a spherical region of a few tens of nanometers in diameter immediately below the AFM tip.^[32,33]

This short overview of the status of kelvin probe force microscopy and conductive AFM shows a promising field to further understand the physics of organic semiconductors and bulk heterojunction solar cells at the nanoscale, and that several different options exist to correlate the nanoscale properties to the macroscale. Moreover, the overview on AFM techniques presented above indicates the necessity to consider the complementary nature of KPFM and C-AFM

Bibliography

- [1] A. Alexeev and J. Loos. Conductive atomic force microscopy (C-AFM) analysis of photoactive layers in inert atmosphere. *Organic Electronics*, 9(1):149–154, Feb. 2008.
- [2] a. Alexeev, J. Loos, and M. M. Koetse. Nanoscale electrical characterization of semiconducting polymer blends by conductive atomic force microscopy (C-AFM). *Ultramicroscopy*, 106(3):191–9, Feb. 2006.
- [3] V. I. Arkhipov, H. von Seggern, and E. V. Emelianova. Charge injection versus space-charge-limited current in organic light-emitting diodes. *Applied Physics Letters*, 83(24):5074, 2003.
- [4] H. Ba. Injection , Transport and Recombination of Charge Carriers in Organic Light- emitting Diodes. 418(December 1997):402–418, 1998.
- [5] J. Barker, C. Ramsdale, and N. Greenham. Modeling the current-voltage characteristics of bilayer polymer photovoltaic devices. *Physical Review B*, 67(7):075205, Feb. 2003.
- [6] P. W. M. Blom, V. D. Mihailetschi, L. J. a. Koster, and D. E. Markov. Device Physics of Polymer:Fullerene Bulk Heterojunction Solar Cells. *Advanced Materials*, 19(12):1551–1566, June 2007.
- [7] C. Brabec, G. Zerza, and G. Cerullo. Tracing photoinduced electron transfer process in conjugated polymer/fullerene bulk heterojunctions in real time. *Chemical physics letters*, 340(June):232–236, 2001.
- [8] S. Braun, W. R. Salaneck, and M. Fahlman. Energy-Level Alignment at Organic/Metal and Organic/Organic Interfaces. *Advanced Materials*, 21(14-15):1450–1472, Apr. 2009.
- [9] E. Bundgaard and F. Krebs. Low band gap polymers for organic photovoltaics. *Solar Energy Materials and Solar Cells*, 91(11):954–985, July 2007.

BIBLIOGRAPHY

- [10] D. Cheyns, J. Poortmans, P. Heremans, C. Deibel, S. Verlaak, B. Rand, and J. Genoe. Analytical model for the open-circuit voltage and its associated resistance in organic planar heterojunction solar cells. *Physical Review B*, 77(16):165332, Apr. 2008.
- [11] F.-C. Chiu. A Review on Conduction Mechanisms in Dielectric Films. *Advances in Materials Science and Engineering*, 2014:1–18, 2014.
- [12] J. Cuiffi, T. Benanti, W. J. Nam, and S. Fonash. Modeling of bulk and bilayer organic heterojunction solar cells. *Applied Physics Letters*, 96(14):143307, 2010.
- [13] M. Dante, J. Peet, and T.-Q. Nguyen. Nanoscale Charge Transport and Internal Structure of Bulk Heterojunction Conjugated Polymer/Fullerene Solar Cells by Scanning Probe Microscopy. *Journal of Physical Chemistry C*, 112(18):7241–7249, May 2008.
- [14] O. Douhéret, L. Lutsen, A. Swinnen, M. Bresselge, K. Vandewal, L. Goris, and J. Manca. Nanoscale electrical characterization of organic photovoltaic blends by conductive atomic force microscopy. *Applied Physics Letters*, 89(3):032107, 2006.
- [15] O. Douhéret, a. Swinnen, M. Bresselge, I. Van Severen, L. Lutsen, D. Vanderzande, and J. Manca. High resolution electrical characterisation of organic photovoltaic blends. *Microelectronic Engineering*, 84(3):431–436, Mar. 2007.
- [16] D. Ellison and J. Kim. Determination of quasi-Fermi levels across illuminated organic donor/acceptor heterojunctions by Kelvin probe force microscopy. *Journal of the American Chemical Society*, pages 13802–13805, 2011.
- [17] P. Emtage and J. O'Dwyer. Richardson-Schottky effect in insulators. *Physical review letters*, 16(9):1964–1966, 1966.
- [18] J. Frenkel. On pre-breakdown phenomena in insulators and electronic semi-conductors. *Physical Review*, 1938.

BIBLIOGRAPHY

- [19] T. Glatzel, H. Hoppe, N. S. Sariciftci, M. C. Lux-Steiner, and M. Komiyama. Kelvin Probe Force Microscopy Study of Conjugated Polymer/Fullerene Organic Solar Cells. *Japanese Journal of Applied Physics*, 44(7B):5370–5373, July 2005.
- [20] S. Günes, H. Neugebauer, and N. S. Sariciftci. Conjugated polymer-based organic solar cells. *Chemical reviews*, 107(4):1324–38, Apr. 2007.
- [21] J. Halls and R. Friend. The photovoltaic effect in a poly (p-phenylenevinylene)/perylene heterojunction. *Synthetic Metals*, 85:1307–1308, 1997.
- [22] a. Haugeneder, M. Neges, C. Kallinger, W. Spirkl, U. Lemmer, J. Feldmann, U. Scherf, E. Harth, a. Gügel, and K. Müllen. Exciton diffusion and dissociation in conjugated polymer/fullerene blends and heterostructures. *Physical Review B*, 59(23):15346–15351, June 1999.
- [23] B. Heinz and K. Anna. Charge Transport in Organic Semiconductors. (October 2011), 2012.
- [24] H. Hoppe, T. Glatzel, M. Niggemann, a. Hinsch, M. C. Lux-Steiner, and N. S. Sariciftci. Kelvin probe force microscopy study on conjugated polymer/fullerene bulk heterojunction organic solar cells. *Nano letters*, 5(2):269–74, Feb. 2005.
- [25] H. Hoppe, T. Glatzel, M. Niggemann, W. Schwinger, F. Schaeffler, a. Hinsch, M. C. Lux-Steiner, and N. Sariciftci. Efficiency limiting morphological factors of MDMO-PPV:PCBM plastic solar cells. *Thin Solid Films*, 511-512:587–592, July 2006.
- [26] G.-H. Lee, Y.-J. Yu, C. Lee, C. Dean, K. L. Shepard, P. Kim, and J. Hone. Electron tunneling through atomically flat and ultrathin hexagonal boron nitride. *Applied Physics Letters*, 99(24):243114, 2011.
- [27] D. Markov, C. Tanase, P. Blom, and J. Wildeman. Simultaneous enhancement of charge transport and exciton diffusion in poly(p-

BIBLIOGRAPHY

- phenylene vinylene) derivatives. *Physical Review B*, 72(4):045217, July 2005.
- [28] D. E. Markov, E. Amsterdam, P. W. M. Blom, A. B. Sieval, and J. C. Hummelen. Accurate measurement of the exciton diffusion length in a conjugated polymer using a heterostructure with a side-chain cross-linked fullerene layer. *The journal of physical chemistry. A*, 109(24):5266–74, June 2005.
- [29] R. A. Marsh, C. Groves, and N. C. Greenham. A microscopic model for the behavior of nanostructured organic photovoltaic devices. *Journal of Applied Physics*, 101(8):083509, 2007.
- [30] K. Maturová, S. V. Bavel, and M. Wienk. Morphological device model for organic bulk heterojunction solar cells. *Nano Letters*, (Gg 385):6–11, 2009.
- [31] K. Maturová, M. Kemerink, M. M. Wienk, D. S. H. Charrier, and R. a. J. Janssen. Scanning Kelvin Probe Microscopy on Bulk Heterojunction Polymer Blends. *Advanced Functional Materials*, 19(9):1379–1386, May 2009.
- [32] D. Moerman, R. Lazzaroni, and O. Douheret. Efficient bulk heterojunction photovoltaic cells with a pre-organized poly(3-hexylthiophene) phase. *Applied Physics Letters*, 99(9):093303, 2011.
- [33] D. Moerman, N. Sebaihi, S. E. Kaviyil, P. Leclere, R. Lazzaroni, and O. Douhéret. Towards a unified description of the charge transport mechanisms in conductive atomic force microscopy studies of semi-conducting polymers. *Nanoscale*, July 2014.
- [34] D. Natali and M. Caironi. Charge injection in solution-processed organic field-effect transistors: physics, models and characterization methods. *Advanced materials (Deerfield Beach, Fla.)*, 24(11):1357–87, Mar. 2012.

BIBLIOGRAPHY

- [35] P. Peumans, A. Yakimov, and S. R. Forrest. Small molecular weight organic thin-film photodetectors and solar cells. *Journal of Applied Physics*, 93(7):3693, 2003.
- [36] W. J. Potscavage, A. Sharma, and B. Kippelen. Critical interfaces in organic solar cells and their influence on the open-circuit voltage. *Accounts of chemical research*, 42(11):1758–67, Nov. 2009.
- [37] O. G. Reid, K. Munechika, and D. S. Ginger. Space charge limited current measurements on conjugated polymer films using conductive atomic force microscopy. *Nano letters*, 8(6):1602–9, June 2008.
- [38] O. G. Reid, G. E. Rayermann, D. C. Coffey, and D. S. Ginger. Imaging Local Trap Formation in Conjugated Polymer Solar Cells: A Comparison of Time-Resolved Electrostatic Force Microscopy and Scanning Kelvin Probe Imaging. *The Journal of Physical Chemistry C*, 114(48):20672–20677, Dec. 2010.
- [39] A. Rice, R. Giridharagopal, and S. Zheng. Controlling vertical morphology within the active layer of organic photovoltaics using Poly (3-hexylthiophene) nanowires and phenyl-C61-butyric acid methyl ester. *ACS nano*, (4):3132–3140, 2011.
- [40] A. Rose. Space-charge-limited currents in solids. *Physical Review*, 1, 1955.
- [41] T. J. Savenije, J. M. Warman, and A. Goossens. Visible light sensitisation of titanium dioxide using a phenylene vinylene polymer. (April):148–153, 1998.
- [42] P. Schilinsky, C. Waldauf, and C. J. Brabec. Recombination and loss analysis in polythiophene based bulk heterojunction photodetectors. *Applied Physics Letters*, 81(20):3885, 2002.
- [43] J. Scott and G. Malliaras. Charge injection and recombination at the metal-organic interface. *Chemical physics letters*, (January):115–119, 1999.

BIBLIOGRAPHY

- [44] P. E. Shaw, A. Ruseckas, and I. D. W. Samuel. Exciton Diffusion Measurements in Poly(3-hexylthiophene). *Advanced Materials*, 20(18):3516–3520, July 2008.
- [45] M. K. Siddiki, S. Venkatesan, D. Galipeau, and Q. Qiao. Kelvin probe force microscopic imaging of the energy barrier and energetically favorable offset of interfaces in double-junction organic solar cells. *ACS applied materials & interfaces*, 5(4):1279–86, Feb. 2013.
- [46] C. Soci, I.-W. Hwang, D. Moses, Z. Zhu, D. Waller, R. Gaudiana, C. J. Brabec, and a. J. Heeger. Photoconductivity of a Low-Bandgap Conjugated Polymer. *Advanced Functional Materials*, 17(4):632–636, Mar. 2007.
- [47] M. Soldera, K. Taretto, and T. Kirchartz. Comparison of device models for organic solar cells: Band-to-band vs. tail states recombination. *Physica Status Solidi (a)*, 209(1):207–215, Jan. 2012.
- [48] C. Tanase, P. Blom, and D. de Leeuw. Origin of the enhanced space-charge-limited current in poly(p-phenylene vinylene). *Physical Review B*, 70(19):193202, Nov. 2004.
- [49] C. W. Tang. Two-layer organic photovoltaic cell. *Applied Physics Letters*, 48(2):183, Jan. 1986.
- [50] B. Thompson and J. Fréchet. Polymer - Fullerene Composite Solar Cells. *Angewandte Chemie (International ed. in English)*, pages 58–77, 2008.
- [51] C. Yang and A. Heeger. Morphology of composites of semiconducting polymers mixed with C 60. *Synthetic metals*, 83:85–88, 1996.

Chapter 3

Characterization techniques

3.1 Introduction

Any OPV based device needs a thorough characterization in order to determine the relevant physical properties that regulate the measured performance. This chapter will discuss the basic characterization techniques such as current-voltage characteristics and external quantum efficiency (EQE) measurements and the more advanced atomic force microscopy, a technique extremely well suited to assess the nanoscale morphology.

3.2 Basic Characterization Techniques

3.2.1 Dektak

Profilometry is required to determine the absolute thickness of photovoltaic layers as the thickness leading to optimal device performances varies with the type of absorber layer.^[1,21] Profilometry is performed using a sharp tip to mechanically scan a surface. Whenever the thickness of

a layer was determined, it was measured using a Dektak stylus profilometer from Bruker unless otherwise stated.

3.2.2 Current-Voltage measurements

The traditional way to assess the efficiency of (organic) solar cells is through the analysis of current density - voltage (JV) curves, usually acquired both in dark and under standard AM1.5G illumination at 1 sun ($1 \text{ sun} = 100 \text{ mW/cm}^2$) as this best represents the solar spectrum of sunlight reaching the Earth's atmosphere. Figure 3.1 shows a possible IV-curve. The most interesting characteristic parameters extracted from this curve are the short circuit current density (J_{sc}), open circuit voltage (V_{oc}) and maximum power point (MPP). The short circuit current is defined as the current value at zero applied voltage, while the open circuit voltage corresponds to the voltage at which zero current is measured and the maximum power point is defined as the current-voltage point (J_{max} and V_{max}) at maximum power. From these well defined parameters the efficiency and fill factor can be calculated.

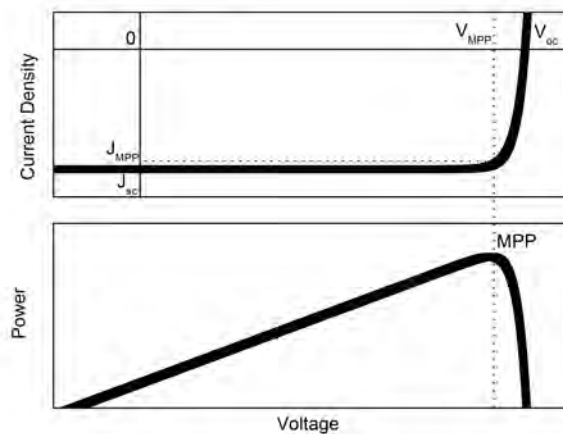


Figure 3.1: Current-Voltage characteristic and the relevant parameters that can be extracted.

CHAPTER 3. CHARACTERIZATION TECHNIQUES

The power conversion efficiency (η) is defined as the ratio of the maximal extracted power to the incident light power (P_{light}):

$$\eta = \frac{P_{out}}{P_{light}} = \frac{J_{max} * V_{max}}{P_{light}} \quad (3.1)$$

The fill factor (FF) is defined as:

$$FF = \frac{J_{max} * V_{max}}{J_{SC} * V_{OC}} \quad (3.2)$$

Including the fill factor in the equation of the efficiency leads to the following definition:

$$\eta = \frac{J_{SC} * V_{OC} * FF}{P_{light}} \quad (3.3)$$

The fill factor can be interpreted as a loss factor, as a low fill factor indicates possible interfacial problems. These interfacial problems can either come from the interface between bulk heterojunction and electrode or from the interface between donor and acceptor.

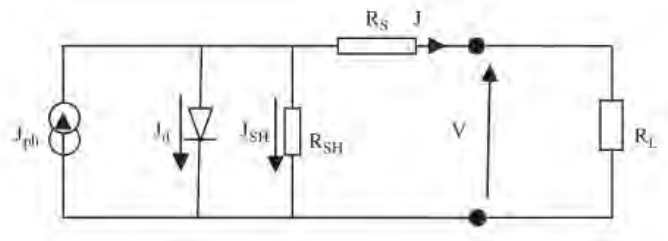


Figure 3.2: Single diode model as used to extract series and shunt resistance. From^[7]

A device model to describe these JV-curves is the simple single diode model as shown in figure 3.2. This equivalent circuit consists out of four separate parts: the photo-current (J_{ph}) as generated by the solar cell, the current through the diode J_d , the shunt resistance (R_{sh}) and the series resistance R_S . The series resistance is attributed to the individual resistivities of the used materials while the shunt resistance is related to the

recombination of charge carriers near the D/A Interface.

The power conversion efficiencies (PCEs) of the BHJ solar cells were characterized using a Newport class A solar simulator (model 91195A) calibrated with a silicon solar cell to give an AM 1.5G spectrum.

3.2.3 EQE

The external quantum efficiency is defined as the ratio of the number of charges collected at the electrodes to the number of incident photons at any given wavelength.

$$EQE(\lambda) = \frac{N_e(\lambda)}{N_{ph}(\lambda)} \quad (3.4)$$

EQE spectra were measured on a commercial setup from Bentham. A xenon arc lamp (300-670 nm) and a quartz halogen lamp (670-900 nm) were used as an illumination source, the incident light was chopped, coupled into a monochromator and aimed at the device in short circuit current conditions. The resulting current is sent through a Bentham477 current pre-amplifier and thereafter arrives in a Bentham485 lock-in amplifier. The setup was calibrated with a certified silicon cell.

3.2.4 Proton NMR

Proton nuclear magnetic resonance (H-NMR) is mainly used as a characterization technique to determine the chemical composition and molecular structure of a material.^[23] As the atomic nucleus is a spinning charged particle it generates a magnetic field. Without any externally applied magnetic field the nuclear spin is random. However, with the presence of an external field, the nuclear spins will align themselves with or against the direction of the field. Alignment against the field will cost energy while alignment with the field will allow the atoms to gain energy, the energy difference between these states is equivalent to the energy of radio waves of about 100 MHz. By monitoring the emission of the absorbed radio fre-

quency (RF) energy at either a fixed frequency and a sweeping magnetic field or fixing the magnetic field and sweeping the frequency of the RF radiation, a NMR spectrum can be recorded. The NMR shifts (δ , in ppm) were determined relative to the residual ^1H absorption of CHCl_3 (7.26 ppm) or to the ^{13}C resonance shift of CDCl_3 (77.16 ppm).

3.3 Atomic Force Microscopy

Scanning force microscopy or atomic force microscopy was invented in 1986 by Binnig, Quate and Gerber to circumvent the problem of STM being only able to measure conductive samples. They replaced the wire of an STM with a simple lever made out of a diamond at the end of a thin gold strip. With atomic force microscopy the tip height was controlled in such a way to keep the force between tip and sample constant. The resolution of such a system is in essence limited by the shape of the tip.^[3] As illustrated in figure 3.3 an atomic force microscope thus needs the following parts: a chip or cartridge to hold a cantilever with a probe (also called tip), a photo-detector, a laser/light source and a piezoactuator to move the sample on the micro/nanometer scale (not shown). The laser is set on the top of a reflecting cantilever so it hits the center of the detector, the probe is then brought into contact with the sample by moving the piezoactuator towards the tip. The tip is thereafter brought into the repulsive force regime (Fig. 3.4) and scanning at a constant cantilever deflection will be started. Any mechanical deviation is detected from a deviation of the laser spot on the photo-detector. The topography can be determined from this signal by moving the piezoactuator up or down depending on the shift of the spot on the photo-detector. Careful calibration of the piezoactuator thus results in accurate height measurements. The method of measurement as described here is commonly referred to as contact mode AFM and is a static mode. This technique is sensitive to the elasticity of the sample as any change in softness could possibly appear as a change in height.

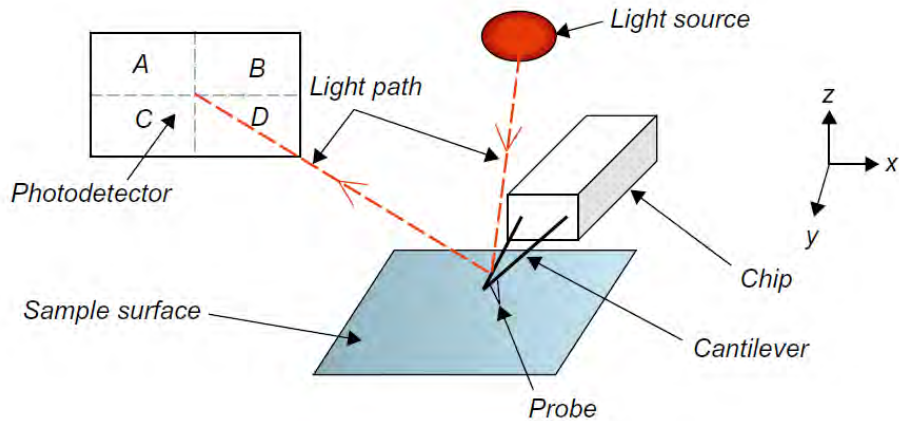


Figure 3.3: Basic overview of an AFM setup. Reprint from^[4]

The following sections will discuss the used AFM techniques and the inherent drawbacks and benefits of each technique.

3.3.1 Contact and Conductive AFM

As mentioned before in contact AFM the probe is brought into contact by moving the piezoactuator towards the tip, this will result in a perpendicular force which is given by Hooke's law ($F = -k \cdot \delta z$, with F the force applied during measurement, δz the deflection distance and k the force constant of the cantilever). This equation clearly shows that to minimize the forces on the sample, the force constant and the deflection setpoint need to be kept to a minimum. Generally speaking the cantilever has to be softer than the bonds between the bulk atoms in tip and sample. However, as figure 3.4 illustrates proper tip-sample contact is only ensured when working in the repulsive regime.

One of the biggest pitfalls in the analysis of contact-AFM images is the interpretation of height images, since the apparent height can be heavily influenced by the composition of the sample. Imagine an atomically flat sample consisting of two polymers with different mechanical proper-

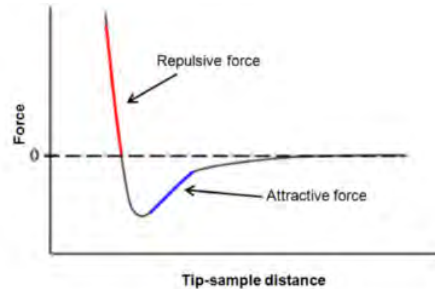


Figure 3.4: A standard force-distance curve as can be obtained from AFM. Reprint from^[19]

ties being imaged by contact AFM with a pre-set force, during scanning the polymers will display different indentations and thus will show a different apparent height. Furthermore, the operating principle of Contact AFM implies that during measurement the tip remains in full contact with the sample possibly resulting in either tip or sample damage. In addition to a perpendicular force a lateral force exists as well, which in turn will result in torsion of the cantilever. By detecting and analysing this torsion it is possible to determine the local friction properties.

Conductive AFM was derived from contact AFM in the mid 1990's to be able to measure currents through silicon gate dielectrics on the nano-scale.^[20] The main difference from standard contact AFM is the fact that a probe with a thin conductive metallic layer is brought into contact with the surface and a fixed voltage applied to simultaneously map topography and current. It is however possible to use a different measurement configuration in which the probe is fixed at a set position and the voltage is swept over a predefined range. Most of the time however, the techniques are combined as first a topographic and current mapping of the sample is done, followed by IV-spectroscopy on interesting areas e.g.: grain boundaries in copper indium gallium sulphur/selenium (CIGS), copper zinc tin sulphur/selenium (CZTS) samples or local measurements on phase separated materials.^[9,14,17]

In addition to the drawbacks of contact AFM such as sample and probe damage, conductive AFM can be heavily influenced by sample topography. A rough sample will have locations with an increased tip-sample contact area, thereby resulting in increased current. Or possibly, when measuring in ambient condition, a thin water meniscus can form on the sample surface and as a result show an increased conduction.^[16]

3.3.2 Dynamic AFM

A different option is the use of dynamic modes in which the cantilever oscillates near the sample surface. Two main modes exist: dynamic force microscopy and amplitude modulated atomic force microscopy (AM-AFM). In dynamic force microscopy, a self-driven cantilever (eigenfrequency f_0 , spring constant k) is subjected to a feedback loop as to have an oscillation at a frequency (f) with a constant amplitude (A). When in close proximity to the sample the forces between tip and sample will result in a small change in frequency and phase. These detected changes will go through a bandpass filter to remove any unwanted noise, the signal is thereafter interpreted into a topographical image. To be absolutely sure that the restoring force at the lower turning point (when tip movement changes from down to up) is larger than the attractive force between tip and sample an appropriately large oscillation amplitude has to be selected. To be able to use a self-driven cantilever the measurements need to proceed in vacuum, this removes any dampening from the surrounding atmosphere and results in high quality factors.

Compared to contact AFM dynamic force microscopy has the ability for true atomic resolution and this has been shown by Giessibl on a 7x7 reconstructed Si(111) surface.^[11] Moreover, other semiconductors such as TiO₂, InP, GaAs and InAs have been studied successfully as well.^[12]

CHAPTER 3. CHARACTERIZATION TECHNIQUES

Alternatively to frequency shift detection it is also possible to use the amplitude of the cantilever oscillations as a control parameter during AFM imaging. AM-AFM uses tip oscillation amplitudes of 20 to 100 nm at a frequency close to the resonance frequency of the cantilever. In this mode the root-mean-square value of the deflection detector is used as a control parameter for the tip-sample distance. The main benefit compared to contact AFM is a reduction in the lateral forces while maintaining a similar resolution only limited by the tip shape. This method is generally referred to as tapping AFM.

Similar to dynamic force microscopy the phase shift between excitation and cantilever oscillation can be used to obtain additional information, this is however limited to soft materials and when using sharp tips. In phase imaging local phase separation between materials tends to show up as contrast, however, this contrast can invert in between measurements and is therefore harder to interpret.

3.3.3 KPFM

The initial macroscopic Kelvin probe works based on the principle that if two metals are brought into electrical contact a current will flow from the metal with the lower work function to the metal of the higher work function which in turn will lead to a contact potential difference between the two metals.^[2] This idea was improved upon by William Zisman, who mounted a vibrating plate above the sample electrode. Due to the vibration of the plate the output voltage varies periodically. Moreover, the peak-to-peak voltage depends on the difference between the contact potential and the externally applied voltage. Thus any change in contact potential can be detected by varying the external potential to get a zero output voltage. This technique however averages over the entire plate area and therefore, has a severely reduced lateral resolution.^[25]

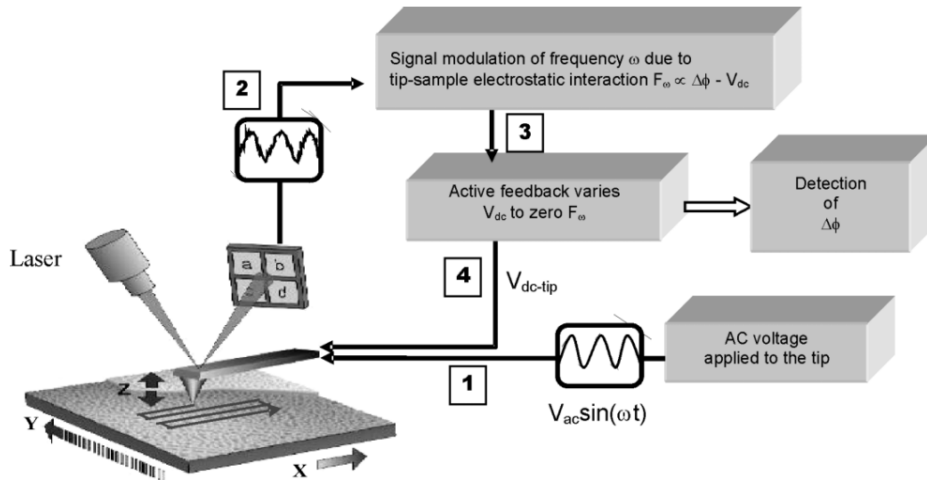


Figure 3.5: Overview of a KPFM setup

Nonnenmacher et al. were able to measure the local contact potential by modifying a standard AC force microscope by adding a heterodyne interferometer to detect the motion of the force sensor.^[22] Most modern microscopes now include the possibility of measuring local contact potential differences between tip and sample through either amplitude modulated KPFM (AM-KPFM) or frequency modulated KPFM (FM-KPFM).

Figure 3.5 shows an overview on how a KPFM can be implemented on an AFM. In a first step an alternating voltage V_{ac} is applied to the tip at a frequency ω . The resulting mechanical oscillation due to the electrostatic tip-sample interaction is detected on a photodiode. In the third step the oscillation of the cantilever is isolated via a lock-in amplifier and fed back into the circuit. In a final step this feedback is used to minimize $F_{\omega ac}$ by applying a DC bias voltage onto the tip.

The electrostatic force between tip and sample has a quadratic dependence on the difference between the tip bias voltage (V_{DC}) and the contact potential difference (V_{CPD}) between tip and sample and it is possible to model this using the simple model of a capacitor. The resulting electro-

static force in that case is

$$F_{el} = \frac{-1}{2} \frac{\partial C}{\partial z} [V_{dc} - V_{CPD} + V_{AC} \sin(\omega_{ACT})]^2 \quad (3.5)$$

$\partial C/\partial z$ is the capacitance gradient and V_{CPD} is the work function difference between the tip and the sample.

$$V_{CPD} = \frac{\Phi_{sample} - \Phi_{tip}}{q} \quad (3.6)$$

Expanding equation 3.5 allows one to write it as a sum of forces with $F_{el} = F_{dc} + F_{\omega_{AC}} + F_{2\omega_{ac}}$. The result of the first term F_{DC} (eq. 3.7) is a fixed deflection. The second term $F_{\omega_{ac}}$ (eq. 3.8) varies with the frequency of the applied electrical signal and is mainly used to determine the contact potential difference. The last term $F_{2\omega_{ac}}$ (eq. 3.9) does not depend on the contact potential difference and has been used to determine the local capacitance.

$$F_{dc} = -\frac{\partial C}{\partial z} \left[\frac{1}{2} (V_{dc} - V_{CPD})^2 + \frac{V_{AC}^2}{4} \right] \quad (3.7)$$

$$F_{\omega_{ac}} = -\frac{\partial C}{\partial z} (V_{dc} - V_{CPD}) V_{AC} \sin(\omega_{ACT}) \quad (3.8)$$

$$F_{2\omega_{ac}} = -\frac{\partial C}{\partial z} \frac{V_{AC}^2}{4} \cos(2\omega_{ACT}) \quad (3.9)$$

As can be seen from equation 3.6 to determine the absolute work function of the material under investigation the probe needs to be fully calibrated using a sample with a known work function. Moreover, to have an exact and absolute work function all measurements need to be done in ultra-high vacuum as the work function is very sensitive to any surface adsorbates.

As the definition of V_{CPD} ($\frac{\Phi_{sample} - \Phi_{tip}}{q}$ or $\frac{\Phi_{tip} - \Phi_{sample}}{q}$) tends to vary between different microscopes and software versions a selection of samples were prepared. The first two were a low (Al) work function metal^[18] and a

transparent conducting oxide (ITO)^[13], the second set consisted out of a MeOH treated and normal a PEDOT:PSS layer^[24] covering this surface. The results are shown in figure 3.6, it can be clearly seen that V_{CPD} behaves as the opposite of the work function. I.e. a decrease in surface potential correlates to an increase in work function. Moreover, this implicates that the effective work function of the tip as used here is in the order of 5.2 eV making it a nice average for the quoted values for platinum and iridium.

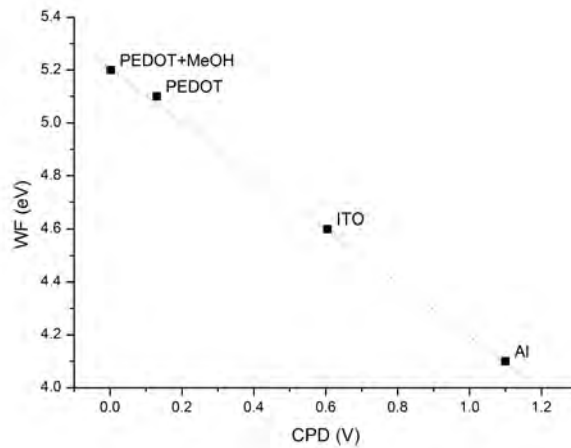


Figure 3.6: Plot of several reference materials (Al, ITO, PEDOT, MeOH treated PEDOT) to determine the correct definition of the contact potential difference.

3.3.4 PeakForce Tapping and TUNA

PeakForce tapping (PF-Tapping) is a novel measurement mode for AFM. It uses a standard AFM probe and differs by not oscillating the probe at or near resonance frequency but instead uses a low frequency oscillation (1-2 kHz) of either probe or piezo-actuator. Each time the AFM tip touches the surface a force-distance curve is captured by the AFM controller and analysed. The nature of this technique completely removes any lateral force component while keeping the resulting perpendicular force on the sample to a minimum.

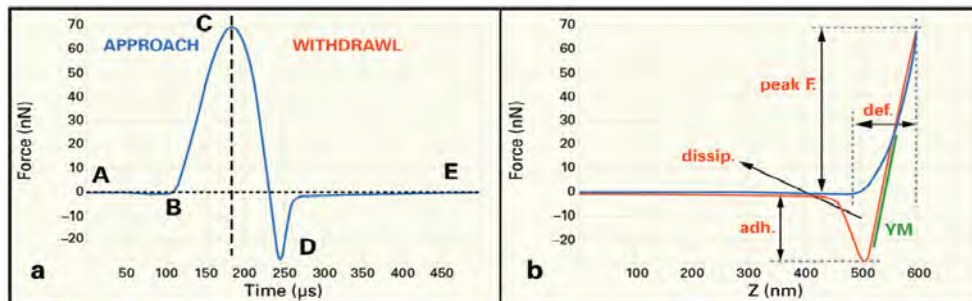


Figure 3.7: (a) A single curve as obtained by Peak Force Tapping. (b) The curve from (a) reworked into a force distance curve. From this curve different mechanical properties such as adhesion, energy dissipation and Young's modulus can be estimated.^[10]

Figure 3.7 shows a single curve obtained by PeakForce Tapping and the corresponding force-distance curve as used for analysis of morphology and corresponding mechanical properties by employing the Darjaguin-Muller-Toporov (DMT) model of elastic contact. As a single linescan takes 1 second and an average number of 512 points per line is selected this leads to an averaging of 3 to 4 of these force-distance curves per pixel. The processing power needed to analyse force-distance curves on the fly is rather high therefore, any fits based on this model are done by the AFM controller and sent to the software afterwards.^[5]

To be able to compare absolute values measured for the mechanical properties all tips need to be fully characterized. This characterization is a three step process, in the first the deflection sensitivity is characterized by analyzing a force-distance curve on an extremely hard sample. The second step is a thermal tuning of the cantilever to determine the spring constant. The final step is a characterization of a sample with a known hardness to set the correct parameters for subsequent imaging. However, for bulk heterojunction organic solar cells relative differences within a single sample are sufficient as one is more interested to determine whether or not phase separation is present. Moreover, by omitting the characterization steps as described above any expected initial tip damage is pre-

vented.

PeakForce tunnelling AFM (PF-TUNA) works in a similar fashion as PeakForce Tapping with the addition of current sensing capabilities. The main difference with standard conductive AFM is the time that the AFM probe is in contact with the sample. Figure 3.8 shows the definition of the different currents that are measured during PeakForce TUNA. The first current is defined as the Peak Current, this is measured at maximum force during a force distance curve. The second current is called the Contact Current and defined as the current measured during the time when the AFM probe is in contact with the sample. The third and final current is termed the TUNA current and is defined as the number of charges measured over the entire measurement time of a single force distance curve.^[6]

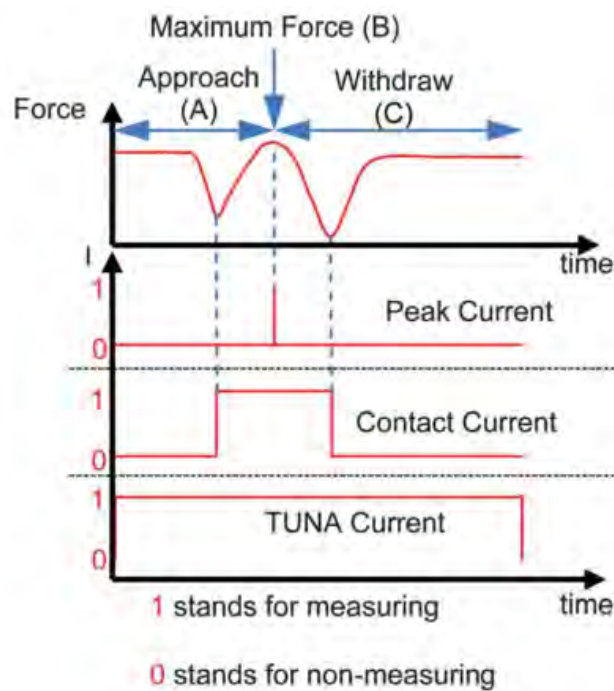


Figure 3.8: Overview of the different currents measured with PeakForce TUNA.^[8]

CHAPTER 3. CHARACTERIZATION TECHNIQUES

Of all currents the Contact Current is most closely related to the current as measured by conductive AFM however, there will be some discrepancies as the force applied during PeakForce Tapping and TUNA can be as low as 50 pN while C-AFM can be down to the sub-nN range.^[8]

A small overview of the electrical AFM techniques with corresponding typical resolution and used tips can be found in table 3.1. The electrical and topographical resolution of C-AFM and PF-TUNA is similar however, the topography image resulting from PeakForce TUNA is far less distorted compared to a topography image of C-AFM due to the severely reduced lateral force. An example of this can be found in chapter 4 section 4.2.4 on figures 4.28 (c and i) and 4.29 (a and b) on page 89 and 92

Table 3.1: Overview of the electrical techniques with the corresponding probes.

	C-AFM	PF-TUNA	KPFM
Typical x-y resolution	25 nm ^[15]	25 nm ^[15]	25 nm ^[19]
Typical z resolution	0.5 nm	0.5 nm	0.5 nm
Resolution limiting factors	Tip diameter,z-scanner	Tip diameter,z-scanner	Tip diameter,z-scanner
Type of contact	Contact	Intermittant contact	Non contact Tapping mode
Tip coating	Pt/Ir	Pt/Ir	Pt/Ir
Quoted spring constant	~0.4 N/m	~0.4 N/m	4.0 N/m
Quoted tip resonant frequency	~70 kHz	~70 kHz	~75 kHz
Single or Double pass	Single	Single	Double
Type	PFTUNA	PFTUNA	SCM-PIT

Nanoscale characterization was done on a Bruker Multimode 8 AFM with a V series controller either in ambient atmosphere or in an inert N₂ atmosphere with a relative humidity less than 6%. The relative humidity was monitored using a home built set-up based on relative humidity sensors with an accuracy of 3%.

Bibliography

- [1] S. Altazin, R. Clerc, R. Gwoziecki, G. Pananakakis, G. Ghibaudo, and C. Serbutoviez. Analytical modeling of organic solar cells and photodiodes. *Applied Physics Letters*, 99(14):143301, 2011.
- [2] A. Bennett and C. Duke. Self-Consistent-Field Model of Bimetallic Interfaces. I. Dipole Effects. *Physical Review*, 160(3):541–553, Aug. 1967.
- [3] G. Binnig, C. Quate, and C. Gerber. Atomic force microscope. *Physical review letters*, 56(9), 1986.
- [4] R. W. Bowen and N. Hilal. *Atomic Force Microscopy in Process Engineering*. Elsevier Ltd, 2009.
- [5] Bruker. PeakForce QNM - Quantitative Nanomechanical Property Mapping, 2010.
- [6] Bruker. PeakForce TUNA - Nanoelectrical Application Module, 2010.
- [7] A. Cheknane, H. S. Hilal, F. Djeflal, B. Benyoucef, and J.-P. Charles. An equivalent circuit approach to organic solar cell modelling. *Microelectronics Journal*, 39(10):1173–1180, Oct. 2008.
- [8] S. Desbief, N. Hergué, O. Douhéret, M. Surin, P. Dubois, Y. Geerts, R. Lazzaroni, and P. Leclère. Nanoscale investigation of the electrical properties in semiconductor polymer-carbon nanotube hybrid materials. *Nanoscale*, 4(8):2705–12, Apr. 2012.
- [9] O. Douhéret, L. Lutsen, A. Swinnen, M. Bresselge, K. Vandewal, L. Goris, and J. Manca. Nanoscale electrical characterization of organic photovoltaic blends by conductive atomic force microscopy. *Applied Physics Letters*, 89(3):032107, 2006.
- [10] B. Foster. New atomic force microscopy (AFM) approaches life sciences gently, quantitatively, and correlatively. *American laboratory*, (APRIL):24–27, 2012.

BIBLIOGRAPHY

- [11] F. Giessibl. Atomic resolution of the silicon (111)-(7x7) surface by atomic force microscopy. *Science*, (13):1–4, 1995.
- [12] F. J. Giessibl. AFM's path to atomic resolution. *Materials Today*, 8(5):32–41, May 2005.
- [13] S. JEE, S. KIM, J. KO, and Y. YOON. Study on work function change of ITO modified by using a self-assembled monolayer for organic based devices. *Journal of the Korean Physical Society*, 49(5):2034–2039, 2006.
- [14] M. Kawamura, T. Yamada, N. Suyama, A. Yamada, and M. Konagai. Grain Boundary Evaluation of $\text{Cu}(\text{In}_{1-x}\text{Ga}_x)_2\text{Se}_2$ Solar Cells. *Japanese Journal of Applied Physics*, 49(6):062301, June 2010.
- [15] K. M. Lang, D. a. Hite, R. W. Simmonds, R. McDermott, D. P. Pappas, and J. M. Martinis. Conducting atomic force microscopy for nanoscale tunnel barrier characterization. *Review of Scientific Instruments*, 75(8):2726–2731, Aug. 2004.
- [16] M. Lanza, M. Porti, M. Nafría, X. Aymerich, E. Whittaker, and B. Hamilton. UHV CAFM characterization of high-k dielectrics: Effect of the technique resolution on the pre- and post-breakdown electrical measurements. *Microelectronics Reliability*, 50(9-11):1312–1315, Sept. 2010.
- [17] J. B. Li, V. Chawla, and B. M. Clemens. Investigating the role of grain boundaries in CZTS and CZTSSe thin film solar cells with scanning probe microscopy. *Advanced materials (Deerfield Beach, Fla.)*, 24(6):720–3, Feb. 2012.
- [18] K. Maturova, S. S. van Bavel, M. M. Wienk, R. a. J. Janssen, and M. Kemmerink. Description of the Morphology Dependent Charge Transport and Performance of Polymer:Fullerene Bulk Heterojunction Solar Cells. *Advanced Functional Materials*, 21(2):261–269, Jan. 2011.

BIBLIOGRAPHY

- [19] W. Melitz, J. Shen, A. C. Kummel, and S. Lee. Kelvin probe force microscopy and its application. *Surface Science Reports*, 66(1):1–27, Jan. 2011.
- [20] M. P. Murrell, M. E. Welland, S. J. O’Shea, T. M. H. Wong, J. R. Barnes, A. W. McKinnon, M. Heyns, and S. Verhaverbeke. Spatially resolved electrical measurements of SiO₂ gate oxides using atomic force microscopy. *Applied Physics Letters*, 62(7):786, 1993.
- [21] G. Namkoong, J. Kong, M. Samson, I.-W. Hwang, and K. Lee. Active layer thickness effect on the recombination process of PCDTBT:PC71BM organic solar cells. *Organic Electronics*, 14(1):74–79, Jan. 2013.
- [22] M. Nonnenmacher, M. P. O’Boyle, and H. K. Wickramasinghe. Kelvin probe force microscopy. *Applied Physics Letters*, 58(25):2921, 1991.
- [23] R. Silverstein, G. Bassler, and T. C. Morrill. *Spectrometric Identification of Organic Compounds*. 1991.
- [24] H. Zhou, Y. Zhang, J. Seifert, S. D. Collins, C. Luo, G. C. Bazan, T.-Q. Nguyen, and A. J. Heeger. High-Efficiency Polymer Solar Cells Enhanced by Solvent Treatment. *Advanced materials (Deerfield Beach, Fla.)*, pages 1646–1652, Jan. 2013.
- [25] W. a. Zisman. a New Method of Measuring Contact Potential Differences in Metals. *Review of Scientific Instruments*, 3(7):367, 1932.

Part II

Results and discussion

Chapter 4

Results and Discussion

4.1 Charge injection and extraction in Polymer/Donor:acceptor blends

4.1.1 Introduction

Organic solar cells are usually based on the bulk heterojunction concept in which electron donor and acceptor molecules are deposited together to form an intermixed film. How fine these materials mingle will in part determine the efficiency of the final solar cell.^[70] However, as this type of intermixing is happening on the nanoscale, characterization techniques with a resolution at the same scale are needed. Atomic force microscopy and derived techniques are extremely well suited for this type of research as they combine a non-destructive nature with a high lateral resolution. Moreover, these techniques have been successfully employed to study the local electrical properties of organic semiconductors.^[9,20,22,58,60,71,89] To be able to effectively describe the nature of charge transport between a metal contact (or conductive AFM tip) and a semiconducting polymer it is of the utmost importance to get information on the barrier existing between the two materials. This is mainly due to the fact that charge injection (extraction) at a metal contact into (from) an organic semicon-

ductor is heavily influenced by the nature of the contact between the two materials. Having perfect alignment between the metal's work function and HOMO or LUMO levels is not needed, however, the discrepancy in energy levels between the two materials can't be too large and it is on this premise that currently local IV-curves are analysed.^[22,58,71] Moreover, early work places the barrier at which transport changes from bulk to injection limited current at 0.3 to about 0.4 eV thereby confirming the validity of using ohmic transport.^[19] Contrary to fixed barriers, more recent work describes an intermediate quasi-ohmic region with varying limits.^[87] Selection of a proper model to describe the measured data is the only way to ensure that the extracted parameters can be attributed to real physical processes. This section will show that depending on the barrier between tip and sample either ohmic conduction and with it space charge limited current is valid or that a Poole-Frenkel type conduction between tip and sample exists.^[26]

4.1.2 Determining the tip/sample barrier for injection

Kelvin Probe Force Microscopy is ideally suited to determine the tip sample barrier as it works on the presupposition of determining the work function difference between the probe and the metal under investigation. In the case of semiconductors however, the difference between the work function of the tip and the fermi level of the semiconductor is measured.^[3,4,73] However, organic semiconductors do not have the classic definition of a work function such as traditional semiconductors making the interpretation of kelvin probe force microscopy data far more difficult.^[66]

As shown in section 3.3.3 the contact potential difference is defined as $V_{CPD} = \frac{\Phi_{tip} - \Phi_{sample}}{q}$. Therefore by analysing both the V_{CPD} of the aluminium cathode and the blend (or pure organic layer) it is possible to estimate the difference of the work function of the metal and the surface poten-

CHAPTER 4. RESULTS AND DISCUSSION

tial of the polymer. This allows a direct comparison of different areas of a single sample irrespective of the work function of the used AFM tip as long as the AFM tip is not changed within the measurement of a single sample. The effect of composition, thickness and substrate will be determined in the following sections. To this end three different samples sets were analysed by KPFM. The first set composed of P3HT:PCBM films with varying ratios deposited on poly(3,4-ethylenedioxythiophene) polystyrene sulfonate (PEDOT:PSS) on ITO/glass. The second set consisted out of P3HT layers with varying thickness spincoated on PEDOT:PSS on ITO/glass. The third sample set investigated the effect of PEDOT:PSS as an interlayer in between P3HT:PCBM and ITO the surface potential of P3HT:PCBM as measured by KPFM. Finally, the I-V curves as obtained by C-AFM from different polymers were analysed to confirm the proposed injection and transport model. The experimental details can be found in IV.

Table 4.1 shows the measured surface potential from KPFM on a set of P3HT:PCBM samples with a varying composition, these results already show that the absolute value of the contact potential difference between tip and blend is in the order of 0.2 to about 0.4 eV. Another very interesting point to note is that the V_{CPD} of pure P3HT and for P3HT:PCBM blends is positive, while pure PCBM has a negative contact potential difference. This strongly indicates that the presence of PCBM in the blend does not have an influence on the tip sample barrier. However, there is a distinct possibility that the P3HT:PCBM shows vertical phase separation and that the resulting surface potential is solely due to the presence of P3HT.^[91] Interestingly the blend with the highest PCBM content also has the highest contact potential difference, which is completely counter intuitive when comparing to the contact potential difference of pure PCBM (-0.23 eV). These results show that the measured contact potential difference on aluminium is very stable, moreover, a work function of 4.1 eV for aluminium^[56] would set the work function of the AFM tip to 5.5 eV which is high but not impossible for the materials (platinum/iridium (Pt/Ir)) making up the AFM tip.^[45,78] This

CHAPTER 4. RESULTS AND DISCUSSION

work function for the AFM tip would set the measured energy level of the pure P3HT to about 5 eV which is very close to the HOMO level of P3HT as this is generally cited at 5.1 eV.^[58] When applying a similar correction for the ITO substrate it can be seen that V_{CPD} as measured here coincide with the fermi levels as quoted in literature, however, the variation is larger as the PEDOT:PSS and polymer covering the ITO have to be removed.^[38] The removal of PEDOT:PSS consisted out of a thorough scrubbing with a q-tip dipped in H₂O. Any remaining PEDOT:PSS and a water meniscus could have a significant effect on the eventual work function and can explain the large variation when comparing these values for ITO.^[4]

Table 4.1: The measured surface potential of P3HT:PCBM thin films in different ratio's with an aluminium contact deposited on top.

Sample	Al (V)	Blend (V)	ITO (V)	Corrected energy level - Blend (eV)	Corrected energy level - ITO (eV)
Pure P3HT	1.36 ± 0.01	0.39 ± 0.01	0.73 ± 0.01	5.07 ± 0.02	4.74 ± 0.02
Pure PCBM	1.39 ± 0.01	-0.23 ± 0.01	0.54 ± 0.01	5.72 ± 0.02	4.95 ± 0.02
P3HT:PCBM 1:1	1.42 ± 0.02	0.30 ± 0.05	0.90 ± 0.04	5.22 ± 0.07	4.62 ± 0.06
P3HT:PCBM 1:2	1.38 ± 0.02	0.40 ± 0.05	0.85 ± 0.04	5.08 ± 0.07	4.63 ± 0.06
P3HT:PCBM 2:1	1.35 ± 0.02	0.22 ± 0.05	0.88 ± 0.04	5.23 ± 0.07	4.57 ± 0.06

To exclude vertical phase separation the samples containing P3HT were imaged by C-AFM at a fixed voltage. The results are shown in figure 4.1 and images at a positive bias clearly show that the addition of PCBM results in areas with a considerable increased conduction. Applying a negative bias during C-AFM imaging results in areas showing no conduction and the location of these non-conducting regions coincide with the spikes seen at positive bias. A similar behaviour was seen by Rice et. al. when using P3HT nanowires in combination with PC₆₁BM.^[72] Therefore, it is safe to say that the P3HT and PCBM are finely intermixed and that the amount of PCBM in this case shows no significant influence on the surface potential. A similar result was seen by Xu et. al. when using photoelectron spectroscopy on various P3HT:PCBM blends, they show the formation of a P3HT rich layer at the surface.^[90] This is not necessarily contradictory to the results found here. A layer can be P3HT rich but still contain a decent

amount of PCBM to show up in the conductive AFM measurements.

Moreover, to be absolutely sure on the interpretation of these spikes, current-voltage curves on pure P3HT, pure PCBM and on a sample with a 2:1 ratio of P3HT:PCBM were made. The shown JV-curves were all measured by the same tip and were corrected for the area of the tip, which in turn was determined by SEM. The current-voltage curve on pure PCBM (Fig. 4.2 (a)) evidently shows no contribution from -10 to 0 V, undeniably exhibiting that any conduction measured by AFM on a mixture with PCBM under negative bias can be solely attributed to the other components in the mixture. There even is no measurable current with a sample bias up to 2.5 V, however, beyond this value the current unquestionably starts to increase exponentially. Current-voltage curves measured on pure P3HT (Fig. 4.2 (b)) show a radically different behaviour, a significant amount of current can be measured at all times except at zero bias. However, at a bias of 10 V the current through PCBM is about two orders of magnitude higher than the current through P3HT. Finally the current-voltage characteristics on a P3HT:PCBM mixture were measured, more specifically an area exhibiting both a contribution of PCBM and P3HT was targeted, this is displayed in figure 4.2 (c). These results clearly show that any current at a low bias passes through the P3HT while if the applied bias is a high enough current will start to flow through the PCBM, suggesting the existence of a PCBM path towards the PEDOT:PSS through which current can flow. More important, it is additional proof that PCBM is present at the surface.

To exclude any other surface effects and further elucidate the surface potential difference between the aluminium contact and the polymer film, the KPFM tip was replaced and the P3HT:PCBM mixtures were re-evaluated. Both tables (4.1 and 4.3) show near identical results, the calculated difference between blend and sample remains at a near constant value of ~ 1.0 V. Moreover, using a similar correction as before suggests a tip work

CHAPTER 4. RESULTS AND DISCUSSION

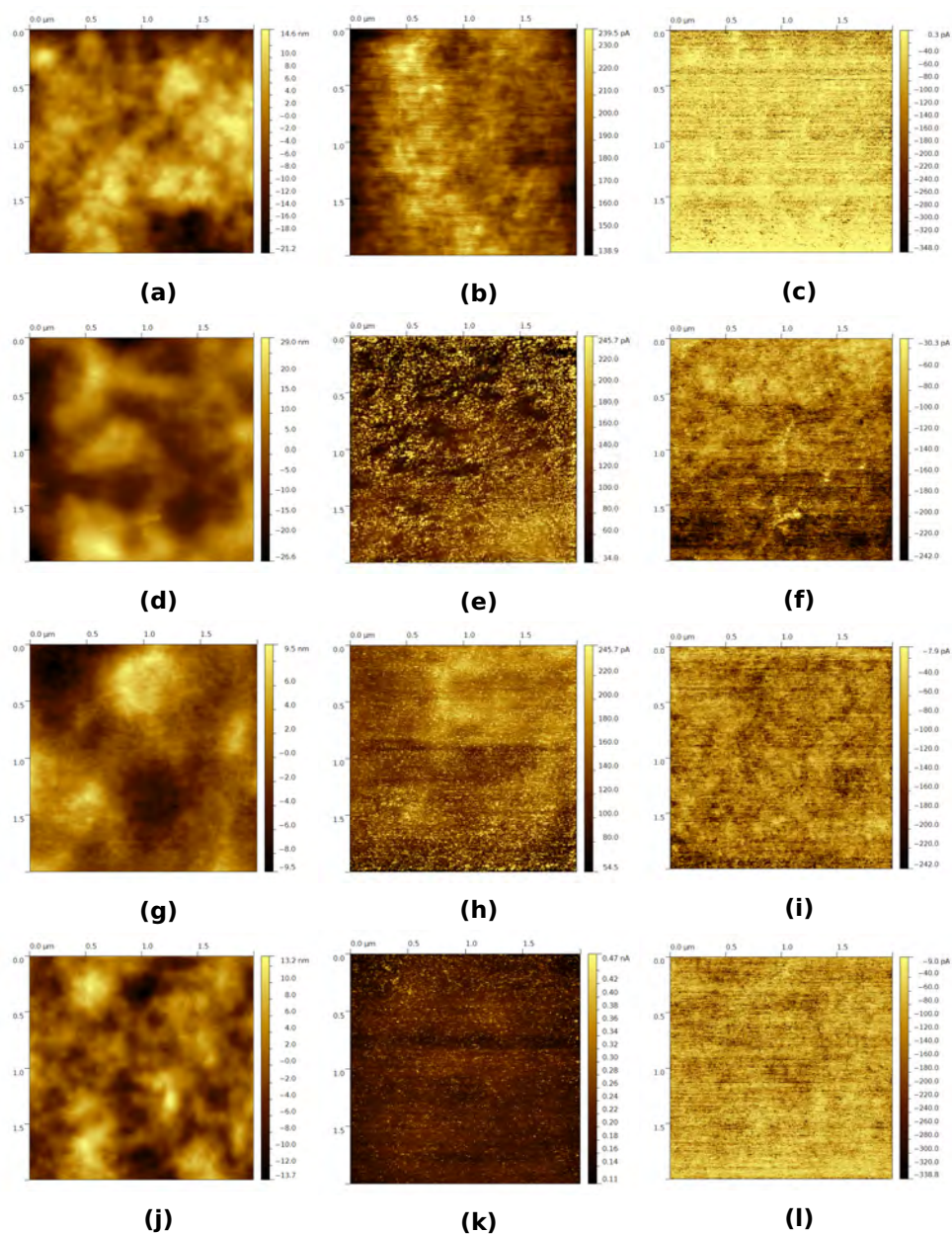


Figure 4.1: An overview of topography and corresponding conductive AFM images on pure P3HT (a,b,c), P3HT:PCBM (1:1) (d,e,f), P3HT:PCBM (1:2) (g,h,i) and P3HT:PCBM (2:1) (j,k,l). The first column always represents the measured morphology on a 2 by 2 μm² scale. Column number two represents the measured current at a fixed positive sample bias (5 V), the average current of the respective images is 190 pA, 130 pA, 160 pA, 210 pA. While the third column shows the measured current at a fixed negative bias (-5 V), the average current of the respective images is -40 pA, -130 pA, -100 pA, -100 pA.

CHAPTER 4. RESULTS AND DISCUSSION

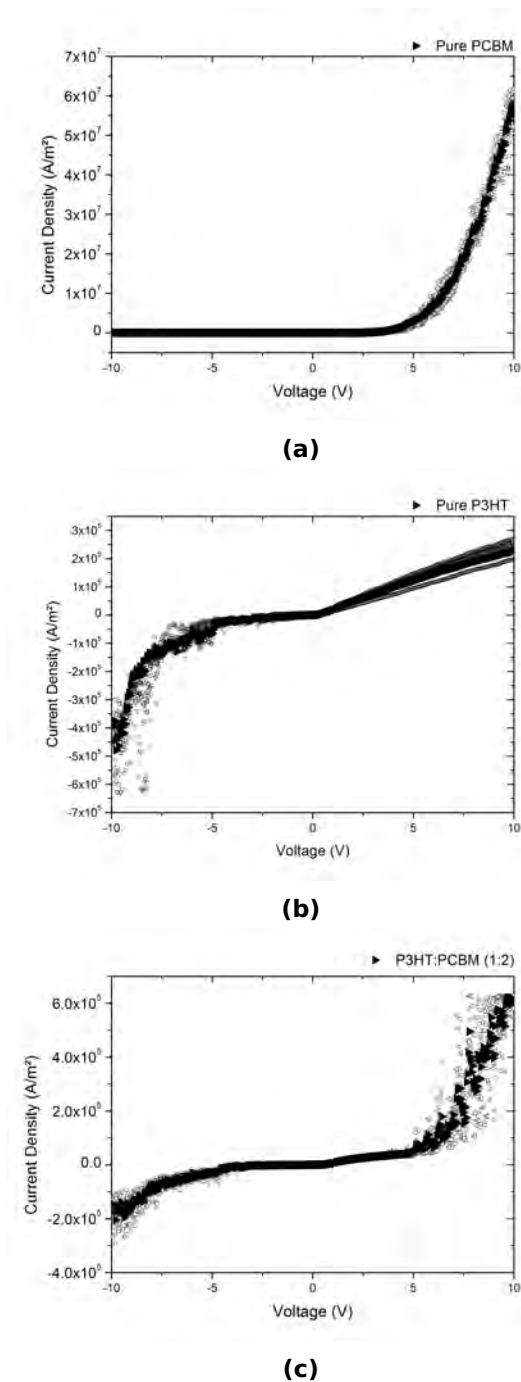


Figure 4.2: Current-voltage curves measured on Pure PCBM (a), pure P3HT (b) and P3HT:PCBM in a 1 to 2 ratio (c). The black solid triangles represent the average curve from 5 measurements, the respective standard deviations as calculated at 10 V are: 4.9×10^6 , 2.4×10^4 and $1.7 \times 10^4 A/m^2$.

CHAPTER 4. RESULTS AND DISCUSSION

function near 5.4 eV which is somewhat higher than the quoted values in literature.^[58,59] There is a slight discrepancy between the results in table 4.1 and those presented in 4.2, however, as some time passed (96-120h) between the initial measurement and the follow-up experiment a surface modification due to illumination or exposure to minute traces of oxygen or water could have had a profound effect on the surface potential.^[4]

Table 4.2: Contact potential difference results as obtained by KPFM on P3HT:PCBM at different ratios of P3HT:PCBM with a new tip.

Sample	Al (V)	Blend (V)	ITO (V)	Corrected energy level - Blend (eV)	Corrected energy level - ITO (eV)
P3HT:PCBM 1:1	1.26 ± 0.02	0.28 ± 0.01	0.414 ± 0.01	5.08 ± 0.03	4.95 ± 0.03
P3HT:PCBM 1:2	1.25 ± 0.01	0.27 ± 0.01	0.495 ± 0.01	5.08 ± 0.02	4.86 ± 0.02
P3HT:PCBM 2:1	1.25 ± 0.01	0.28 ± 0.01	0.552 ± 0.01	5.07 ± 0.02	4.80 ± 0.02

Table 4.3 shows the results for a fresh sample set and measured with a new tip. Again showing very little spread on the contact potential difference of the aluminium contact and suggesting that this AFM tip has a work function at around 5.2 to 5.3 electron volts. The surface potential difference between the aluminium and the P3HT:PCBM blend is always of the same order of magnitude and the correction, as done before, puts the measured values at the HOMO level of pure P3HT. These samples were treated with the utmost care as to limit any exposure to oxygen/water and/or illumination and the corresponding effect on surface potential. This set of samples was hereafter analysed with conductive AFM, the results and corresponding discussion can be found in section 4.1.3

Table 4.3: A novel set of P3HT:PCBM mixtures of different ratios measured with KPFM.

Sample	Al (V)	Blend (V)	ITO (V)	Corrected energy level - Blend (eV)	Corrected energy level - ITO (eV)
P3HT:PCBM 1:1	1.15 ± 0.01	0.11 ± 0.01	0.49 ± 0.01	5.15 ± 0.02	4.76 ± 0.02
P3HT:PCBM 1:2	1.12 ± 0.01	0.10 ± 0.01	0.57 ± 0.01	5.12 ± 0.02	4.65 ± 0.02
P3HT:PCBM 2:1	1.13 ± 0.01	0.20 ± 0.01	0.57 ± 0.01	5.03 ± 0.02	4.66 ± 0.02

It is well known that P3HT has the tendency to form different types of morphologies depending on the deposition and preparation method.^[11]

CHAPTER 4. RESULTS AND DISCUSSION

To rule out any effect of the crystallinity of P3HT in P3HT:PCBM on the surface potential a set of PCDTBT:PC₇₁BM ([6,6]-phenyl C71 butyric acid methyl ester (PC₇₁BM)) samples was measured as it is generally accepted that PCDTBT is amorphous.^[15] The outcome of this experiment can be found in table 4.4, in this case the PCBM content was varied from a simple 1:1 ratio to a 1:8 ratio. The results show surface potential values of 0.9 V on the aluminium contact suggesting a tip work function of 5.0 eV and a calculated energy level of 5.3 to 5.4 eV for PCDTBT:PC₇₁BM which again corresponds to highest occupied molecular orbital values quoted in literature (5.4 eV) for PCDTBT.^[5,42]

Table 4.4: PCDTBT:PC₇₁BM at different ratios measured by KPFM.

Sample	Al (V)	Blend (V)	ITO (V)	Corrected energy level - Blend (eV)	Corrected energy level - ITO (eV)
PCDTBT:PC ₇₁ BM 1:1	0.91 ± 0.01	-0.30 ± 0.05	0.53 ± 0.02	5.31 ± 0.06	4.48 ± 0.03
PCDTBT:PC ₇₁ BM 1:2	0.88 ± 0.02	-0.37 ± 0.04	0.56 ± 0.02	5.35 ± 0.06	4.42 ± 0.04
PCDTBT:PC ₇₁ BM 1:4	0.94 ± 0.02	-0.38 ± 0.02	0.60 ± 0.04	5.42 ± 0.04	4.44 ± 0.06
PCDTBT:PC ₇₁ BM 1:8	0.90 ± 0.02	-0.35 ± 0.02	0.70 ± 0.02	5.35 ± 0.04	4.30 ± 0.04

To preclude the effect of band bending a set of samples with varying P3HT thickness by spincoating at different speeds were measured with KPFM and Dektak.^[46,65] The results are displayed in table 4.5, and illustrate that the surface potential is independent of film thickness at least with a thickness larger than 30 nm. Thereby showing that any band bending does not become an issue at the thickness used in this work. Moreover, any band bending at the tip sample interface should be limited as there is no physical contact between tip and sample during KPFM imaging.

Table 4.5: Contact potential differences as measured by KPFM on P3HT layers of varying thickness.

P3HT film thickness	Al	P3HT Film	Corrected energy level - P3HT
270 nm	1.44 ± 0.01	0.47 ± 0.02	5.07 ± 0.03
140 nm	1.41 ± 0.01	0.41 ± 0.02	5.13 ± 0.03
90 nm	1.37 ± 0.01	0.41 ± 0.03	5.06 ± 0.04
50 nm	1.39 ± 0.01	0.32 ± 0.02	5.17 ± 0.03
30 nm	1.38 ± 0.01	0.29 ± 0.02	5.19 ± 0.03

The results obtained with KPFM here show that effectively the measured contact potential difference can be treated as an offset in work function of the metal probe and the HOMO level of the donor. Moreover, the results obtained with KPFM show that there appears to be a variation between the work functions of different AFM probes suggesting that when similar probes are used for conductive AFM the results are not always directly comparable in between different measurements.

4.1.3 Conduction mechanisms for pure films and blends

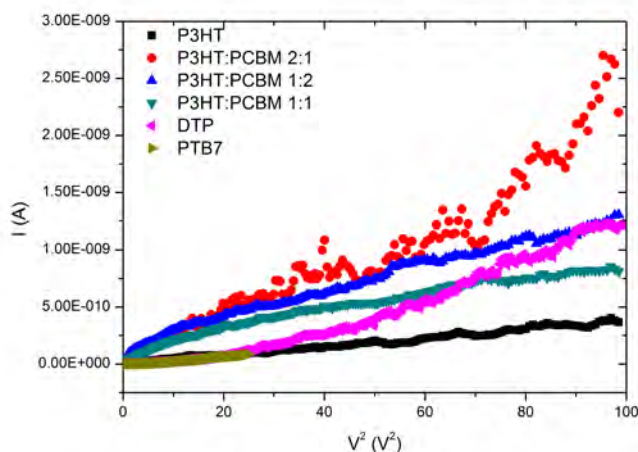


Figure 4.3: Current-voltage curves as obtained by C-AFM in an SCLC type plot. Only the curve obtained on pure P3HT seems to show a linear behaviour in this plot.

Space charge limited current is a widely used model to describe current transport in organic semiconductors.^[13,40,68,75] One of the prime requirements however, is the necessity of an ohmic contact between the contacts and the organic material under investigation. Moreover, the alignment of the contact's Fermi level with either HOMO or LUMO of the material allows a study of either hole or electron transport. In case of SCLC transport, when plotting the current in function of the square of the applied tip bias

a straight line is expected. Figure 4.3 shows such a plot of the current measured by C-AFM in function of the square of the applied tips bias for different organic materials either in blend or as a pure material.

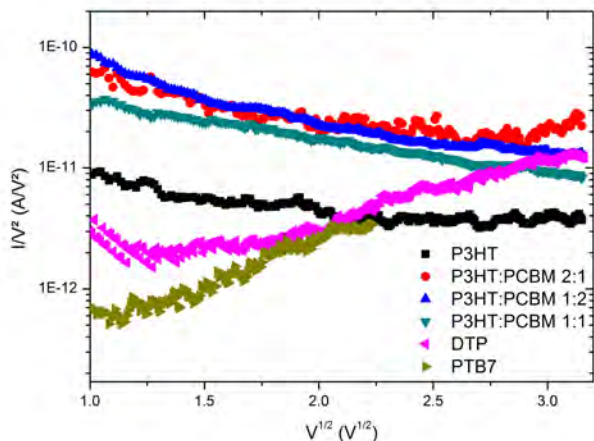


Figure 4.4: Current-voltage curves in an SCLC type plot with a field dependent mobility, in which none of the curves appear to change linearly.

An extension to space charge limited current exists in the form of using a field dependent mobility, this is more generally referred to as a modified Mott-Gurney and uses a Poole-Frenkel form for the mobility, which should result in a linear dependence of I/V^2 to $V^{1/2}$. Figure 4.4 shows a plot for different organic materials of I/V^2 in function of $V^{1/2}$ and as there is no linear dependence this is not a viable option to describe the local current, moreover, the fact that the slope is negative in the case of P3HT and P3HT:PCBM suggests a negative value for β , the strength of the field-dependence, which has no physical meaning. It can be clearly seen that a space charge limited type of current does not give the correct dependence, the primary reason for this is most likely the mismatch in work function between the metal AFM tip and the polymer thin film.

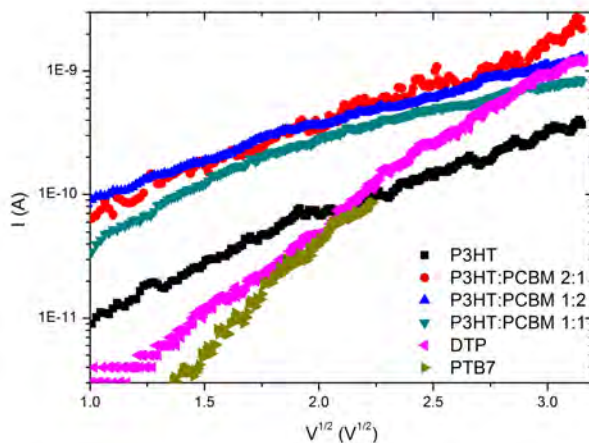


Figure 4.5: The data obtained from C-AFM in a Schottky plot, again the curves do not appear to show any linear behaviour in this type of plot.

Generally speaking a Schottky type contact is referred to as a rectifying contact between a metal and a semiconductor. These rectifying properties are similar to those of a PN junction. The associated equation shows that when plotting the current in function of the square root of the applied voltage a linear dependence should assert itself, not taking into account a field dependent barrier. Figure 4.5 shows the current in function of the square root of the applied voltage. However, the results displayed here imply that the model is not valid in the case of a metal AFM tip on the organic semiconductors as studied in this work.

Fowler-Nordheim tunnelling differs from direct tunneling only by the shape of the tunneling barrier. Direct tunneling has tunneling through the complete barrier while Fowler Nordheim tunnelling has a triangular shaped barrier. To determine whether or not this type of tunnelling is valid I/V^2 will be plotted in function of $1/V$. Figure 4.6 displays a set of curves with I/V^2 in function of $1/V$, the results here indicate that Fowler Nordheim Tunneling is not a valid model to describe charge injection across a barrier in the case of a metal AFM tip and an organic semiconductor.

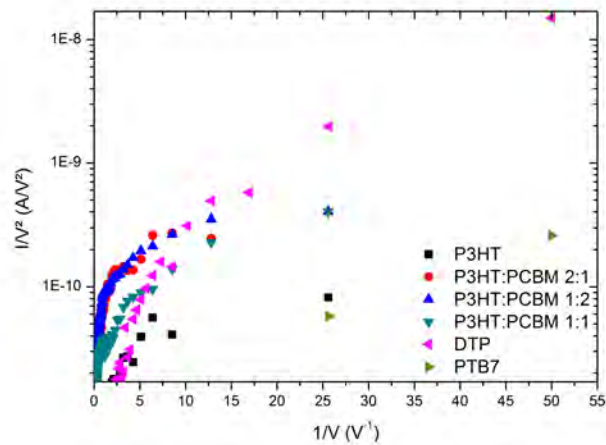


Figure 4.6: Fowler Nordheim plot of the local IV data. The presented curves do not appear to be linear.

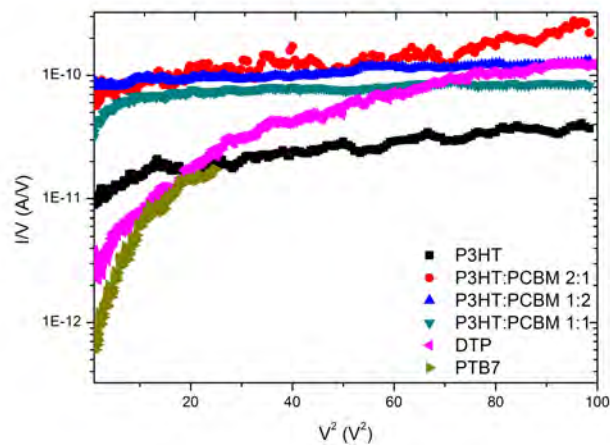


Figure 4.7: Current voltage data represented according to thermionic emission, in this case J/V does not appear to change linearly with V^2

Figure 4.7 shows the current plotted in a thermionic field emission plot, again, this model does not appear to be valid to describe the local current voltage curves as obtained by C-AFM measurement on the organic semiconductors studied in this manuscript.

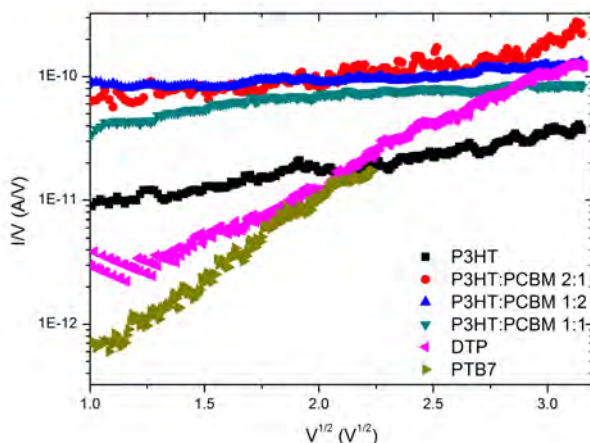


Figure 4.8: Poole Frenkel type plot, all the curves appear to have a linear relationship in this type of plot.

Figure 4.8 shows I/V in function of $V^{1/2}$, which appears to be linear for all the samples studied. The Poole Frenkel type charge injection, which is a combination between Schottky type charge injection and hopping transport through the polymer. Therefore, this seems to be a valid model to describe current injection and transport in organic semiconductors in a C-AFM measurement configuration. It should be no surprise that this could be a valid model for organic semiconductors as hopping transport has been shown to be valid in a wide range of organic semiconductors.^[26]

The question now remains, what defines when space charge limited current is valid and when Poole-Frenkel is to be applied. To this end the current voltage curves of samples with varying injection barriers were compared. Figure 4.9 shows a comparison between local IV-curves either plotted ac-

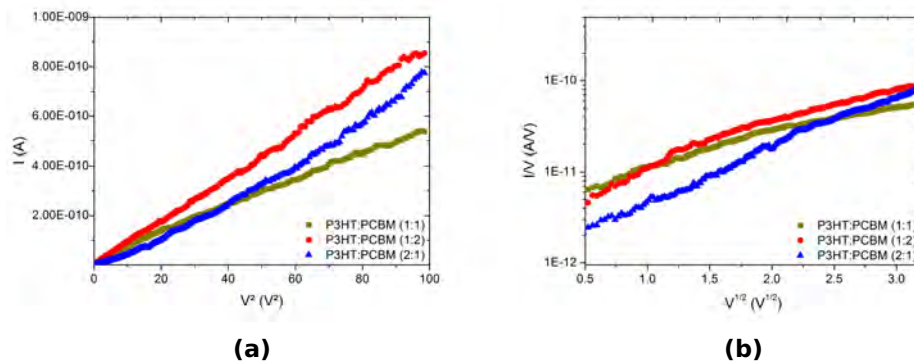


Figure 4.9: Direct comparison of local current voltage data obtained by conductive AFM plot according to the SCLC (a) and the Poole Frenkel model (b).

according to space charge limited current or according to Poole-Frenkel of the samples in table 4.3. The two samples which had a lower tip-sample barrier showed an SCLC type behaviour while the sample with a higher tip-sample barrier showed a Poole-Frenkel type behaviour. Thus the KPFM measurements seem to indicate that if the barrier between tip and sample is sufficiently low, the current indeed is space charge limited. However, as soon as the barrier is higher than a certain threshold the current can be described by a Poole Frenkel type model.

4.1.4 The effect of PEDOT:PSS on the local conduction

Finally the effect of the underlying layer was studied, the results are shown in figure 4.10. When looking at the transition of ITO to glass it is clear that when the glass is covered with PEDOT:PSS that the surface potential difference does not change, while without the PEDOT:PSS there is a visible shift in surface potential exactly at the edge of the ITO.^[29] This clearly shows that the barrier between tip and sample will change when using C-AFM on samples without PEDOT:PSS. Moreover, without PEDOT:PSS as an intermediary layer between the ITO and the P3HT or P3HT:PCBM blends an ohmic contact is no longer ensured.

CHAPTER 4. RESULTS AND DISCUSSION

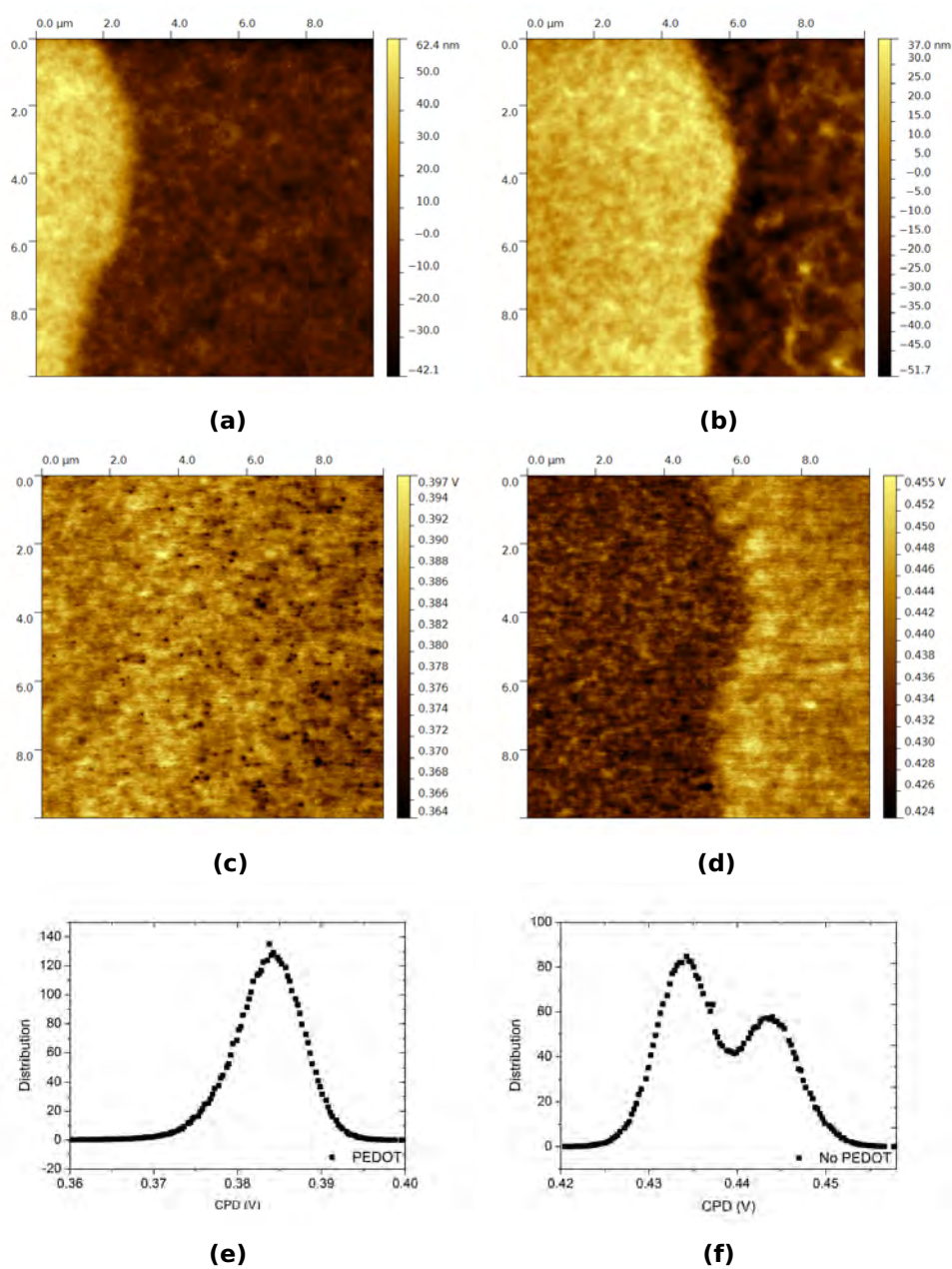


Figure 4.10: Direct comparison of the topographic, KPFM signal ($10 \times 10 \mu\text{m}^2$) and contact potential distribution of a P3HT layer deposited on PEDOT:PSS on ITO (a,c,e) and P3HT deposited on bare ITO (b,d,f).

CHAPTER 4. RESULTS AND DISCUSSION

The sample without the PEDOT:PSS layer shows a clear contrast in the contact potential difference signal, while this contrast cannot be seen on the sample with a PEDOT:PSS layer. Moreover, the observed contrast shows that V_{CPD} between tip and sample is larger on P3HT on glass compared to P3HT on ITO thereby indicating that a possible effect on local conduction can be seen. This effect has been investigated in further detail by analysing IV curves made at different distances from the contact on samples with and without PEDOT:PSS. It is expected that the samples with PEDOT:PSS show a uniform behaviour while those without PEDOT:PSS show differences in local conduction as transport will be either in plane or out of plane depending on the measurement configuration.

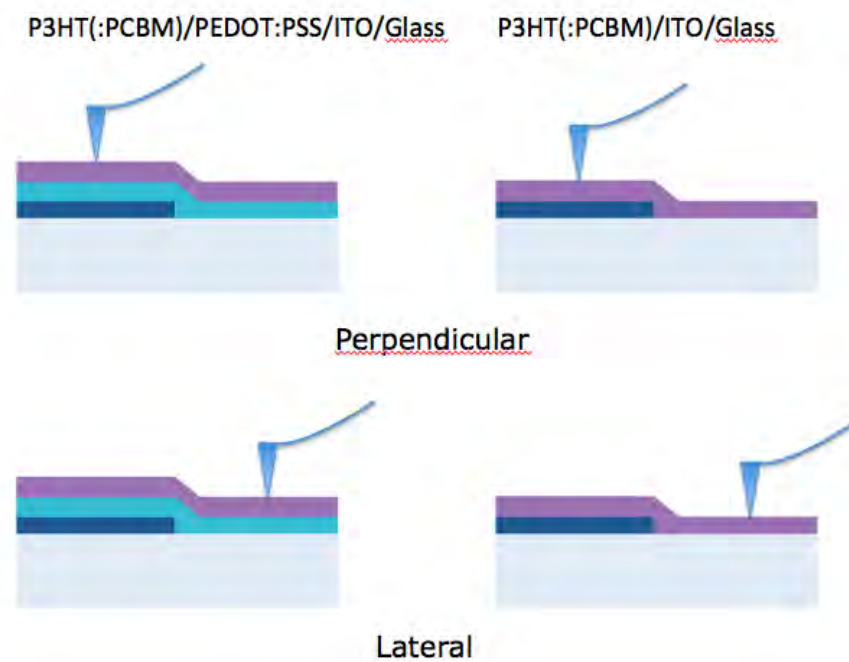


Figure 4.11: An overview of the measurement configuration for the lateral and perpendicular case, with and without PEDOT:PSS.

A direct comparison between the IV-curves plotted according to space charge limited current and Poole Frenkel (Fig. 4.12) shows that in the case

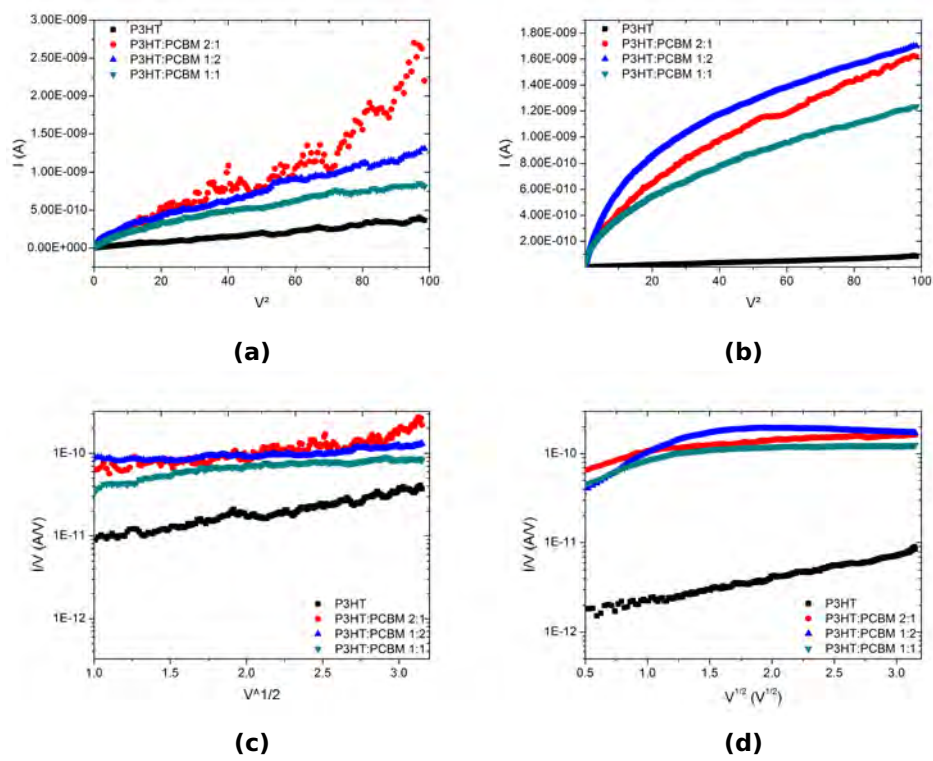


Figure 4.12: Direct comparison of SCLC type (a,b) and Poole Frenkel type (c,d) plots for perpendicular (a,c) and lateral transport (b,d).

CHAPTER 4. RESULTS AND DISCUSSION

of perpendicular transport the conduction can be adequately described by either Poole-Frenkel or SCLC depending on the tip-sample barrier as suggested above. However, in the perpendicular case neither of the two models corresponds to the measured IV curves. The IV-curves measured in the lateral configuration and plotted according to the Poole-Frenkel model even suggest a negative slope, this however, seems to be physically impossible. Moreover, none of the injection/transport models discussed above seem to be able to describe the nature of the transport in the lateral case. Furthermore, it is well known that transport in P3HT heavily depends on the stacking of the individual units thereby explaining as to why this difference exists.^[9]

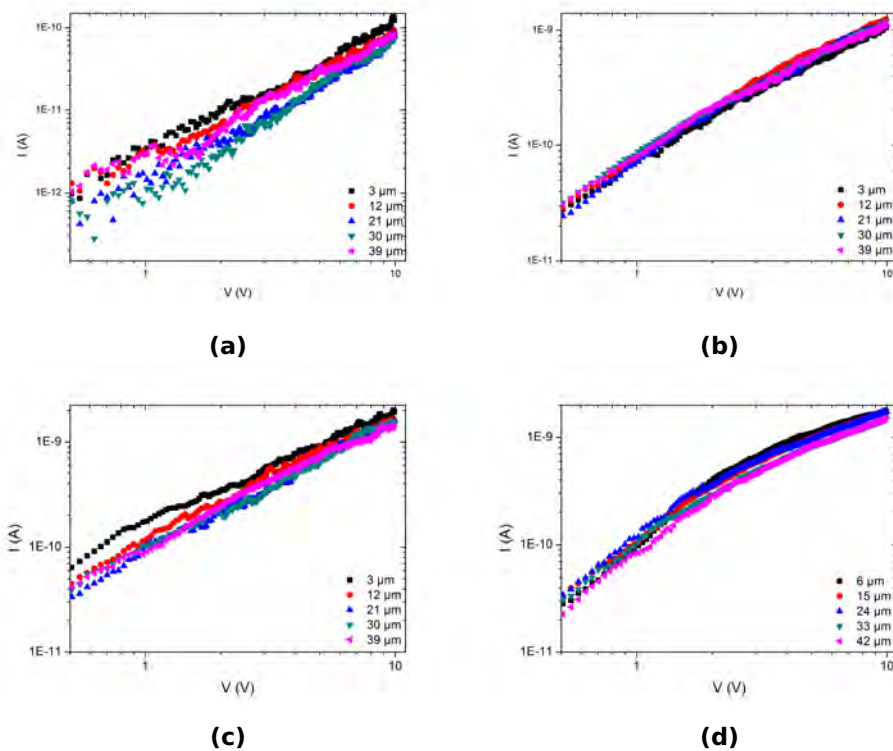


Figure 4.13: An overview of JV curves at different distances from the contact. (a) Shows the pure P3HT sample, (b) shows the P3HT:PCBM 1:1, (c) contains IV curves of the P3HT:PCBM 2:1 sample and (d) shows the P3HT:PCBM 1:2 ratio.

CHAPTER 4. RESULTS AND DISCUSSION

It has been shown by Moerman in the past that the current as measured by conductive AFM remains constant irrespective of the distance between the AFM tip and the back electrode with a study of fibrillar P3HT.^[58] A similar behaviour is found here for thin films of P3HT and P3HT:PCBM mixtures suggesting that the current is mainly contact limited. More specifically, the shape of the curve measured perpendicular is different than those measured in the lateral configuration indicating a different mechanism between the two configurations.

A similar study of P3HT:PCBM on PEDOT:PSS is possible, however, these results are even more difficult to interpret as the injected charges can be transported either through the P3HT:PCBM blend or through the PEDOT:PSS. The current measured at different distances does not seem to vary, which is similar to the non-PEDOT:PSS case.

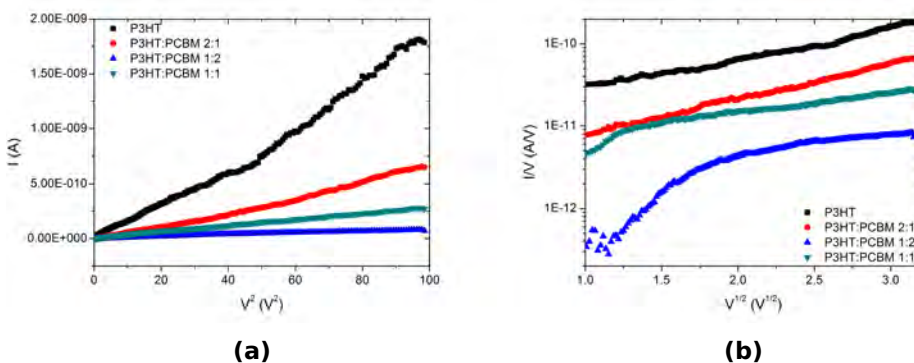


Figure 4.14: The current measured in a lateral configuration away from the ITO contact in an SCLC type plot (a) and a Poole Frenkel type plot (b)

The plots as shown in figure 4.14 again show that either a space charge limited or Poole-Frenkel type current can be found. These local IV curves were taken at a distance of 40 μm from the ITO back contact but with a PEDOT:PSS interlayer, and now either Poole Frenkel or SCLC does seem to be valid this strongly indicates that PEDOT:PSS is a necessary layer when studying the local charge transport characteristics. This however, is

well known as generally the HOMO level of organic blends not necessarily corresponds to that of ITO.

4.1.5 Conclusions

In conclusion we have shown that the current as measured by AFM is mainly contact limited and can be described by a Poole-Frenkel type injection or SCLC, depending on the tip sample barrier. Moreover, this type of injection does not seem to be limited to a single material type but appears to be applicable for standard P3HT, P3HT:PCBM mixtures and novel material types such as PTB7:PC₇₁BM and DTP based polymers. However, to be able to link the physical properties (such as mobility) of the polymers in question to the measured current voltage curves a more thorough analysis of the interface between AFM tip and polymer is needed. Additionally, the KPFM results on P3HT:PCBM and PCDTBT:PC₇₁BM blends with different ratios indicate that the measured contact potential difference is linked to the HOMO level of the polymer. Moreover, KPFM and C-AFM on P3HT/PEDOT:PSS/ITO and on P3HT/ITO shows that PEDOT:PSS has an influence on the surface potential and that the influence on the local current voltage curves is not negligible.

4.2 Scanning Probe Microscopy for interlayer characterization

4.2.1 Introduction

To render conjugated polymers soluble in more environmentally benign solvents (rather than chlorobenzene etc.), which are highly desirable toward high-throughput OPV solution processing, several synthetic strategies can be adopted. Introduction of ionic moieties as side chains on the polymer backbone affords CPEs, applicable either as active light-harvesting materials or as interlayer materials in the solar cell stack. Ongoing synthetic efforts have been directed toward the preparation of a wide range of cationic polythiophene (co)polymers with appended ‘ionic liquid-like’ N-methylimidazole moieties through substitution on the bromohexyl-substituted precursor polymers and considerably facilitated by employing microwave heating.^[10,27,44] The versatility of the Grignard metathesis (GRIM) polymerization route^[37,52,95] allows straightforward tuning of the molecular weight, the built-in monomer ratio, the side chain pattern and the polymer architecture (random versus block copolymers), combined with narrow polydispersities and high regioregularities, while the counter ion can be readily exchanged on the final polymer stage.^[27]

4.2.2 Imidazolium-substituted polythiophenes as efficient electron transport materials

For this interlayer work, one particular ionic imidazolium-functionalized polythiophene homopolymer (with Br⁻ counter ion) was initially selected. Two batches with varying molecular weight (P2 and P3, with $M_n = 11.2$ kDa and 32.6 kDa, respectively, for the non-ionic precursor polymers) and narrow polydispersity ($D = 1.6$) were prepared. These materials were first evaluated as interlayer materials on top of an active layer comprising of PCDTBT, one of the current state-of-the-art low bandgap donor poly-

CHAPTER 4. RESULTS AND DISCUSSION

mers,^[7,8,37,67] and PC₇₁BM (Figure 4.15). The PCDTBT:PC₇₁BM combination combines high efficiency and long operating lifetimes. To enable comparison with the electron transporting layer (ETL) material introduced by Bazan et al.,^[74] trimethylamine-functionalized polythiophene P1^[86] was prepared as well (M_n = 32.6 kDa) as a reference material (Figure 4.15).

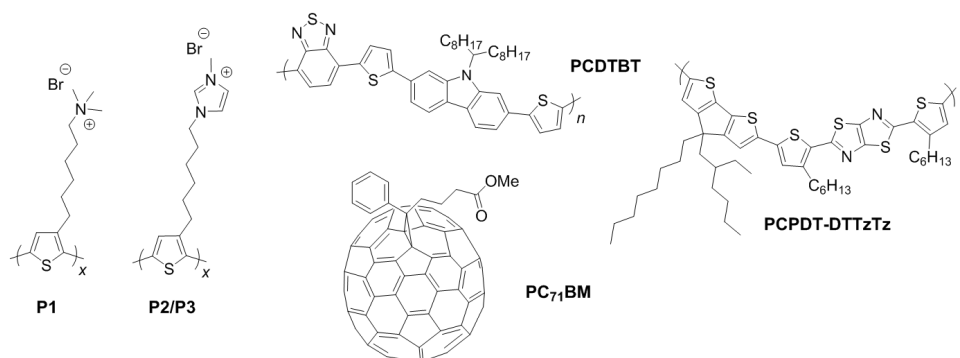
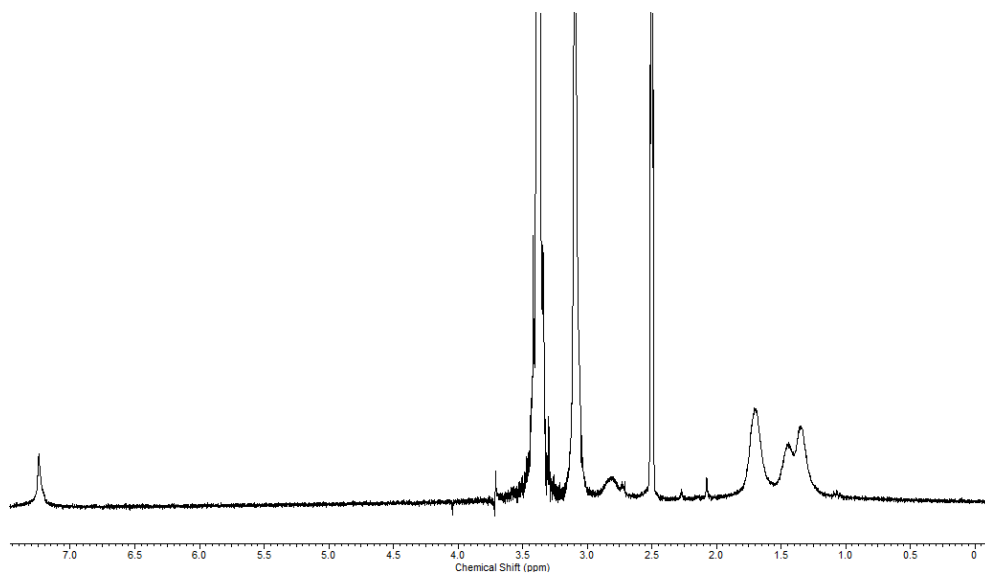


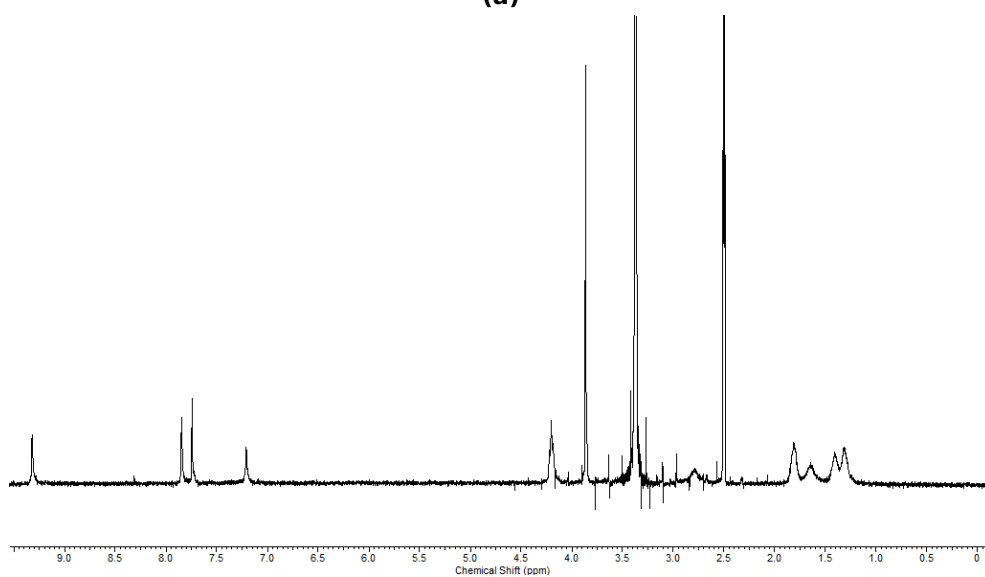
Figure 4.15: Trimethylamine-functionalized polythiophene **P1**, imidazole-functionalized polythiophenes **P2** and **P3**, the PCDTBT and PCPDT-DTTzTz donor polymers, and PC₇₁BM.

Additionally, poly[(9,9-bis(3'-(N,N-dimethylamino)propyl)-2,7-fluorene)--alt-2,7-(9,9-dioctylfluorene)] (PFN) was also included as an additional ETL material in the device set. For ionic polythiophenes P1-P3, complete functionalization and material purity were confirmed by ¹H NMR (Figure 4.16).^[27] The optical absorption spectra show typical polythiophene features, with a small red shift (in film) for P2 and P3 ($\lambda_{\text{max}} = 504$ nm) compared to P1 ($\lambda_{\text{max}} = 482$ nm) (Table 4.6). 'P3HT-like' electrochemical behavior was observed for all three materials by cyclic voltammetry (Table 4.6), the main difference being located at the reduction onset. The presence of the ionic groups in these hydrophilic polymers makes them soluble in alcohols, hence enabling processing from more benign non-chlorinated solvents. Moreover, as orthogonal solvents are applied for the photoactive layer and CPE film, integrity problems due to redissolution of the underlying BHJ layer are readily avoided.

CHAPTER 4. RESULTS AND DISCUSSION



(a)



(b)

Figure 4.16: ¹H NMR spectra of ionic polythiophenes **P1** (top) and **P3** (bottom).

CHAPTER 4. RESULTS AND DISCUSSION

Table 4.6: Cyclic voltammetry and UV-vis data (both in film) of the **P1-P3** ionic polythiophenes (and P3HT/PCDTBT under the same conditions).

Polymer	λ_{max} [nm]	E_{onset}^{ox} [V]	E_{onset}^{red} [V]	HOMO [eV]	LUMO [eV]	E_g^{EC} [eV]	E_g^{OP} [eV]
P1	482	0.34	-1.98	-5.20	-2.88 (-3.19)	2.32	2.01
P2	504	0.33	-1.91	-5.19	-2.95 (-3.25)	2.24	1.94
P3	504	0.10	-1.93	-4.96	-2.93 (-3.00)	2.03	1.96
P3HT	519	0.27	-2.24	-5.13	-2.62 (-3.23)	2.51	1.90
PCDTBT	579	0.47	-1.63	-5.43	-3.33 (-3.57)	2.10	1.86

^a In film (P1-P3 from tetrafluoropropanol, P3HT from chlorobenzene, PCDTBT from chlorobenzene/dichlorobenzene 70/30)

^b Based on the onset of reduction ^c Values between brackets are based on: LUMO = HOMO + E_g^{OP} ^d $M_n = 2.5 \times 10^4$ g/mol, $D = 2.1$.

For the evaluation of the ETL features of the novel ionic polythiophenes, the standard solar cell stack glass/ITO/PEDOT-PSS/polymer:PC₇₁BM/CPE/Al was employed.^[74] In a first experiment, the optimal concentration of the CPE materials (in methanol) was investigated for PCDTBT:PC₇₁BM active layers (data not shown). The optimum was found around 0.02 w/v% and hence all further experiments were performed using this concentration.^[74] Next, the devices with interfacial charged polymer layers were compared to cells with traditional Ca/Al electrodes (Table 4.7). Ca is commonly applied as a low work function metal to optimize electrical contact but suffers from high air-sensitivity and is therefore increasingly replaced by solution-processed metal oxides (ZnO, TiO_x). The overall increase in PCE due to the ETL materials could mainly be attributed to an increase in short-circuit current density (J_{sc}), with only minor contributions from open-circuit voltage (V_{oc}) and fill factor (FF) (Figure 4.17, Table 4.7).

Comparing the three interlayer materials, the novel high-Mn ionic polythiophene P3 afforded the best results, with a top PCE of 6.7% (average 6.2%). Compared to the reference ETL material P1, derived from the same precursor polymer batch, there is an increase in PCE of 0.2% (both for the best and average PCE). In comparison with the device utilizing Ca,

CHAPTER 4. RESULTS AND DISCUSSION

J_{sc} increased from 10.7 mA/cm² to 12.1 mA/cm², which is an increase of roughly 20%. The increase in J_{sc} was confirmed by extracting the currents from external quantum efficiency (EQE) measurements (Figure 4.18, Table S2). The enhanced current can partly be explained by increased reflection upon removing the Ca layer (which shows some ‘parasitic’ absorption; Figure 4.19).^[31] The addition of the CPE layers seems to provide an optimal balance between improved ohmic contact and mirror effects.

Table 4.7: Photovoltaic performance of PCDTBT-based BHJ solar cell devices with and without the addition of CPE layers. ^a Averaged over 4 devices.

Layer Sequence	V_{oc} [V]	J_{sc} [mA cm ⁻²] ^b	FF	Average η [%]	Best η [%]
.../PCDTBT:PC ₇₁ BM/Al	0.73	11.36	0.41	3.39 ± 0.36	3.82
.../PCDTBT:PC ₇₁ BM/Ca/Al	0.87	10.66	0.57	5.23 ± 0.33	5.71
.../PCDTBT:PC ₇₁ BM/ P1 /Al	0.88	11.82	0.58	6.03 ± 0.46	6.48
.../PCDTBT:PC ₇₁ BM/ P2 /Al	0.84	11.67	0.55	5.32 ± 0.24	5.57
.../PCDTBT:PC ₇₁ BM/ P3 /Al	0.87	12.05	0.59	6.22 ± 0.43	6.69
.../PCDTBT:PC ₇₁ BM/PFN/Al	0.88	11.84	0.58	5.96 ± 0.42	6.33
.../PCDTBT:PC ₇₁ BM/MeOH/Al	0.88	11.68	0.57	5.81 ± 0.17	5.99

^a Stack: glass/ITO/PEDOT-PSS/PCPDT-DTTzTz:PC₇₁BM/X/Al with X = Ca or CPE.

^b Uncorrected data.

Table 4.8: Photovoltaic performance of PCPDT-DTTzTz-based BHJ solar cell devices with and without the addition of CPE layers. ^a

Layer Sequence	V_{oc} [V]	J_{sc} [mA cm ⁻²] ^b	FF	Average η [%]	Best η [%]
.../PCPDT-DTTzTz:PC ₇₁ BM/Ca/Al	0.68	12.2	0.54	4.50 ± 0.20	4.78
.../PCPDT-DTTzTz:PC ₇₁ BM/ P3 /Al	0.68	12.9	0.55	4.86 ± 0.40	5.43

^a Stack: glass/ITO/PEDOT-PSS/PCPDT-DTTzTz:PC₇₁BM/X/Al with X = Ca or CPE.

^b Uncorrected data.

Table 4.9: Photovoltaic performance of PCDTBT-based BHJ solar cell devices with and without the addition of CPE layers, as applied for the EQE measurements.

Layer Sequence	V_{oc} [V]	J_{sc} [mA cm ⁻²] ^b	FF	Best η [%]	J_{EQE} [%]
.../PCDTBT:PC ₇₁ BM/Ca/Al	0.81	9.26	0.62	4.66	9.05
.../PCDTBT:PC ₇₁ BM/ P1 /Al	0.87	10.2	0.65	5.79	10.6
.../PCDTBT:PC ₇₁ BM/ P3 /Al	0.85	10.4	0.67	5.90	10.7

^a Stack: glass/ITO/PEDOT-PSS/PCDTBT:PC₇₁BM/X/Al with X = Ca or CPE.

^b Uncorrected data.

Utilizing the same ionic polythiophene material with a lower Mn (P2) resulted in a clearly lower performance, indicating that the efficiency of

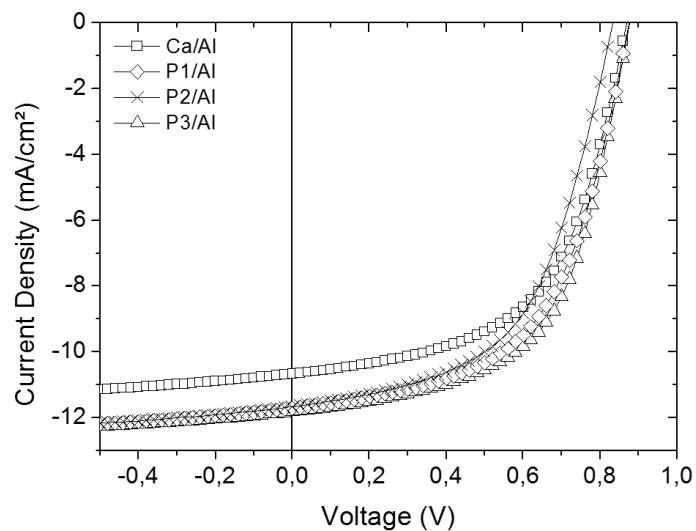


Figure 4.17: *J-V* curves under illumination of PCDTBT-based BHJ photovoltaic devices with and without additional CPE layers.

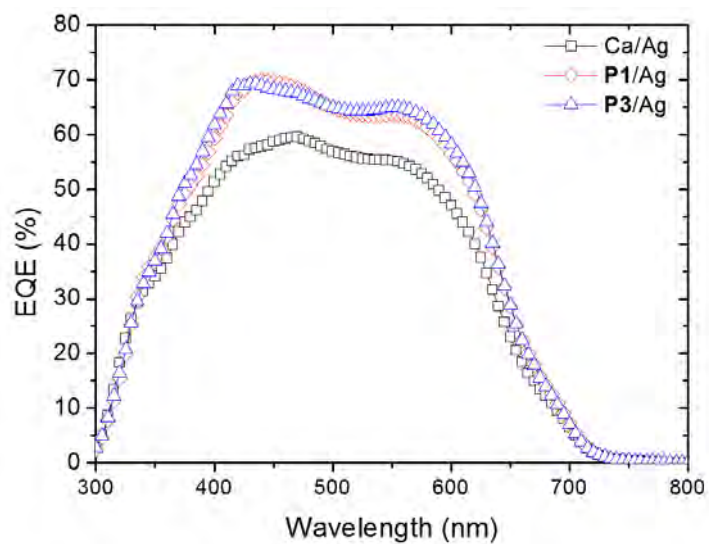


Figure 4.18: EQE spectra for devices containing the P1 and P3 CPEs (compared to a reference Ca/Ag device)

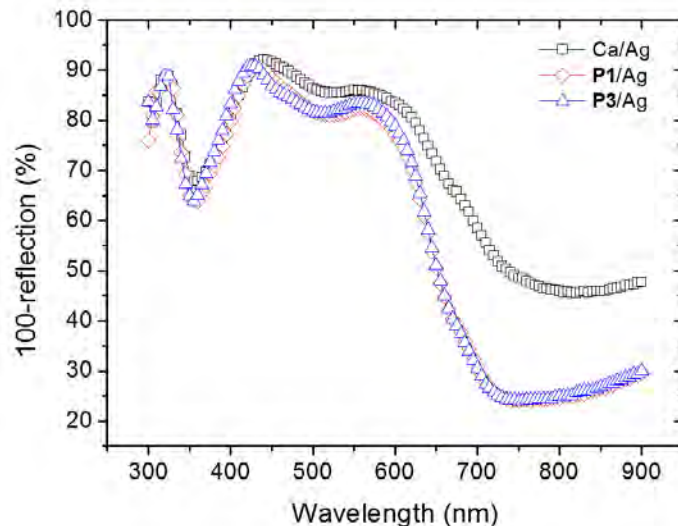


Figure 4.19: Reflectivity spectra for devices containing the **P1** and **P3** CPEs (compared to a reference Ca/Ag device)

the interlayer is dependent on the molecular weight of the interfacial polymer. Ionic polythiophene P3 also showed a noticeable improvement when compared with the widely used PFN interlayer material (on average 5.96% vs. 6.22%). Finally, a reference device for which pure methanol was spin-coated on top of the active layer was produced (Table 4.7, indicated as .../MeOH/Al, Figure 4.20) to investigate whether the beneficial factor leading to improved device performance could not be reproduced by the solvent only. From the data in Table 1 we can observe a noticeable improvement with respect to the reference device utilizing the traditional Ca/Al electrode. This observation has been made before, leading to the statement that the methanol treatment results in the formation of an interface dipole between the active layer and the metal layer.^[14,16,23,35,69,74,85,92–94] The incorporation of the CPE layers did, however, result in further improvements in J_{sc} , resulting in higher overall PCEs. This suggests that, on top of the formation of an interface dipole, the presence of the CPE layer leads to additional beneficial factors improving charge extraction.

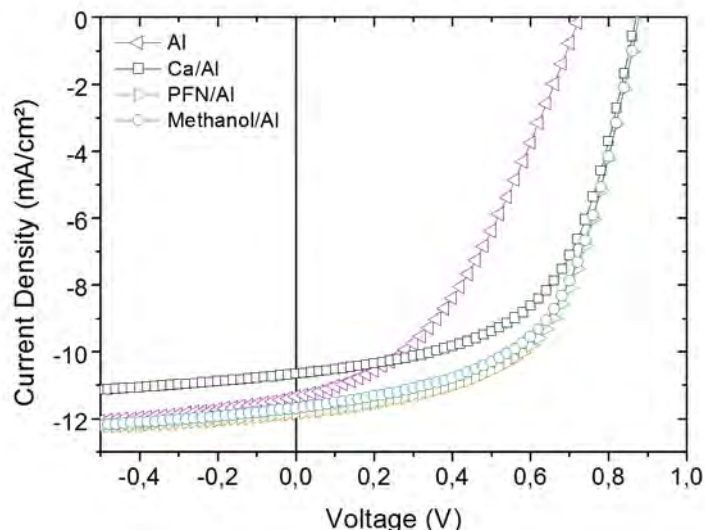


Figure 4.20: J-V curves under illumination of PCDTBT:PC₇₁BM BHJ photovoltaic devices with and without additional CPE layers.

In a follow-up experiment, the highest performing ETL material P3 was also tested on top of an active layer comprising of a different low bandgap polymer, i.e. (poly([4-(2'-ethylhexyl)-4-octyl-4H-cyclopenta[2,1-b:3,4-b']-dithiophene-2,6-diyl]-alt-[2,5-di(3'-hexylthiophen-2'-yl)thiazolo[5,4-d]-thiazole-5',5''-diyl])) (PCPDT-DTTzTz).^[27] As can clearly be seen from the data in Table 4.8 (and the J-V curves in Figure 4.21), the results confirmed the beneficial effect of the novel CPE layer, with an increase in J_{SC} and FF leading to a similar overall PCE improvement. It has to be noted here that the efficiency obtained for the reference device (4.78% best, 4.50% average) is the highest PCE reported for this donor polymer (4.03% before).

To get a more clear view on the potential loss mechanisms in the devices, dark J-V curves were measured, revealing information on the series and shunt resistances (R_s and R_{sh}). Figure 4.22 shows the dark curves for the best performing CPE material P3 and for the reference devices with solely Al and Ca/Al as top electrodes. Utilizing P3 as a CPE resulted in a strong increase of R_{sh} in comparison to the two reference devices. As for

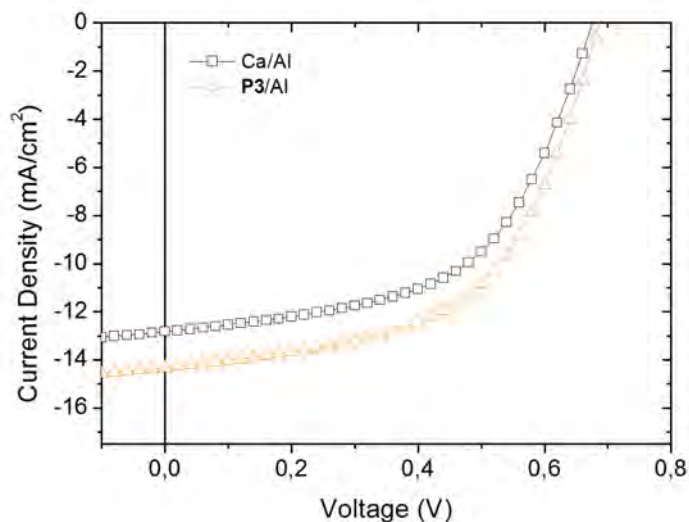


Figure 4.21: J-V curves under illumination of PCPDT-DTTzTz:PC₇₁BM BHJ photovoltaic devices with and without additional CPE layers.

R_s , there was a slight improvement when comparing the CPE-containing device with the Ca/Al reference. However, compared with the Al reference, R_s was much lower. Moreover, in the negative half of the x-axis, the photovoltaic device with a P3 ETL layer showed much less leakage current, confirming the positive influence of the interlayer on the performance of the solar cell device.

Atomic force microscopy (AFM) measurements were performed to investigate the interlayers when deposited on top of the PCDTBT:PC₇₁BM active layer (Figure 4.23). The roughness in all cases increased compared to non-covered PCDTBT:PC₇₁BM films. The ETL materials P1-P3 did not completely cover the active layer surface. The calculated surface coverage seemed to be similar for all ETLs (55%), but the observed morphology was noticeably different. Figure 4.23(a-c) shows the topography, whereas Figure 4.23(d-f) reveals the adhesion images, reflecting the ‘sticking’ of the AFM tip to the surface (additional images can be found in Figure 4.24 and 4.25). The topography images (a-c) show the presence of rather large

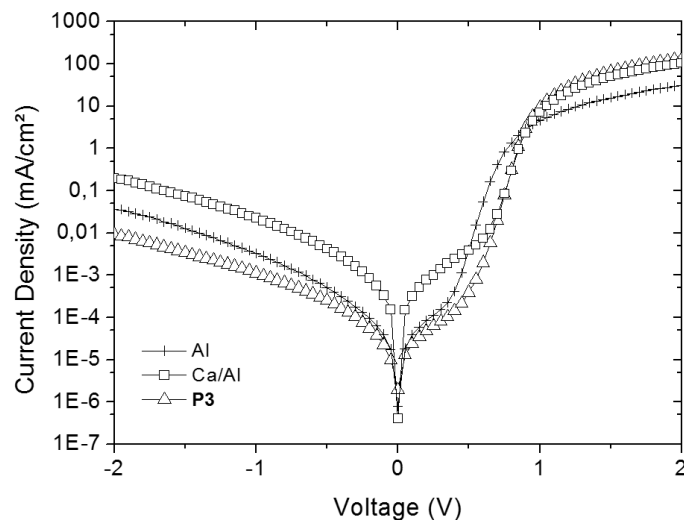


Figure 4.22: J-V curves of PCDTBT-based BHJ photovoltaic devices under dark conditions with and without additional CPE layers.

'holes' (average diameter 110 nm) for P1, whereas for P3 a much finer and more random network is formed. From the adhesion images (d-f) it can be seen that the regions with low adhesion (dark spots) correspond with the higher topography features, and the regions with high adhesion (bright spots) correspond with the lower features on the height image. From these observations, it looks like the active layer is not completely covered and is directly exposed by the presence of holes in the ETL material. The density of these holes can possibly be correlated to the final device performance.

4.2.3 Thickness effect

The study as presented above did not include any further research on whether or not the electrical properties improved with increasing ETL thickness. A study with varying ETL concentration was done, the JV-characteristics (fig. 4.26) clearly show that with higher concentrations in solution the short circuit current decreases. At concentrations of 1 and 2 mg/mL the series resistance increases massively with a resulting drop in efficiency.

CHAPTER 4. RESULTS AND DISCUSSION

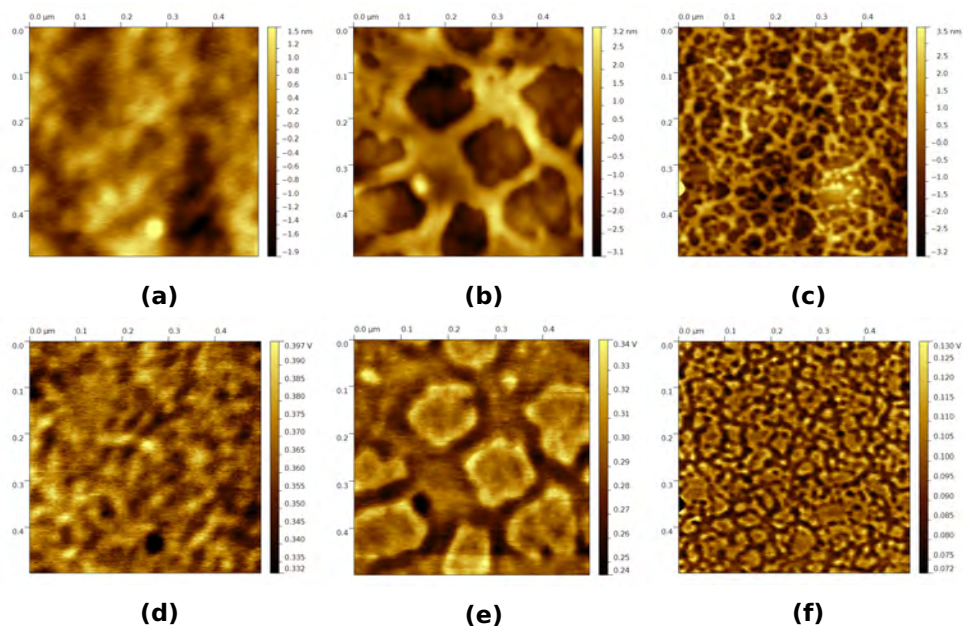


Figure 4.23: AFM (a,b,c: topography; d,e,f: adhesion) images ($500 \times 500 \text{ nm}^2$) of layer stacks with and without additional CPE materials: a,d) PCDTBT:PC₇₁BM, b,e) PCDTBT:PC₇₁BM/**P1**, c,f) PCDTBT:PC₇₁BM/**P3**.

Figure 4.27 shows the morphology (a-c) and adhesion images (d-f) as obtained from atomic force microscopy. At the lowest concentration of 0.25 mg/mL a clear contrast in the adhesion signal is visible, indicating that the ETL does not cover the complete surface. The concentration of 0.5 mg/mL only shows a few distinct areas on the adhesion signal, indicating an improved coverage for the ETL. Thereby confirming the notion that increasing the concentration improves the coverage. While 0.50 mg/mL isn't sufficient to completely cover the surface it is however, sufficient to act as a barrier for electron extraction. Increasing the concentration even further did increase the coverage to a point where the complete surface was coated with the ETL however, the JV-characteristics already show that cells with such thick interlayers do not behave thereby showing that a trade-off exists between coverage and increasing the short circuit current.

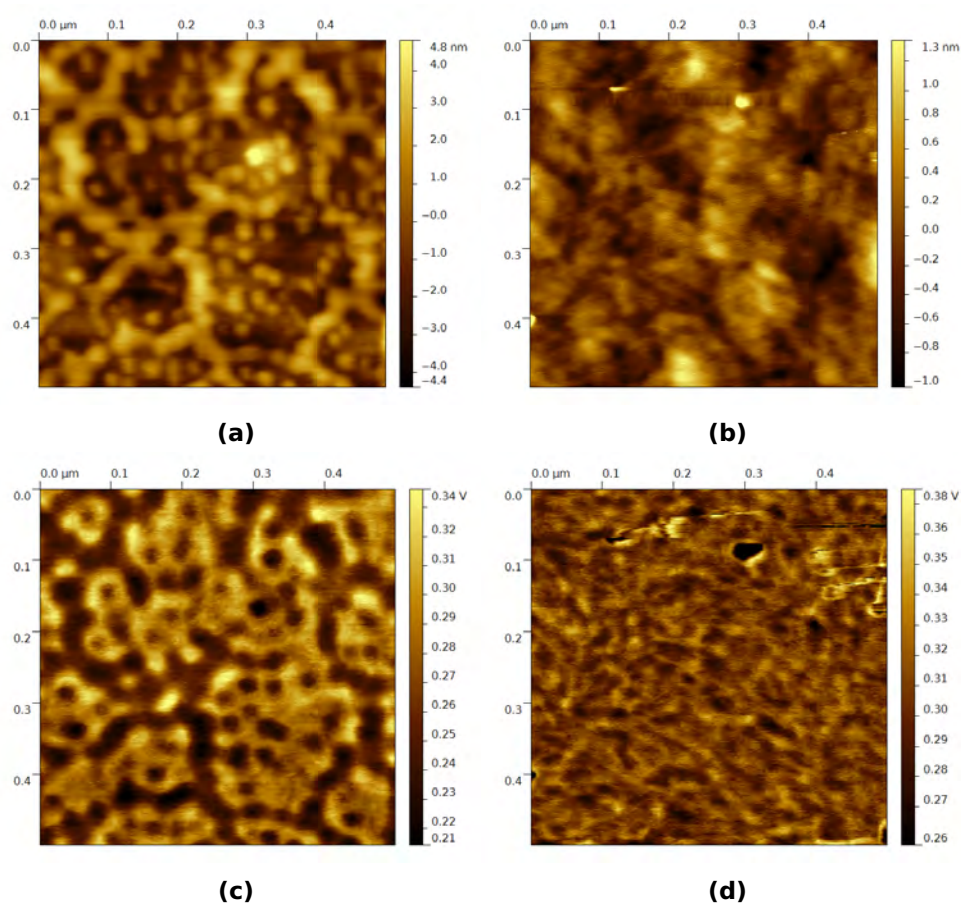


Figure 4.24: AFM (a,b: topography; c,d: adhesion) images (500x500 nm²) of layer stacks with and without additional CPE layer: a,c) PCDTBT:PC₇₁BM/P₂, b,d) PCDTBT:PC₇₁BM/MeOH.

CHAPTER 4. RESULTS AND DISCUSSION

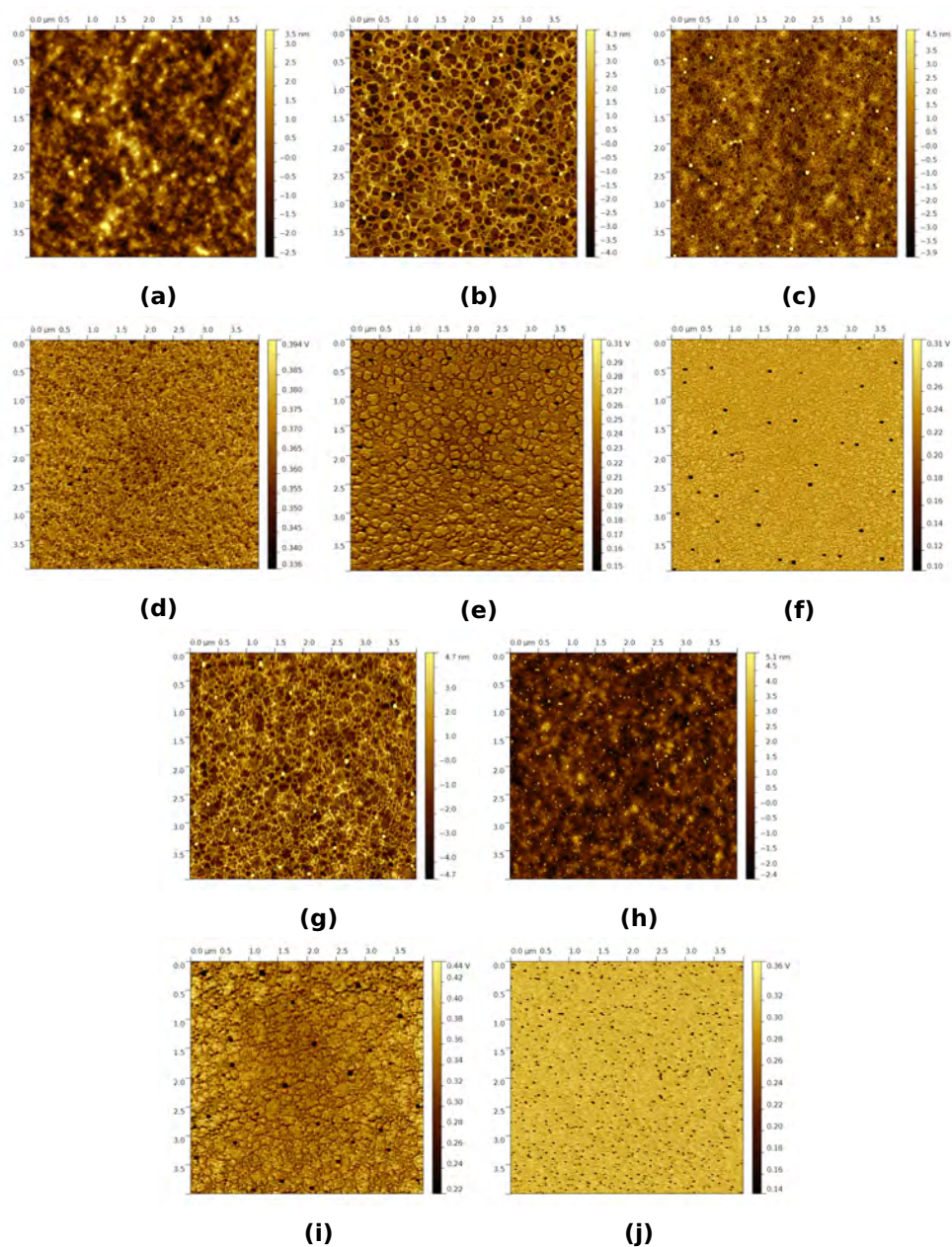


Figure 4.25: AFM (a-c, g-h: topography; d-f, i-j: adhesion) images ($4 \times 4 \mu\text{m}^2$) of layer stacks with and without additional CPE layers: a,d) PCDTBT:PC₇₁BM; b,e) PCDTBT:PC₇₁BM/**P1**; c,f) PCDTBT:PC₇₁BM/**P2**; g,i) PCDTBT:PC₇₁BM/**P3**; h,j) PCDTBT:PC₇₁BM/MeOH.

CHAPTER 4. RESULTS AND DISCUSSION

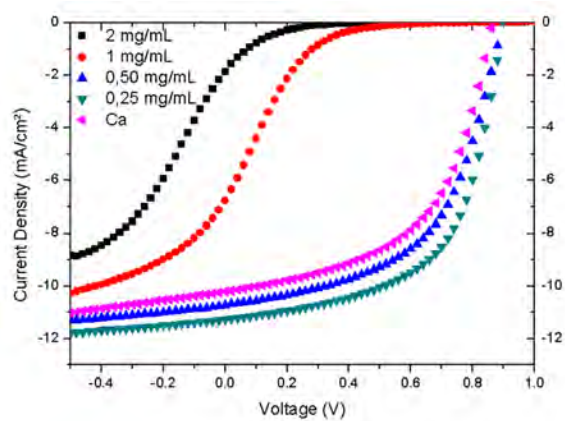


Figure 4.26: Current-voltage characteristics of devices with varying ETL thickness.

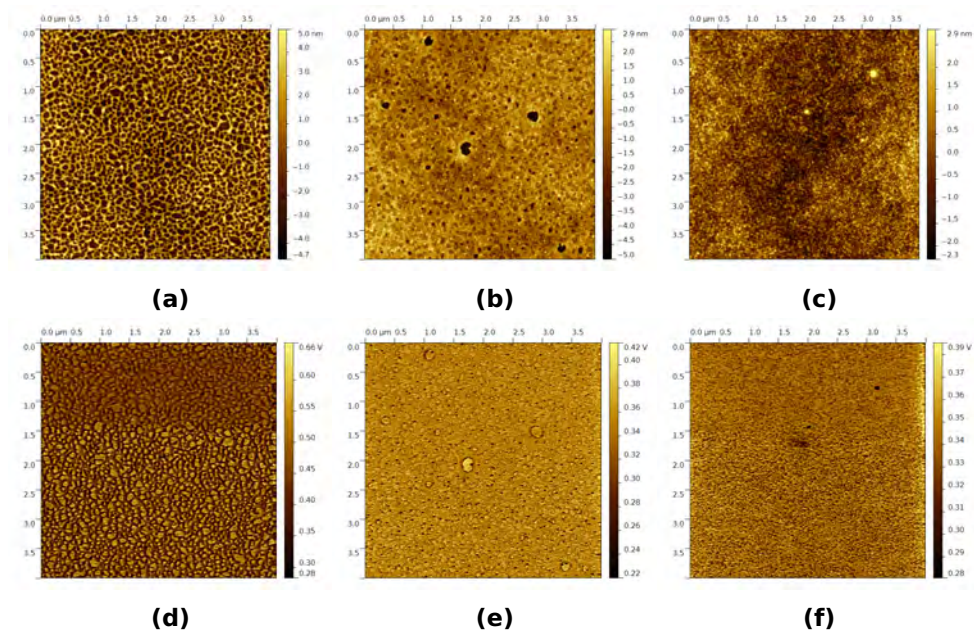


Figure 4.27: Topography (a-c) and adhesion images (d-f) ($4 \times 4 \mu\text{m}^2$) of PCDTBT:PC₇₁BM coated with CPE layers from 0.5 (a,d), 1 (b,e) and 2 mg/mL (c,f)

4.2.4 Morphology and mechanical properties

The following section will go into deeper detail on the morphological, electric and electronic properties of the best performing ETL.

PeakForce quantitative nanomechanical property mapping (PF-QNM) probes the morphology and the mechanical properties at the same time, by making a force distance curve at each point and fitting this force distance curve with the Derjaguin-Muller-Toporov (DMT) model of elastic contact.^[61] Depending on the types of materials under investigation, a suited AFM probe needs to be selected. With a fully calibrated tip it is possible to gain insight on the absolute values of the local mechanical properties (e.g. Young's modulus, adhesion, deformation depth). If absolute values are not of importance, a single uncalibrated cantilever is sufficient. This still allows a study of the coverage or the intermixing of certain materials.^[12] In this case, PeakForce QNM was used to study surface coverage and therefore relative differences are sufficient to draw conclusions.

When looking at the film morphologies (Fig. 4.28 (a), (b) and (c)) it is clear that the calculated RMS roughness (0.6 nm, Table 4.10) is similar for both the reference and methanol treated samples. The biggest change in morphology was visible when the CPE was added. However, from the morphology images it is not clear if the additional CPE layer completely covers the surface or if the lower lying regions actually reveal the underlying active layer.

Table 4.10: Values for the roughness, image averaged contact current and contact potential difference determined from respectively, topography, contact current and contact potential images.

Sample	RMS Roughness	Contact current	Contact potential difference
Reference	0.67 nm	-1.31 pA	-0.30 V
MeOH	0.62 nm	-2.22 pA	-0.26 V
CPE	2.64 nm	-9.47 pA	-0.10 V

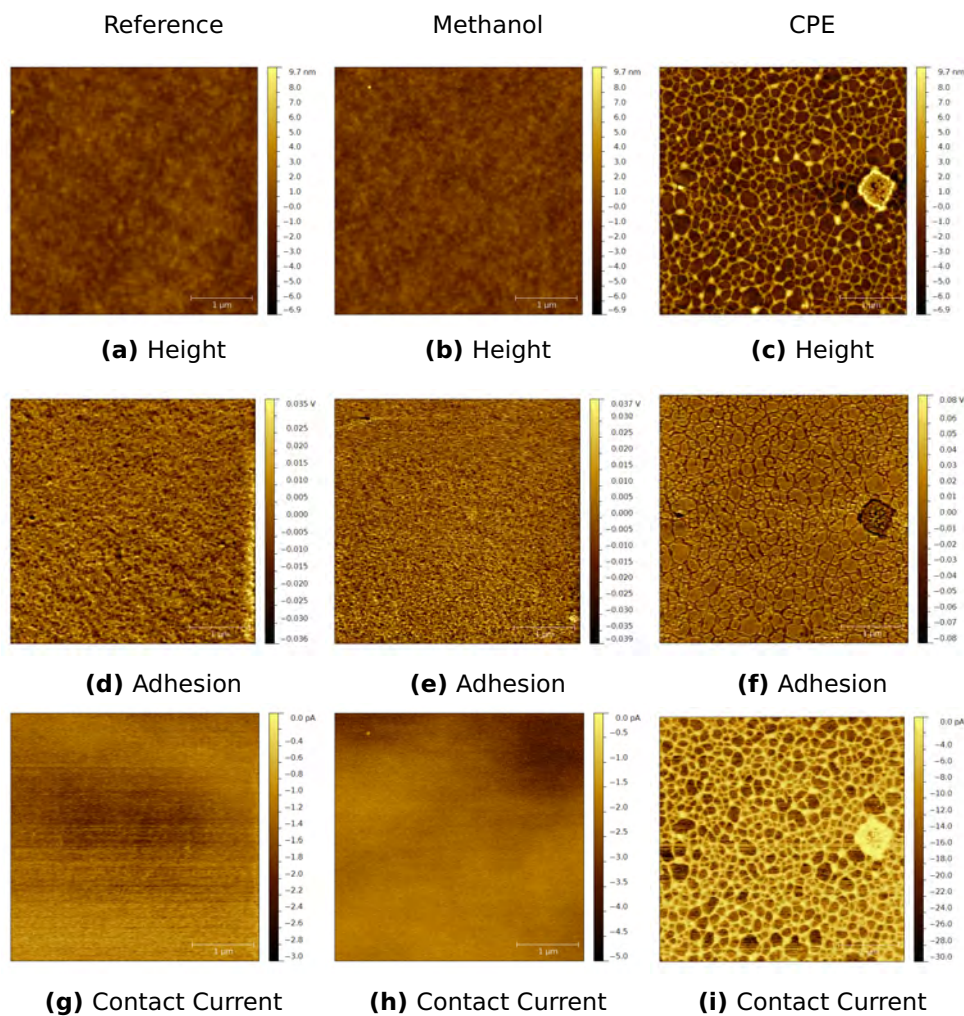


Figure 4.28: Overview of the morphology, adhesion and local current for the different samples, as analysed by PeakForce QNM and TUNA on a $4 \times 4 \mu\text{m}^2$ scale. Images (a), (b) and (c) show the morphology of the reference, methanol treated and CPE covered sample, respectively; (d), (e) and (f) show the adhesion for the reference, methanol treated and CPE covered sample, respectively; (g), (h) and (i) show the cycle averaged local currents for the reference, methanol treated and CPE covered sample, respectively. The image averaged currents are displayed in table 4.10.

In this manuscript the adhesion is presented, the adhesion represents how much your tip interacts with the surface. As interaction forces are different for different materials this will also result in different adhesion properties. Figures 4.28 (d), (e) and (f) show that there are clearly two distinct regions for the CPE treated sample compared to the reference and methanol treated samples. Moreover, a nice correlation between topography and adhesion exists for the CPE coated sample, thus it is possible to conclude that the CPE forms a web on top of the bulk heterojunction. The coverage is about 43 %, as calculated by bearing analysis from 1 by 1 μm^2 and 4 by 4 μm^2 images.

The average thickness of the CPE layer was calculated by analysis of the thickness histogram of figure 4.28 (c). Fitting the two peaks with a normal distribution and calculating the difference between the centers of the two peaks gives the average thickness of the CPE layer. This results in an average thickness of about 3.56 nm. At these thicknesses, the effect of tunneling can be excluded, as this phenomenon only has a major contribution to the current for layers thinner than 0.5 nm.^[30]

4.2.5 PeakForce TUNA and Conductive AFM

While tunneling can be excluded as a possible mechanism, the local current is still of major importance. As the CPE layer is very thin, traditional conductive AFM might result in destruction of the interlayer. PeakForce TUNA is similar to PeakForce QNM with one major difference: PFTUNA tips have a conductive coating which means that when the tip is in contact with the sample it is possible to measure the current while applying a certain bias. Due to the nature of this technique, the applied contact force is constant over the entire image regardless of the applied DC bias. Moreover, the applied force is perpendicular to the sample while conductive AFM has a resulting force parallel with the sample. Thus using PeakForce TUNA should ensure the least amount of sample damage. Nevertheless,

conductive AFM images at both a negative and positive sample bias are included for completion. From PeakForce TUNA measurements three different currents are deduced, namely peak, contact and total current. The peak current is the current at the maximum amount of force during a force distance measurement, the contact current is the current during contact of the tip with the sample and the total current is the time averaged current over the duration of a force distance curve, which also includes the time when the tip is not in contact with the sample.

As the workfunction of the Pt/Ir coated tip is in the same range as the HOMO levels of the probed organic materials the contrast obtained by conductive AFM and PeakForce is due to a hole current.^[18,42] Therefore, when applying a negative bias to the sample holes will be injected from tip into the organic layer. Fig. 4.28 (g), (h) and (i) show the local contact current maps at a DC sample bias of -1.8 V.

In this work the contact current is shown as it lies closest to the classical current measured by conductive AFM. Small differences in hole current between the reference and the MeOH treated sample are visible (Table 4.10 and Fig. 4.28 (g) and (h)) they are however negligible as on this scale the samples will always show some form of inhomogeneity. As evidenced from the KPFM results in table 4.10 there is a small difference in contact potential and thus a small difference in barrier between tip and sample when comparing the reference and MeOH treated samples however, the applied bias of -1.8V should be sufficient to overcome any barrier at the interface between surface and tip. The biggest difference is seen when looking at the CPE treated sample, wherever the CPE is present the hole current seems to be severely limited. The hole blocking nature of this interlayer could explain the increase in short circuit current as seen in^[42] by reducing the interface recombination and thus resulting in more electrons reaching the aluminum top contact.

These results are confirmed by classical conductive AFM measurements clearly showing that at both negative (hole injection) and positive (hole extraction) bias the hole current is severely limited by the conjugated poly-electrolyte interlayer. (Fig. 4.29)

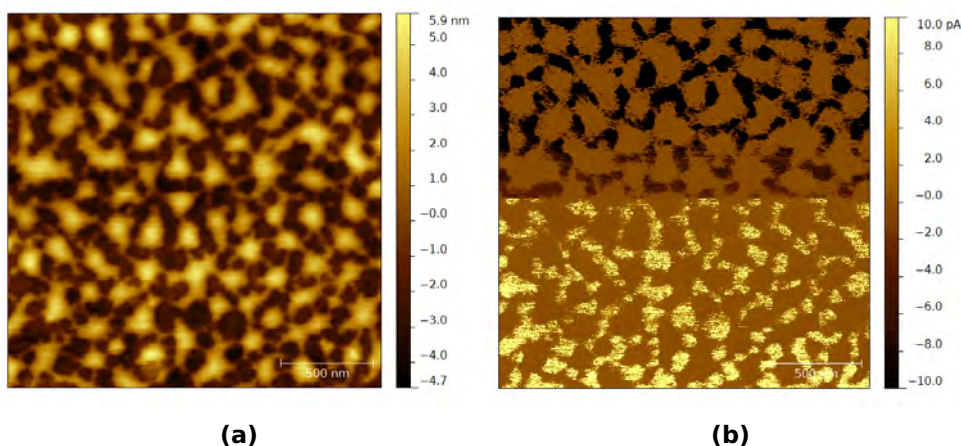


Figure 4.29: Topography (a) and corresponding C-AFM results (b) top part made at a negative sample bias of -1.3 V while the bottom was made at a sample bias of 2.4V

4.2.6 KPFM

In the case of metals, Kelvin Probe Force Microscopy probes the local workfunction, while for blended organic materials one most likely measures a combination of the HOMO levels of the materials present in the bulk heterojunction.^[47]

Fig. 4.30 (d), (e) and (f) show the contact potential difference for the reference, the methanol treated and the CPE coated sample, respectively. A shift of 30 mV is seen (Table 4.10) when going from the reference to the methanol treated sample, an effect also described recently by Zhou et al.^[97] When the CPE is added, a contact potential difference shift of around 0.2 V compared to the reference sample is observed. This difference in surface potential coincides with the estimated difference in HOMO level of

PCDTBT (5.4 eV) and the CPE (5.2 eV).^[42] This change in contact potential difference indicates a lower barrier between the Pt/Ir tip and the sample.

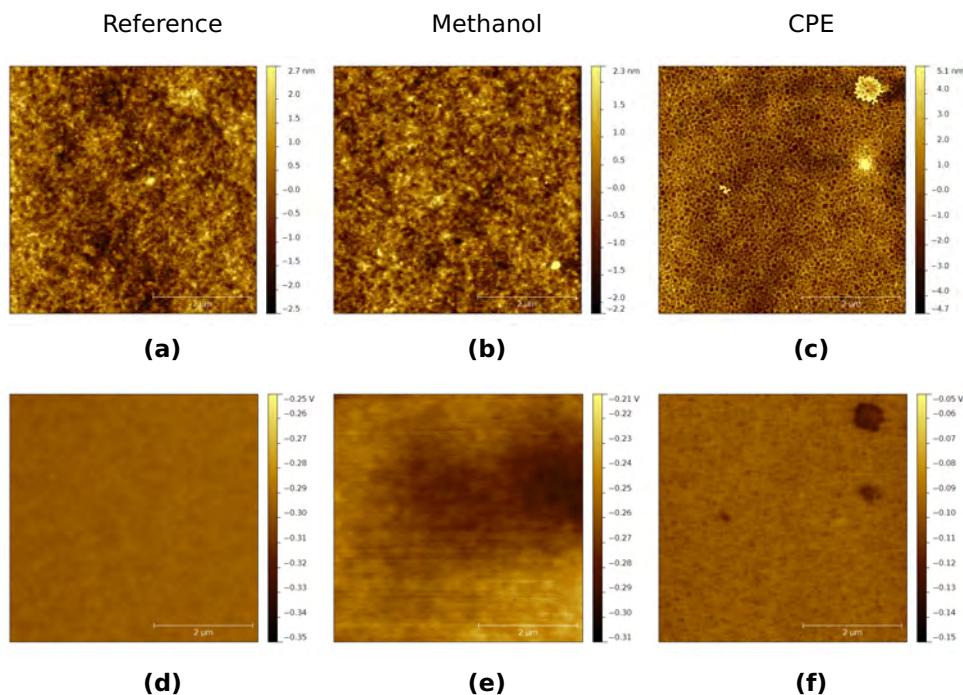


Figure 4.30: Morphology and surface potential images of the reference (a) and (d), the methanol treated (b) and (e) and the CPE covered samples (c) and (f), respectively. ($5 \times 5 \mu\text{m}^2$)

From the analysis of the KPFM image of the CPE coated layer it becomes clear that there are areas with a lower surface potential, which are correlated with the holes that are present in the CPE layer. Topographic artefacts can be excluded as the lateral resolution of KPFM is about 25 nm^[57] and the holes present in the CPE are in the order of 100 nm in diameter. This means that there are areas with a higher and a lower surface potential, indicating the existence of a built-in electric field. From simple electrostatics and a measurement of the CPE layer thickness, this field can be estimated at about 10^6 V/m. Moreover, Hoven et al. have shown that tetrakis(imidazolyl)-borate ions will redistribute when used as a counterion in a PFN based CPE. As the Br⁻ ions used in this work are much smaller they

CHAPTER 4. RESULTS AND DISCUSSION

are most likely mobile and will react to a change in local electrostatic potential and the resulting redistribution of the internal electric field can act as a mechanism to enable efficient electron extraction.^[34]

Further insights into the mechanism at work can be obtained by measuring the change in surface potential upon illumination. Without illumination, the potential difference inside a lower lying region and on top of the CPE layer is around 50 mV, while with illumination, estimated at 0.7 suns, this potential difference is lower, around 20 mV (Fig. 4.31). Two possible explanations can be proposed. At first, one could think that this is merely a screening effect. However, the surface potential difference between the donor-acceptor blend and the CPE layer decreases upon illumination, and this contradicts the idea of a screening effect. A second possibility is charge transfer. A difference in surface potential indicates the existence of regions with a certain amount of positive and negative charges. When the potential difference between the donor-acceptor blend and the CPE is high (in dark), the difference in charges is high. With illumination, both positive and negative charge carriers will be generated inside the active layer. These charges will feel the effect of the built-in potential coming from the CPE layer. Electrons generated in the donor-acceptor blend will move to the CPE, resulting in a decrease of positive charge in the CPE and thus reducing the potential difference, as seen in Fig. 4.32. Moreover, the aluminum top contact acts as an electron extracting contact and the energy barrier between these two materials is most likely beneficial for electron transfer from one layer to the next as shown by Siddiki et al.^[76]

Fig. 4.33 shows the response of the surface potential to a square wave pulse. This square wave was achieved by simply turning the illumination on and off. Every drop in surface potential corresponds with the illumination being turned on. The drop in surface potential seen here is in the same order of magnitude and direction as shown by Maturová et al.^[55] Moreover, the response seems to be a process on a millisecond time scale

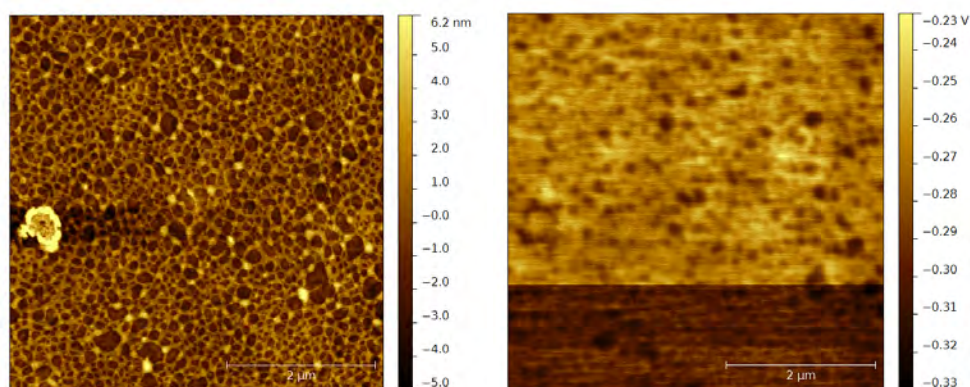


Figure 4.31: Morphology and the corresponding surface potential image ($5 \times 5 \mu\text{m}^2$) of a CPE covered sample with illumination of 0.7 sun (bottom part, top half is measured in dark).

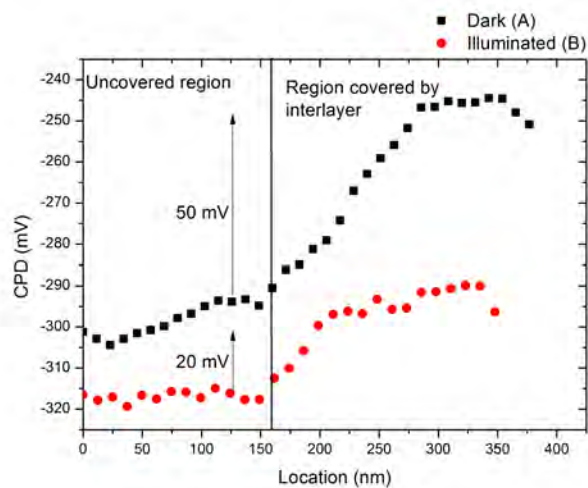
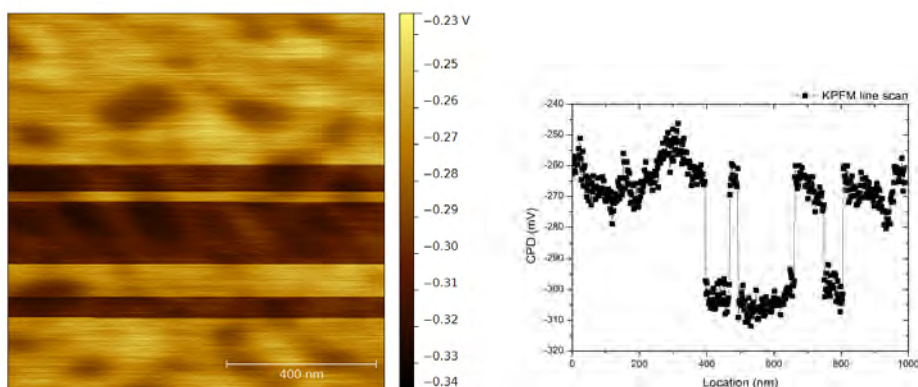


Figure 4.32: Linescan from the uncovered photoactive layer to the part covered by the interlayer at light and dark conditions.

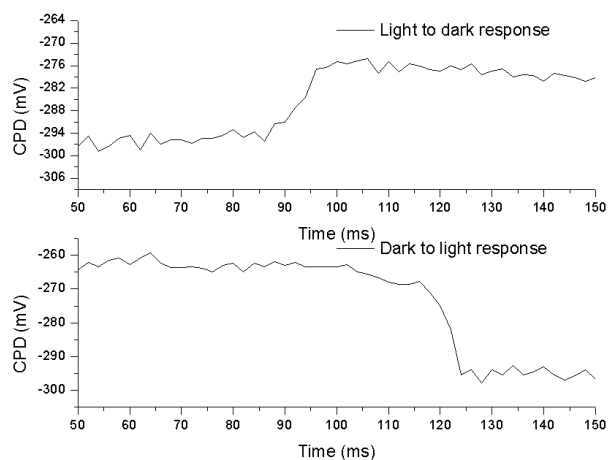
CHAPTER 4. RESULTS AND DISCUSSION

(fig. 4.33 (c)), indicating that the electrons transferred from the donor-acceptor blend are weakly bonded. This is of crucial importance as strong bonding would act as a trap center for electrons and thus not result in an increase in short circuit current.



(a) KPFM image

(b) Line scan



(c) Single line linescan

Figure 4.33: Response of the surface potential ($1 \times 1 \mu\text{m}^2$) to turning the light on and off and the corresponding linescan (a) and (b). The time response estimated from combining the scan rate and a single line scan when turning the illumination on (c)

4.2.7 Conclusions

The presented study confirms that high-efficiency polymer solar cells can be prepared by insertion of appropriate ionic polymer films at the electrode/active layer interface. Interface engineering provides a simple pathway to BHJ OPV efficiency improvement, but its full potential has yet to be explored. The imidazole-substituted ionic polythiophene introduced here combines a number of features that favor this ETL material above most competitive polymer and/or fullerene materials. It is a simple polythiophene derivative, prepared via the straightforward GRIM polymerization method - providing structural versatility and scalability - and its stability and alcohol solubility enable easy processing from environmentally acceptable solvents. The material also seems to be applicable to different polymer:fullerene active layers. Moreover, by tuning the chemical structure of the ionic polythiophene, further improvement is conceivable, e.g. by varying the density and organization of ionic groups at the surface. Additionally, we propose the following mechanisms to contribute to an increase in short circuit current and power conversion efficiency upon application of an imidazole-functionalized ionic polythiophene interlayer. First of all, the CPE layer acts as a hole blocking layer resulting in less recombination at the interface. Moreover, the addition of the CPE also increases the surface potential and thus has an influence on band alignment. Finally, it creates an extra built-in electric field promoting electron transfer from the active layer to the CPE under illumination. The SPM results suggest that increasing the coverage without increasing the ETL thickness should result in even higher device efficiencies.

4.3 Advanced scanning probe microscopy for perovskite based solar cells

Introduction

Perovskites are promising new materials for hybrid solar cells with reported efficiencies of over 15% for devices based on organometal halide perovskites (e.g., $\text{CH}_3\text{NH}_3\text{PbI}_{3-x}\text{Cl}_x$).^[50] However, there are still a multitude of unknowns about the current materials. Specifically their behaviour at the nanoscale is of interest as recent reports show different morphologies as measured by scanning electron microscopy depending on the different implementation method for perovskite based solar cells. It is well known from early research on polycrystalline silicon type absorbers, kesterite or chalcopyrite based layers and even organic solar cells that microstructure will have a significant impact on the electric characteristics of the eventual solar cells.^[1,32,39,53]

Edri et. al. have started a first investigation into the effect of this microstructure by using electron beam induced current (EBIC) on lead methylammonium tri-iodide perovskite based solar cells. Their research shows differences between $\text{CH}_3\text{NH}_3\text{PbI}_{3-x}\text{Cl}_x$ and $\text{CH}_3\text{NH}_3\text{PbI}_3$ suggesting a non-uniform grain behaviour in the latter case. Additionally by using KPFM they were able to show an upward bending for grain boundaries under illumination indicating the presence of a small potential barrier for electron transport in the case of $\text{CH}_3\text{NH}_3\text{PbI}_{3-x}\text{Cl}_x$.^[24,25] This work focusses on the use of scanning probe techniques to further elucidate the possible effect of grain boundaries on the electrical conduction in $\text{CH}_3\text{NH}_3\text{PbI}_{3-x}\text{Cl}_x$ thin films is. Conductive AFM and KPFM are the most viable options for this type of research as these techniques have been successfully applied on different types of absorber layers such as CIGS and CZTS and the results there showed that due to band bending at grain boundaries they mostly act as highly conductive pathways for charge carriers.^[1,43,48]

Results and discussion

A first logical step is an analysis of the surface by Kelvin Probe Force Microscopy as done by Edri et al.^[24] They found an upward band bending at the grain boundaries indicating the presence of a potential barrier for electron transport between grains. Under illumination the barrier was reduced and thus had no limiting effect on photovoltaic performance. Figure 4.34 shows the contact potential difference in dark and under white light illumination for the used mixed halide, the surface potential measured in dark and light do not show large variations over the measured surface, with the exception of a few grain boundaries, as expected for a phase pure material. As the V_{CPD} is defined as $V_{CPD} = \phi_{tip} - \phi_{sample}$ the work function of the sample will be defined as $\phi_{sample} = \phi_{tip} - V_{CPD}$ and a decrease of the CPD corresponds to an increase in work function at the grain boundaries, indicating the formation of a similar barrier as found by Edri et. al.^[24,25] These initial results are thus confirmed in different experiments by different groups, moreover, the behaviour of lead methylammonium tri-iodide perovskite appears to be opposite to that of polycrystalline kesterite thin films effectively suggesting that the grains and not the grain boundaries are the major centers of conduction.^[2,43]

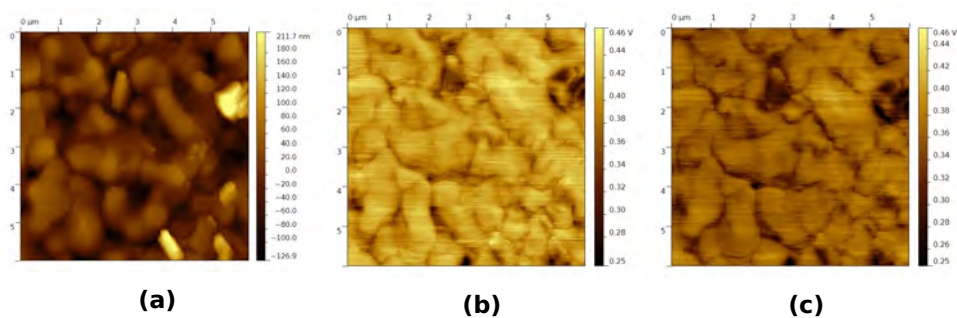


Figure 4.34: Local morphology (a) and contact potential difference ($6 \times 6 \mu\text{m}^2$) of $\text{CH}_3\text{NH}_3\text{PbI}_{3-x}\text{Cl}_x$. (b) Was measured in dark and (c) was measured using front side AM1.5G illumination.

CHAPTER 4. RESULTS AND DISCUSSION

Zhang et al. have shown that kelvin probe force microscopy is capable of measuring the conduction and valence bands of intrinsic semiconductors by relating the measured work function (Fermi level) to the conduction and valence band by adding or subtracting half of the bandgap energy to the measured surface work function.^[96] However, for doped semiconductors this analysis is no longer valid as n or p type doping shifts the fermi level closer to either conduction band or valence band. Taking into account a tip work function of 5.1 eV leads to an average surface fermi level of around 4.7 eV as calculated from the measured CPD by KPFM in dark (fig. 4.34 (b)). The conduction and valence band for $\text{CH}_3\text{NH}_3\text{PbI}_{3-x}\text{Cl}_x$ are usually quoted at 3.75 and 5.3 eV suggesting that the measured energy level in this work lies very close to the center of the bandgap. Moreover, this value of 4.7 eV coincides with the sub-band centered around 4.7 eV due to lead.^[17]

Illuminating the layer during measurement did result in an overall shift of the surface potential and some boundaries are indeed affected by the illumination and show an increase in CPD (fig. 4.35). The fact that not all edges show a surface photovoltage shift indicates that these edges belong to a single grain and that grain formation results in terrace structures, this idea is confirmed by the conductive AFM results as not all edges show zero current at a non-zero sample bias (Fig. 4.36 b and c).

Figure 4.36 shows the local morphology and current at a fixed positive and negative bias. Interestingly there seem to be areas with increased conduction and areas with no conduction under negative sample bias, the areas with increased conduction seem to coincide with what one would call grains while the non-conducting areas coincide with grain boundaries. Another interesting point is that the current does not appear to be uniform over the entire image but is uniform within a single grain. It would be easy to attribute the local differences in conduction to a different composition at the microscale as is done for CIGS absorbers.^[41] However, initial research

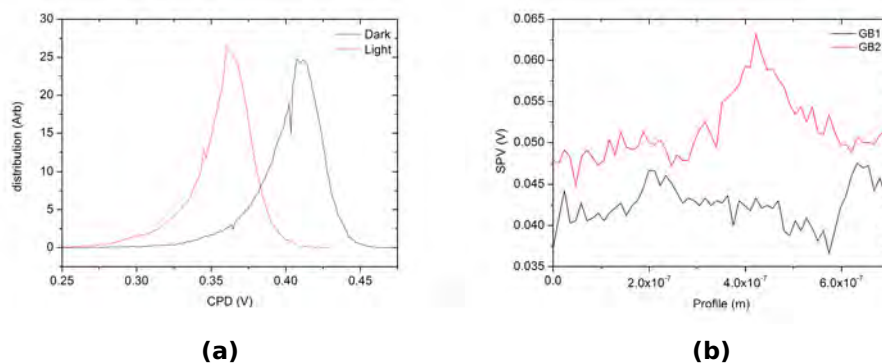


Figure 4.35: (a) Histogram of the dark and illuminated contact potential images. (b) Surface photovoltage measurement calculated from the dark minus the illuminated surface potential at two different locations to illustrate the effect of surface photovoltage at the grain boundaries.

showed that the material under investigation is a phase pure mixed halide perovskite with an orthorhombic crystal structure.^[17] Suggesting that all grains have near identical compositions and thus composition should not affect local current. EBIC measurements on $\text{CH}_3\text{NH}_3\text{PbI}_3$ showed a similar uniform grain to grain contrast as the C-AFM measurements in this work exhibit (fig. 4.36).^[24] The local variation in C-AFM current is a strong indication that the contrast seen in EBIC is not due to a local increase or decrease in charge generation but is related to either local transport mechanisms or charge recombination.

There is however the possibility that the contrast as seen here is a result of the barrier between individual grains and the TiO_2 film at the back contact. Recent research demonstrated that even the selection of the substrate has a strong influence on the structural properties of the film.^[28] It is therefore possible that as fairly large crystals are formed at slightly elevated temperatures certain stresses will occur and thereby could wedge and lift smaller preformed grains off the substrate. This could explain why certain smaller grains show no current at the sample bias voltages of -950 mV and 500 mV.

CHAPTER 4. RESULTS AND DISCUSSION

An important difference between the EBIC results as presented by Edri et. al. and the C-AFM results presented here is the fact that the differences in EBIC contrast for different grains were measured on $\text{CH}_3\text{NH}_3\text{PbI}_3$ while the C-AFM results from this work were obtained from $\text{CH}_3\text{NH}_3\text{PbI}_{3-x}\text{Cl}_x$. This suggests that the deposition method of lead halide based perovskites will have a profound influence on the formation and local properties, of grains and grain boundaries, which in turn will lead to significantly higher or lower devices efficiencies.^[17,36]

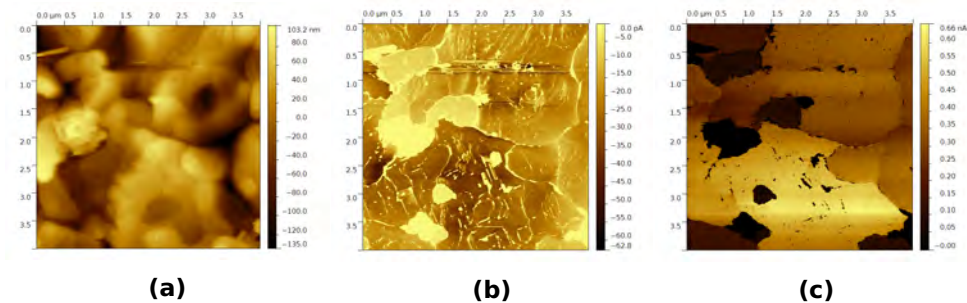


Figure 4.36: Local morphology (a) and conductive AFM ($4 \times 4 \mu\text{m}^2$) of $\text{CH}_3\text{NH}_3\text{PbI}_2\text{Cl}$. (b) Was measured at a negative sample bias of -950 mV and (c) was measured at a positive bias of 500 mV .

Additionally the measurements imply that the current as measured by AFM is contact limited. If the current is limited by the bulk any reduction in thickness should show up as an increase in current. However, from figure 4.37 it can be seen that halving the thickness of the layer does not result in a two-fold increase in current thereby adding to the idea that the current is mainly contact limited. Moreover, the results as shown here actually show a different behaviour at positive and negative bias. At positive bias only certain grain boundaries do not seem to conduct current while at a negative bias all edges have a reduced current. Any surface effects due to the formation of a water meniscus can be excluded as sample preparation and characterization were done in an inert and controlled atmosphere. Additionally, the presence of a water meniscus enhances the measured current, thereby showing that the non-conducting nature is

their true nature.

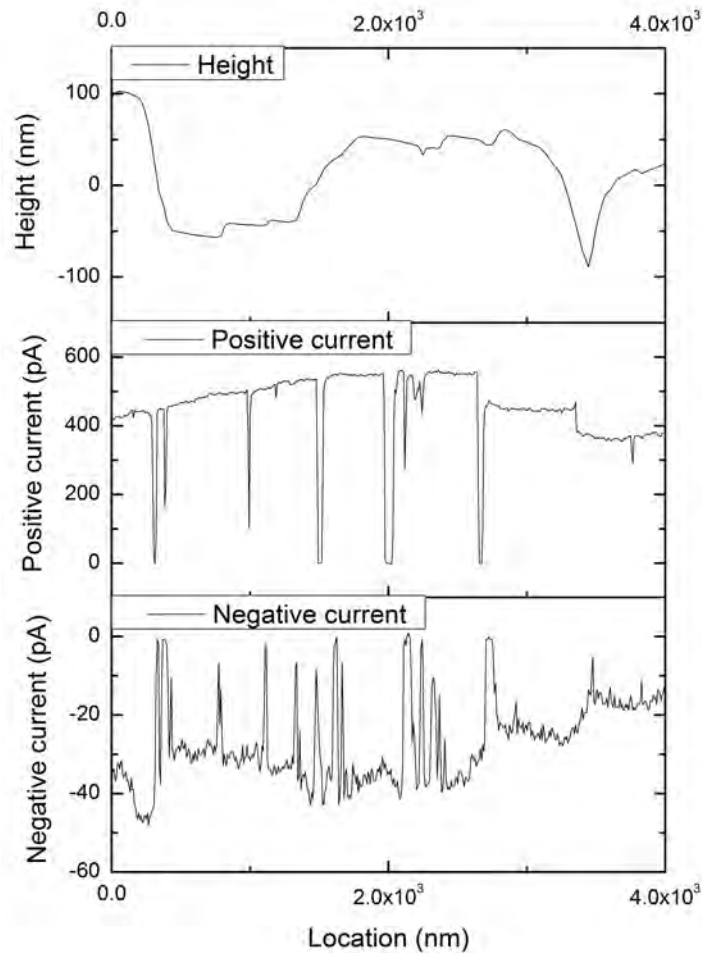


Figure 4.37: A linescan over of the images from figure 4.36 showing that the current is mainly contact limited.

Local composition as well as different surface fermi levels have been excluded as possible effects to explain the grain to grain differences in local conduction. A deeper investigation of the local IV curves is therefore needed. However, to understand the IV-curves it is first necessary to understand how the system behaves which heavily depends on the

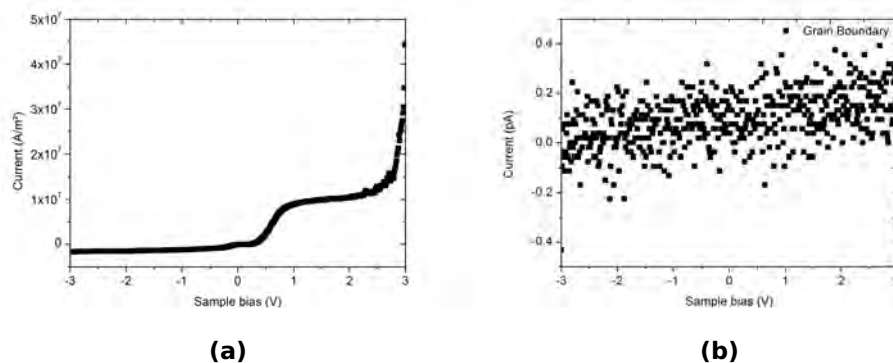


Figure 4.38: A JV-curve made on a grain (a) and on a grain boundary (b). The current through the grain differs from the current through the grain boundary indicating that the grain boundary itself is in this case non-conducting.

tip/sample interaction. The type of contact between a metal coated AFM tip and a semiconductor will determine the eventual behaviour of the system. Contacting a metal to a highly doped semiconductor will in turn lead to an ohmic contact, while contacting a metal to a low doped semiconductor will lead to a Schottky type contact.^[80] The average contact potential difference between AFM tip and sample in this case is at 0.4 eV as determined before from figure 4.34 (b) indicating that a substantial barrier between tip and sample exists and thereby implying that the interaction can be described by a Schottky contact.

Figure 4.38 shows the JV-characteristics of a grain and grain boundary, the tip size was estimated from calibration through a titanium roughness sample and analysed based on an algorithm developed by Villarrubia and implemented in Gwyddion.^[62,83] As the interface is considered as a Schottky type contact applying a positive sample bias actually sets the device in reverse and in that case the current can be described by the Richardson equation.

$$J_R = R^* T^2 \exp(-q\Phi_B/kT) (\exp(-qV/kT) - 1) \quad (4.1)$$

With R^* the effective Richardson constant, q the elementary charge, T

the temperature, k the boltzmann constant, Φ_B the potential barrier and V the applied voltage. The JV-curves between 0.5V and 1.5V imply that the barrier Φ_B is not fixed but depends linearly on the applied voltage. Applying a sufficiently high bias completely suppresses the barrier (fig. 4.38 (a)).

A second possible mechanism to describe the bump in the current voltage characteristics takes into account the ambipolar nature of lead halide based perovskite. As the TiO_2 lines up with the conduction band and the barrier between the Pt/Ir tip and the valence band should remain low, applying a positive bias to the TiO_2 results in an electron current travelling from the oxide into the conduction band onto the Pt/Ir tip, while holes might initially be blocked. At increasing bias holes could be injected over the barrier into the valence band and travel towards the TiO_2 , there however, they will be blocked due to a mismatch in energy levels resulting in a build up of positive charge. This positive charge could shield the electrons from the applied field, nonetheless at higher bias the applied electric field is sufficiently large to overcome any shielding effect from the holes at the TiO_2 . Recombination between electrons and holes is not excluded, nevertheless, recombination acts over the entire voltage range not necessarily only between 0.6 and 2.0 V. Plotting the current in function of the square root of the voltage (Fig. 4.39) shows a linear behaviour from 2.6 V (1.6 $\text{V}^{1/2}$) and higher which suggests a Schottky like behaviour.

The JV-data from figure 4.38 (b) clearly shows that the measured grain boundary does not show conduction over the applied voltage range indicating that the grain boundaries are not contributing to conduction.

Conclusions

In conclusion we have shown that kelvin probe force microscopy and conductive AFM can be used to analyse perovskite based layers. From

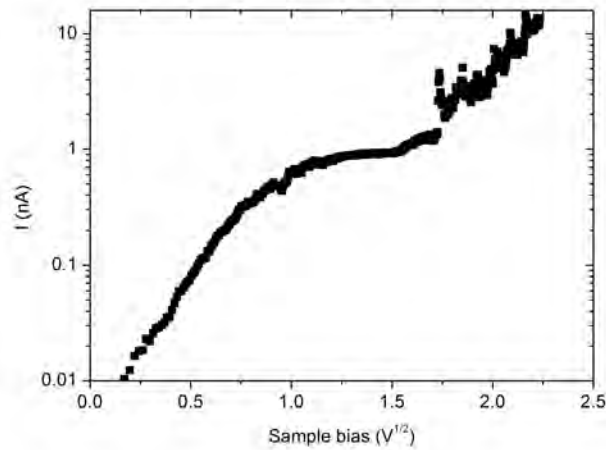


Figure 4.39: Current as measured by AFM through a grain for a positive sample bias including the range at higher voltage.

illuminated KPFM it is deduced that the grain boundaries show reduced band bending while under a white light bias. From the conductive AFM results it is clear that grains exist in this material and not all grains show the same current however, it has to be noted that this current is limited by the contact between tip and sample. An analysis of the current voltage curves of a grain showed that the peculiar bump can be explained by either a potential barrier at the tip sample interface or by charge build up at the perovskite - TiO_2 interface due to the mismatch in energy levels. Moreover, grain boundaries do not show a measurable current. These results indicate that decreasing the amount of grain boundaries should result in higher device efficiencies.

4.4 Visualizing thermally and atmospheric induced degradation of the cathode in polymer solar cells

4.4.1 Introduction

In recent years the field of organic photovoltaics has seen increases in power conversion efficiency from a mere 1% with MDMO-PPV as a donor polymer to 10% for the PCE-10:PC₇₁BM system. At this point, next to the study of power conversion efficiency, also the study of degradation and failure mechanisms gains importance. As the stability of organic photovoltaic devices will be determined by the different layers and their interaction at elevated temperatures it is of the utmost importance to properly characterize the behaviour at each of these layers. A thorough characterization of the polymer:fullerene blend has been reported in literature by several groups.^[6,64,77,82] Degradation of the photoactive layer is commonly studied by transmission electron microscopy to investigate the nanoscale in-blend phase separation. Another relevant technique is atomic force microscopy (AFM) and its derived techniques. Douhéret et al. have shown that phase separated blends show interesting properties for each of the different material phases by using Kelvin Probe Force Microscopy and conductive AFM.^[21] Maturová et al. showed that it was possible to relate the local electrical properties obtained from KPFM to the macroscopic behaviour via a two dimensional drift diffusion model. Moreover, this model allowed an initial description of degraded cells.^[54,56] Contact degradation, another possible failure mechanism, has been studied as well and recently Vorozashi et al. demonstrated that two distinct degradation mechanisms for the cathode at long degradation times exist.^[84] However, even right after deposition voids at the calcium interface already exist suggesting that even right after deposition contact degradation can occur.^[51] In particular the work presented below investigates

the effect of cathode degradation at short times utilizing advanced atomic force microscopy techniques to study changes in local potential and SEM to relate these changes in local potential to the actual local composition.

4.4.2 Results and Discussion

Figure 4.40 shows an overview of the characteristics of solar cells annealed at different temperatures for two hours. All samples which had a cathode and an anode were analysed before annealing (PRE) and after annealing (POST). The samples described as POST-fresh Ca/Al consisted of a glass/ITO/PEDOT:PSS/BHJ stack without any calcium/aluminium anode but were annealed at 85, 110 and 150 °C for two hours, the anode was deposited after this annealing step. The results as shown here clearly show that samples annealed with an anode clearly have a reduced efficiency. This drop in efficiency is due to a drop in current, open circuit voltage and fill factor. The samples that had the top contact deposited after annealing did not show such a reduction in power conversion efficiency, thereby indicating that the annealing has a limited effect on the polymer layer. The main issue in this case is thus the effect of the calcium aluminium contact.

As standard tapping mode atomic force only shows topography an additional technique such as Kelvin Probe Force Microscopy (KPFM) can be used to study the electronic properties of the surface.^[33,49,66] Figure 4.41 shows the topography and surface potential as obtained from KPFM from the reference sample, this figure (4.41 a and c) clearly shows that the blend has a fine intermixing as can be expected from deposition by spin-coating. Moreover, this figure shows that both the blend and the aluminum top contact have a well-defined structure. The roughness of the reference blend is 9.8 nm (table 4.11), while the roughness of the aluminum contact is 8.6 nm. The peak to peak distances for BHJ and aluminum contact show a similar trend. This all indicates that the aluminium follows the morphology of the BHJ rather well. The average surface potential difference

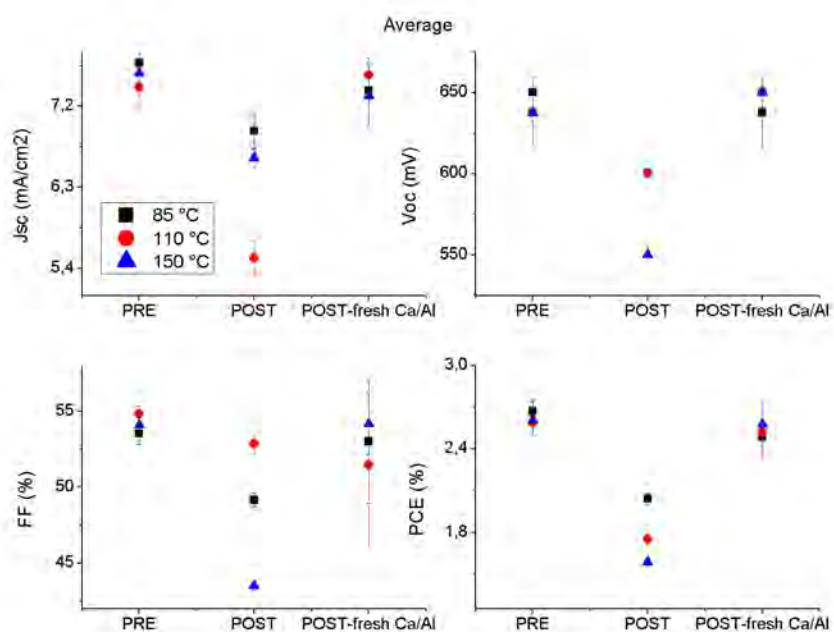


Figure 4.40: An overview of the characteristics of annealed P3HT:PCBM solar cells. The cells were annealed at different temperatures for two hours. Depending on the sample set, they were either annealed with contact 'POST' or annealed without contact 'POST-fresh Ca/Al'. This dataset clearly shows the effect of the contact when annealing the complete cell compared to annealing just the absorber layer.

CHAPTER 4. RESULTS AND DISCUSSION

between tip and blend is 1.01 eV, it can be noted that this difference is of the same order as the difference between the HOMO level of P3HT and the work function of aluminum. Additionally it can be seen that the morphology of the aluminium layer has no influence on the corresponding surface potential, which is expected when using KPFM with a fixed tip-sample distance.

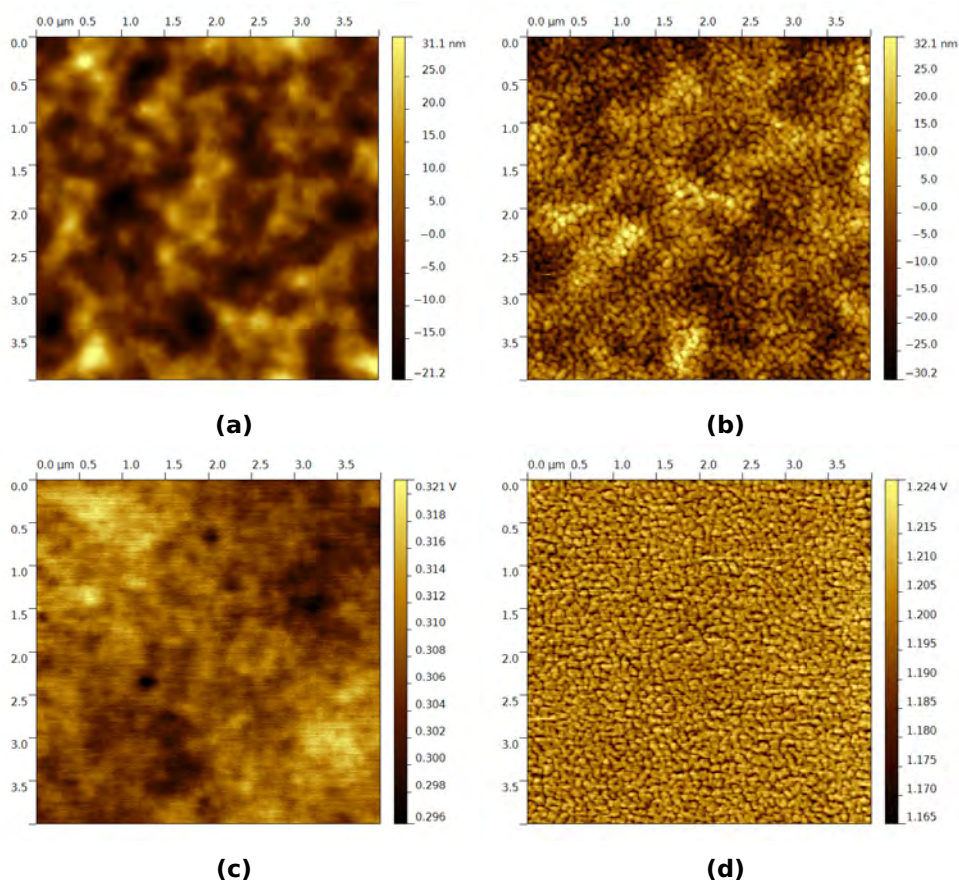


Figure 4.41: The morphology and kelvin probe signal ($4 \times 4 \mu\text{m}^2$) of the aluminium top contact (b,d) and the P3HT:PCBM blend (a,c) of the non-annealed (reference) sample.

When looking at the morphology of the blends annealed at different temperatures (Figure 4.42) it becomes apparent that the roughness or the peak to peak distance as measured on the different blends do not

CHAPTER 4. RESULTS AND DISCUSSION

change significantly. Moreover, it can be seen that the films still don't exhibit phase separation in the form of PCBM clusters.^[79] Which is a microstructural confirmation of the parameters extracted from the JV-curves of the samples annealed without an anode. However, the temperatures reached in this experiment are well above the glass transition temperatures of P3HT:PCBM blends which are quoted at 35 to 40 °C.^[63] Moreover, it has been established in literature that the linear expansion coefficient of P3HT is in the order of $5 \times 10^{-4} K^{-1}$ while the linear expansion coefficients of glass, ITO, calcium and aluminium are in the order of $5 - 8 \cdot 10^{-6} K^{-1}$. Combining both the two orders of magnitude difference in thermal expansion coefficient and the glass transition temperatures it becomes clear that the annealing will have a significant impact on the interface between Ca/Al and the bulk heterojunction layer. Additionally, the contact potential difference (Fig. 4.42 (d)-(f)) remains uniform over the measured surface irrespective of the annealing temperature.

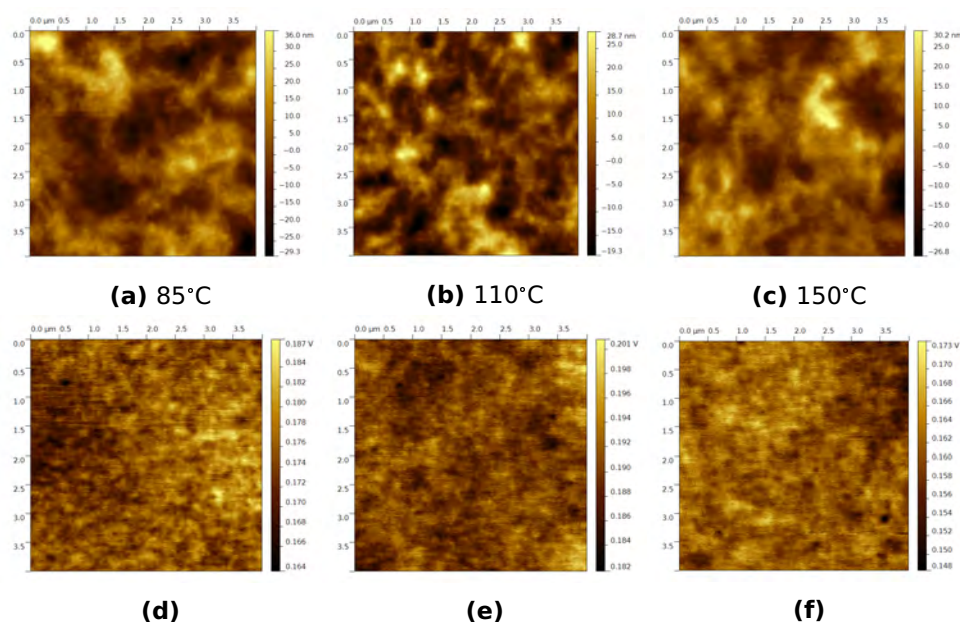


Figure 4.42: Topography (a-c) and corresponding KPFM signals (d-f) ($4 \times 4 \mu\text{m}^2$) of the donor-acceptor blend annealed at different temperatures.

CHAPTER 4. RESULTS AND DISCUSSION

As can be seen in Figure 4.43 the morphology of the aluminum top contact changes significantly upon annealing at increased temperatures, the roughness increases and peak to peak distances of 98 nm (85 °C) to 215 nm (150 °C) are measured on these samples. These changes in morphology are accompanied by changes in the surface potential. The sample annealed at 85 °C shows an increased surface potential in the top right corner, indicating that the temperature as applied here already has an influence. Annealing at 110 °C has a more pronounced influence both on morphology and surface potential. The original morphology for the aluminium as seen in figure 4.41 (b) is no longer visible, the aluminium appears to have molten together and these areas have an increased surface potential. Annealing at 150 °C significantly increases this effect, the aluminium in this case has large areas in which the original nano particle morphology is no longer present. Moreover, the surface potential is far from uniform and while at 110 °C the islands had an increased surface potential this is no longer valid at 150 °C. There are two important questions in relation to this phenomenon. The first question is what the effect of these islands is on the solar cell characteristics and the second is why or how are they formed. These questions are closely related to each other as any change in electronic structure or morphology will have an effect on the solar cells characteristics.

There are several options as to why the behaviour seen here exists. A first option would be a thermal degradation of the aluminium, if this would be the case then a simple deposition of aluminium on glass and annealing should be sufficient to reproduce the effect. The topography in figure 4.44 shows topography of aluminium deposited on glass and annealed at the aforementioned temperatures, the peak to peak distances of all samples are all in the order of 20 nm nor is any effect of melting or merging seen.

A second option is the formation of PCBM clusters under the contacts. Although not impossible this is highly unlikely as kelvin probe force mi-

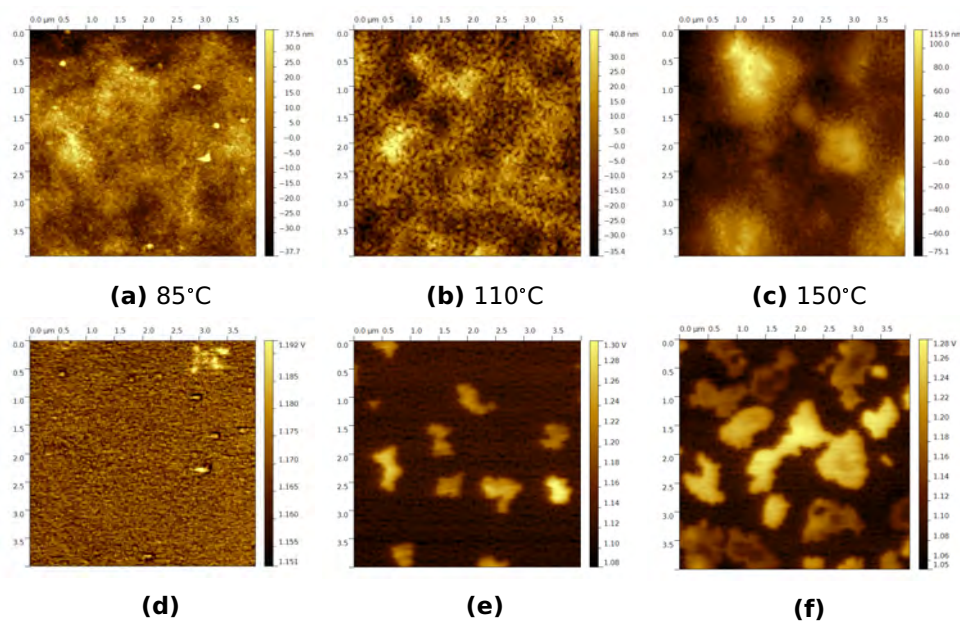


Figure 4.43: Topography (a-c) and KPFM signal (d-f) ($4 \times 4 \mu\text{m}^2$) of the aluminium top contact from the samples annealed at different temperatures. The image averaged KPFM signals are displayed in table 4.11.

scopy did not show the formation of PCBM clusters in the photo-active layer (cf. figure 4.42), nevertheless to exclude this as a possible effect the contact of the sample annealed at 150 °C was etched away using HF and measured with KPFM and these results are shown in figure 4.45. The measured surface potential of the blend under the contact is uniform and does not show the large variations as can be seen on the contact (fig. 4.43 (f)). The peak to peak distance as determined from the morphology however is in this case similar to that of the aluminium, this indicates that the morphology under the contact does change significantly thereby explaining as to why the short circuit current and the fill factor drop. Moreover, a KPFM measurement on a PCBM needle shows that the surface potential should go down in the presence of a needle (fig. 4.46), not up. Additionally, the height of such needles is usually far higher than height as measured on the annealed samples in the experiments done here.

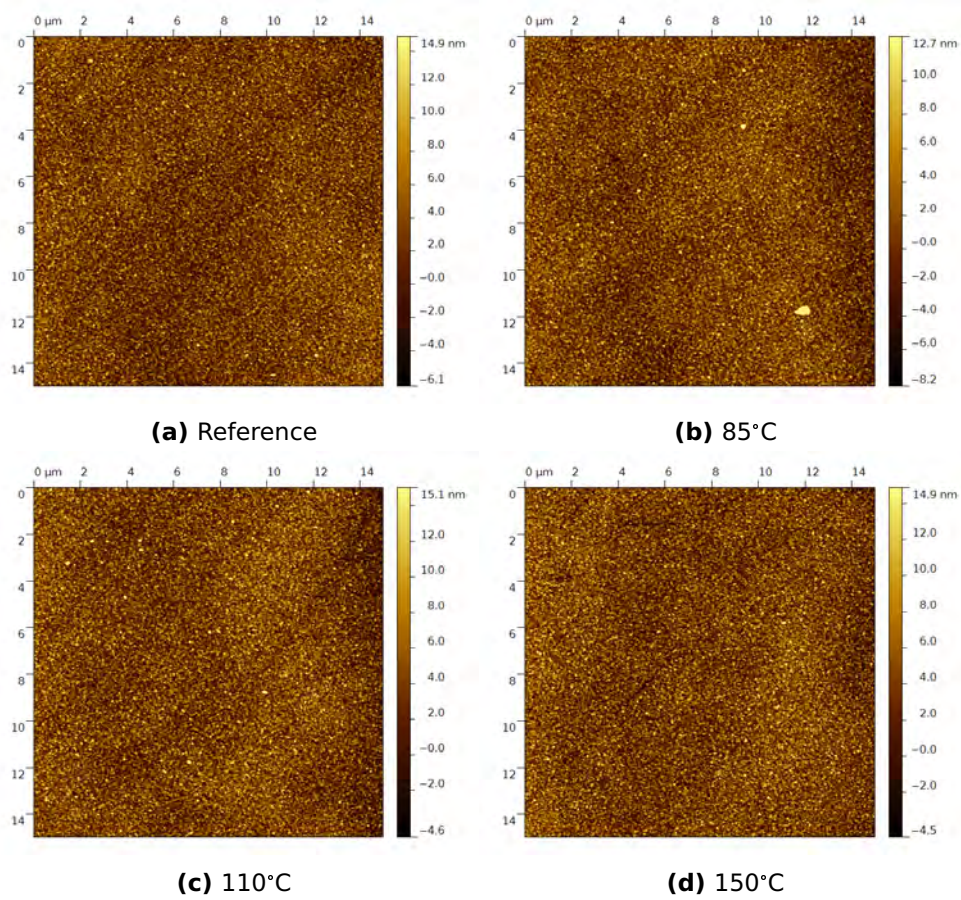


Figure 4.44: Topography ($15 \times 15 \mu\text{m}^2$) of aluminium deposited on glass and annealed at different temperatures for 2 hours.

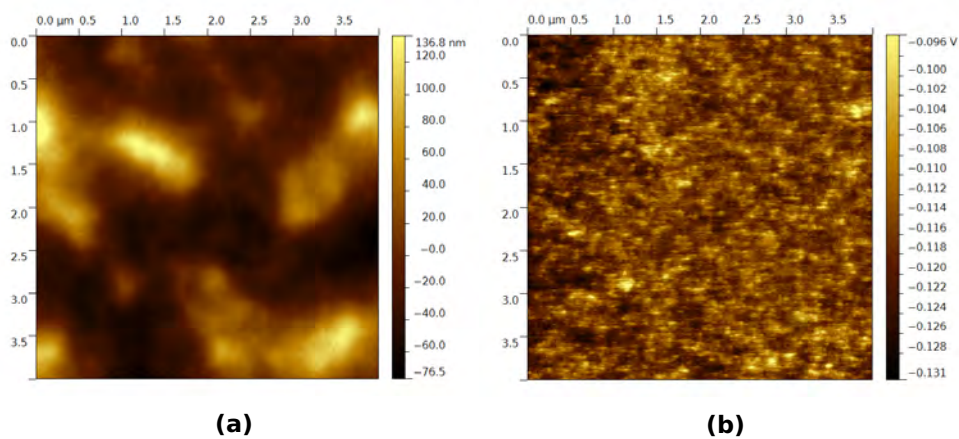


Figure 4.45: Topography and surface potential measurement ($4 \times 4 \mu\text{m}^2$) of a sample annealed at $150 \text{ }^\circ\text{C}$ of which the aluminium was etched away using HF.

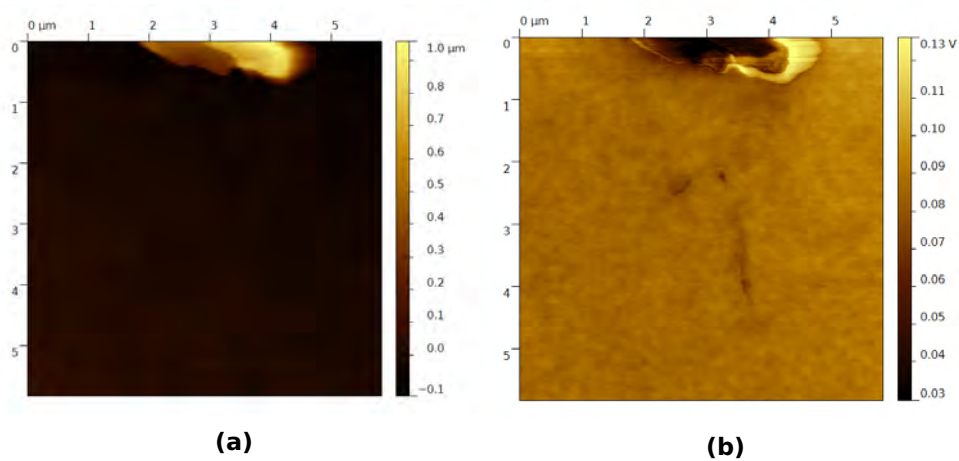


Figure 4.46: Topography and corresponding surface potential measurement ($6 \times 6 \mu\text{m}^2$) of a PCBM needle in a P3HT:PCBM blend.

The third and final option would be the effect of calcium and it is well known that calcium is a highly reactive material however, most research only investigates either the reactivity of the calcium with the photo-active layer or investigates the effect of oxidation on the calcium interlayer.^[64] Figure 4.47 gives an overview of the surface potential results of calcium-/aluminium deposited on ITO. Even without any organic absorber layer a similar effect is seen (cf. Fig. 4.43), indicating that the results as measured before can be attributed solely to the presence of calcium. The degradation of the underlying calcium can happen through oxidation due to the presence of molecular oxygen or water. The oxidation process as described before is highly unlikely as X-ray photoelectron spectroscopy (XPS) results on samples which degraded completely in air show that the calcium oxide remains in between the organic absorber layer and the aluminium anode.^[51] Moreover, the morphology of the Ca/Al on ITO annealed at 110 °C shows that the areas with an increased surface potential have a decrease in height at the exact locations where the surface potential is increased. The fact that the height appears to decrease indicates a different process and suggest that diffusion of calcium might have an influence.

The fact that this process is more pronounced for higher temperatures indicates that it is temperature mediated and that the effect should increase with longer annealing times at higher temperatures. This is indeed the case as can be seen in figure 4.48 which shows a calcium aluminium layer annealed for 10 hours at 85°C. The shape as seen here is different from those annealed at higher temperatures, however, the change in surface potential is identical suggesting that this is the same process. Moreover, the changes in surface potential are again correlated to a change in height. A possible explanation is the inter-diffusion of metals as it is a process which is temperature mediated moreover, this is solely linked to the contact and thus this degradation is independent of the degradation of the photo-active layer. And while 150 °C is far higher than any temperature used in thermal degradation studies, 85 °C is not.

CHAPTER 4. RESULTS AND DISCUSSION

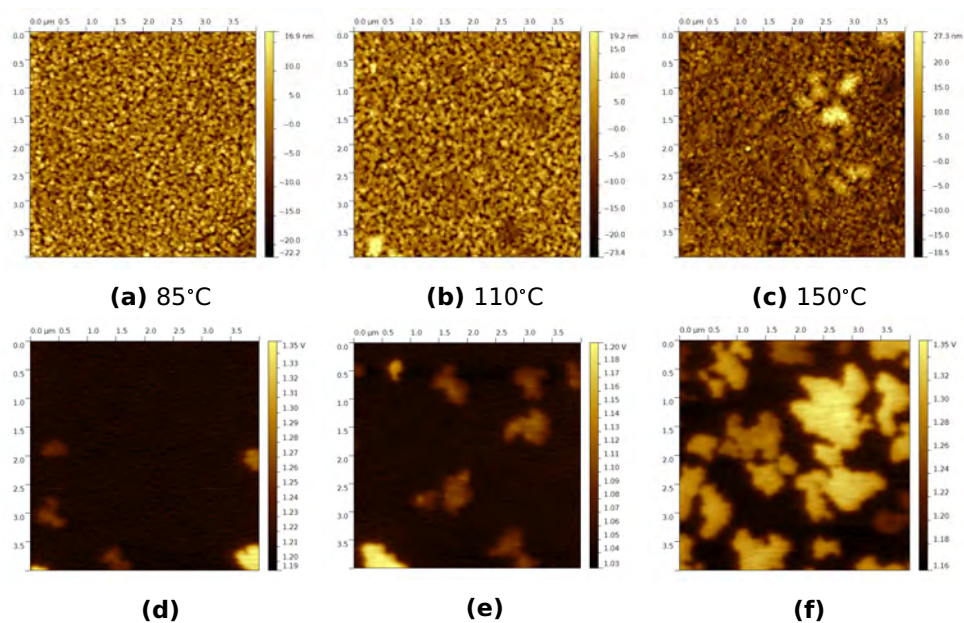


Figure 4.47: Visualization of the morphology (a-c) and KPFM signal (d-f) of the Al/Ca top contact deposited on ITO and annealed at different temperatures. Images are on a $4 \times 4 \mu\text{m}^2$ scale and the image averaged KPFM signals are displayed in table 4.11.

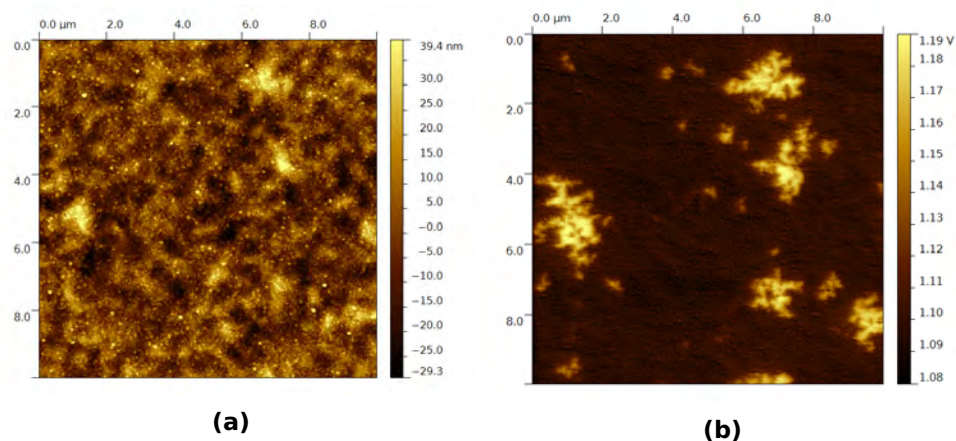


Figure 4.48: Topography and correspond surface potential measurement ($10 \times 10 \mu\text{m}^2$) of Al/Ca evaporated on P3HT:PCBM and annealed at 85 °C for 10 hours.

CHAPTER 4. RESULTS AND DISCUSSION

To further investigate the proposed theory of calcium diffusion through the aluminium matrix SEM and energy dispersive X-ray spectroscopy (EDX) analyses were done on the Ca/Al layers deposited on ITO/glass. The secondary electron (SE) images made using an acceleration voltage of 5 kV are presented in figure 4.49 as the resulting image should present contrast based on the local morphology of the film and the used acceleration should limit the size of the interaction volume as to probe mostly the top layer. Astoundingly, contrast is already present in the as deposited film, however, the number density of the dark areas is rather low and thereby explains why this did not show up in the corresponding KPFM images. The number density of the dark areas does increase with increasing temperatures moreover, the shape as determined by secondary electron imaging corresponds with the shapes seen during KPFM imaging and thus confirming that the same effect is visible to both techniques.

Energy-dispersive X-ray spectroscopy (EDX) was employed to determine the elemental composition in these darker areas compared to the surrounding film. The results of the film annealed at 110°C are shown in figure 4.50. Comparing the two EDX spectra taken at location A and B reveals that at those locations the amount aluminium seem to be reduced while calcium does appear to be present there. To be able to properly detect calcium when it is not present at the surface an energy of at least 8 kV is needed, as the peak of calcium is present here this clearly indicates that the element is present in larger quantities and near the surface thereby proving the existence of calcium towards the surface. Additionally it has to be mentioned that the peaks corresponding to oxygen and indium are higher while the peak corresponding to aluminium is lower in location B compared to location A. This strongly indicates that the aluminium content is lower in location B therefore, the underlying materials are more readily detected. A similar behaviour was seen in the spectra taken on the samples at different annealing temperatures.

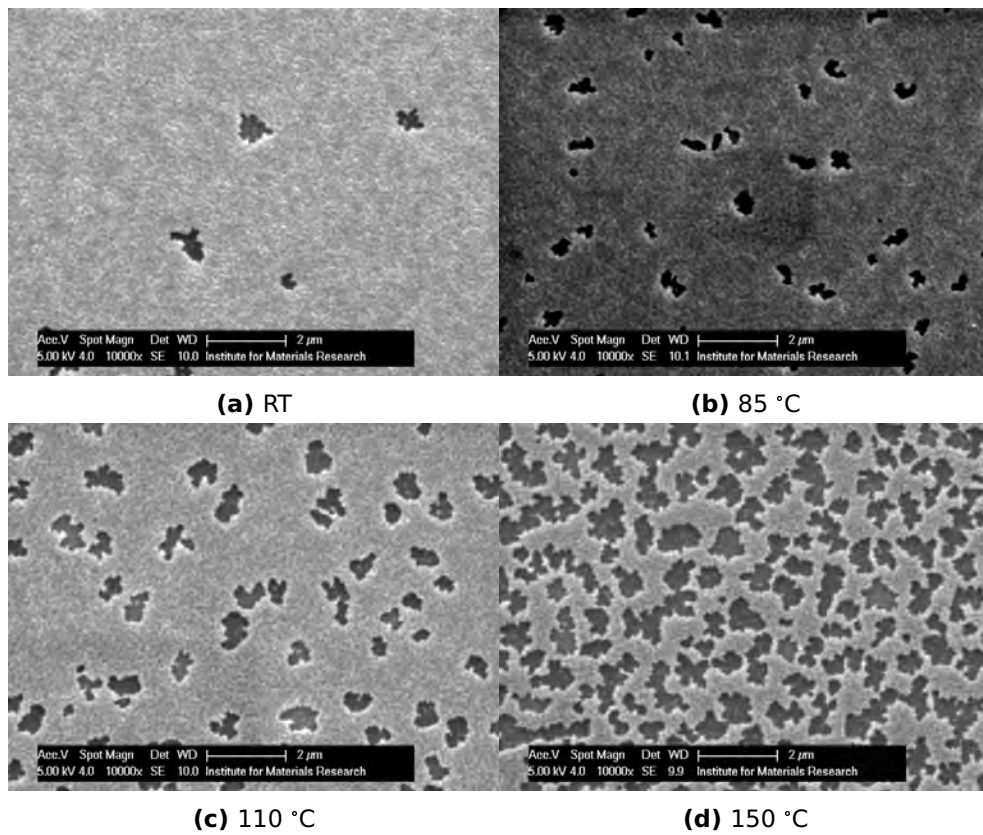
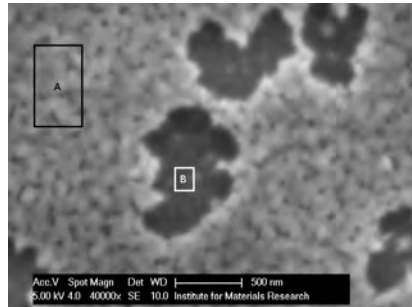
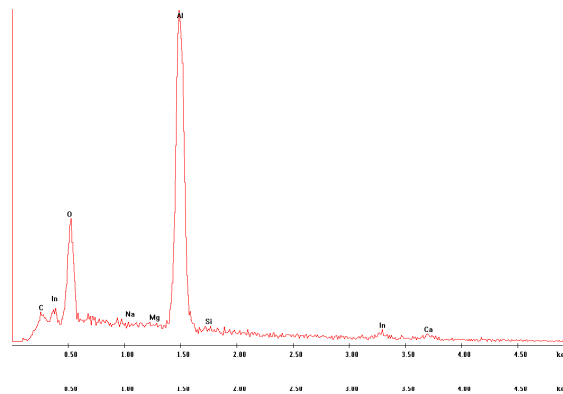


Figure 4.49: An overview of the secondary electron images of Al/Ca deposited on ITO/Glass and annealed at different temperatures.

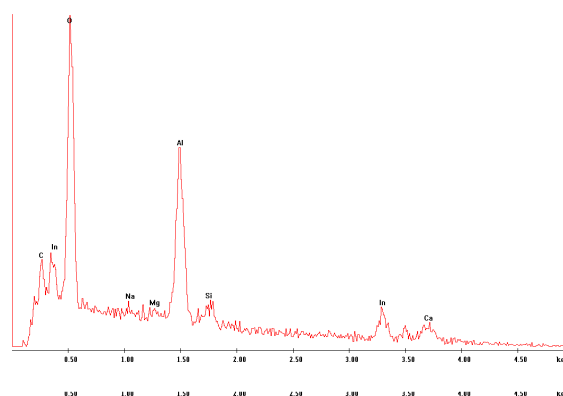
CHAPTER 4. RESULTS AND DISCUSSION



(a)



(b)



(c)

Figure 4.50: Secondary electron image of Al/Ca deposited on ITO/Glass and annealed at 110 °C and the EDX spectra taken at location A (b) and location B (c). The following elements are indicated in order on the EDX spectra: C, In, O, Na, Mg, Al, Si, In, Ca.

The non annealed calcium/aluminium thin film was hereafter left in ambient atmosphere for 70h and measured again with SEM and EDX. The resulting SE and BSE images are clearly different, showing that oxidation takes on a completely different form.

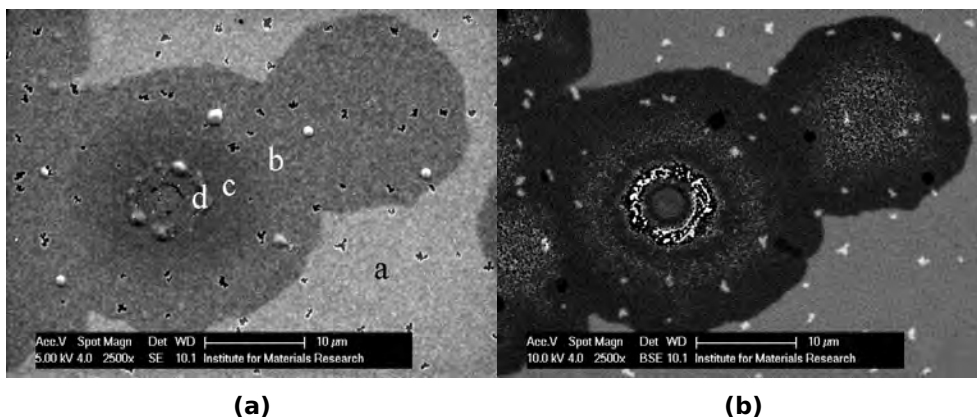


Figure 4.51: SE (a) and BSE (b) images of a non-annealed oxidized calcium aluminium layer.

Figure 4.52 shows the EDX spectra taken on the different locations as indicated in figure 4.51, locations b,c and d clearly show increased amounts of oxygen compared to location a. This shows that oxidation is a completely different process.

A general downward trend with annealing is visible when studying the contact potential difference between aluminium top contact and blend (table 4.11). These islands are not associated with the formation of PCBM clusters as the formation of such a large amount of clusters should show a significant change in solar cell parameters and these islands should be visible in the KPFM signal of the blends (Figure 4.42).^[88] To answer the question on how these changes in local surface potential influence the solar cell characteristics one has to take into account the fact that the open circuit voltage of organic solar cells is generally influenced by two factors, the first one is the difference in HOMO and LUMO between donor and ac-

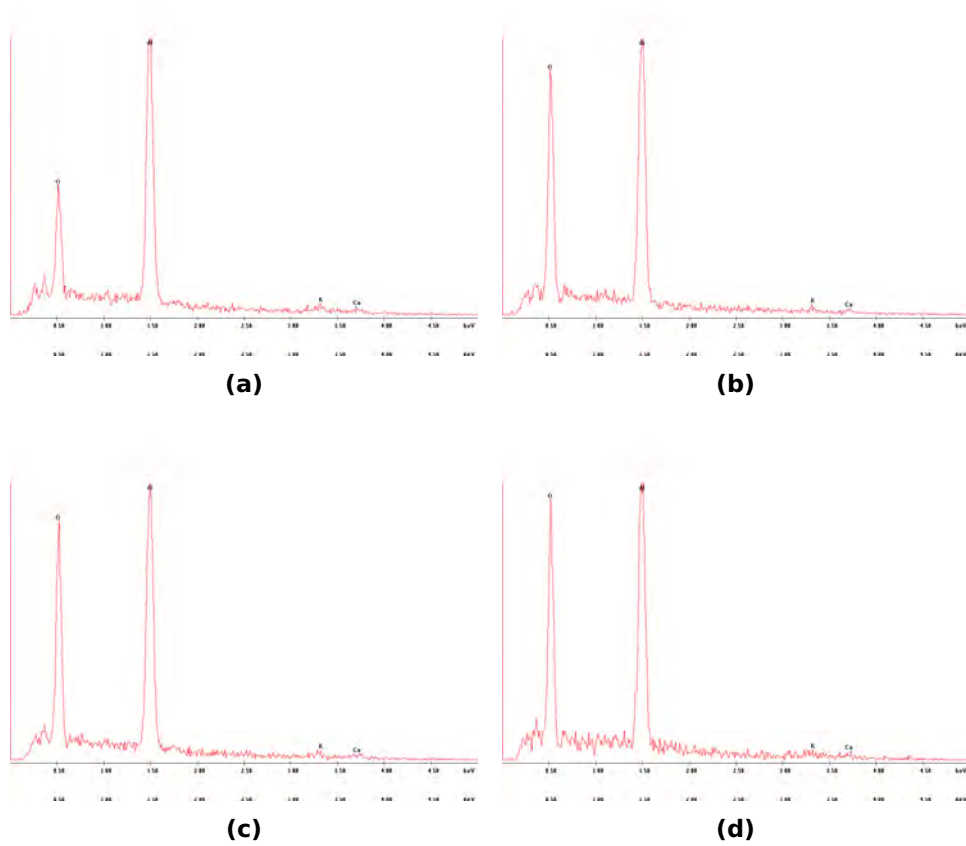


Figure 4.52: The EDX spectra as taken at locations (a), (b), (c) and (d). Locations (b) to (d) seem to have nearly identical spectra while location (a) shows a lower amount of oxygen. The following elements are indicated in order on the EDX spectra: O, Al, K, Ca.

CHAPTER 4. RESULTS AND DISCUSSION

ceptor.^[81] The second factor is the alignment of the workfunction of the cathode to the LUMO of the acceptor and of the anode to the HOMO of the donor. As the blend remains well intermixed the HOMO-LUMO difference should remain constant. However, the variation in surface potential of the top contact does seem to increase with temperature and thus could explain the average downward trend in V_{oc} .

Table 4.11: Overview of the parameters of the measured cells annealed with contact (W c) and annealed without contact (W/o C).

Sample	Voc (V)	Jsc (A/m ²)	η	CPD Cathode(eV)	Rq - Al (nm)	Rq - Blend (nm)	Peak to peak distance Al (nm)	Peak to peak distance blend (nm)
Reference	0.64	75.5	2.62 ± 0.08	1.20 ± 0.01	9.8	8.6	89	60
85°C (W C)	0.60	69.3	2.04 ± 0.04	1.17 ± 0.01	9.8	9.0	98	86
110°C (W C)	0.60	55.1	1.75 ± 0.04	1.14 ± 0.03	11.6	8.3	104	57
150°C (W C)	0.55	66.3	1.59 ± 0.02	1.09 ± 0.05	35.6	8.2	215	67
85°C (W/o C)	0.64	73.7	2.48 ± 0.12	1.14 ± 0.01	8.4	7.0	80	48
110°C (W/o C)	0.65	73.1	2.52 ± 0.21	1.10 ± 0.01	9.8	7.8	91	48
150°C (W/o C)	0.65	73.1	2.58 ± 0.16	1.13 ± 0.01	9.1	6.7	78	52

4.4.3 Conclusions

In conclusion we have shown that kelvin probe force microscopy is a valid technique to study the possible degradation of (metallic) contacts used in organic solar cells. An analysis of cells annealed with contact and without contact showed that the degradation can be exclusively linked to the degradation of the top contact additionally, the formation of PCBM clusters has been excluded both by analysing a PCBM cluster in a P3HT matrix and by removing the aluminium contact and subsequent analysis of the P3HT:PCBM surface. Moreover, additional SEM and EDX measurements showed that annealing resulted in a local thinning of the aluminium layer and possible diffusion of calcium throughout the aluminium layer. Finally, oxidation was excluded as a possible effect.

Bibliography

- [1] D. Azulay, O. Millo, I. Balberg, H.-W. Schock, I. Visoly-Fisher, and D. Cahen. Current routes in polycrystalline CuInSe₂ and Cu(In,Ga)Se₂ films. *Solar Energy Materials and Solar Cells*, 91(1):85–90, Jan. 2007.
- [2] R. Baier, J. Lehmann, S. Lehmann, T. Rissom, C. Alexander Kaufmann, A. Schwarzmann, Y. Rosenwaks, M. C. Lux-Steiner, and S. Sadewasser. Electronic properties of grain boundaries in Cu(In,Ga)Se₂ thin films with various Ga-contents. *Solar Energy Materials and Solar Cells*, 103:86–92, Aug. 2012.
- [3] C. Baumgart, M. Helm, and H. Schmidt. Quantitative dopant profiling in semiconductors: A Kelvin probe force microscopy model. *Physical Review B*, 80(8):1–5, Aug. 2009.
- [4] C. Baumgart, A.-D. Müller, F. Müller, and H. Schmidt. Kelvin probe force microscopy in the presence of intrinsic local electric fields. *Physica Status Solidi (a)*, 208(4):777–789, Apr. 2011.
- [5] Z. M. Beiley, E. T. Hoke, R. Noriega, J. Dacuña, G. F. Burkhard, J. a. Bartelt, A. Salleo, M. F. Toney, and M. D. McGehee. Morphology-Dependent Trap Formation in High Performance Polymer Bulk Heterojunction Solar Cells. *Advanced Energy Materials*, 1(5):954–962, Oct. 2011.
- [6] S. Bertho, G. Janssen, T. J. Cleij, B. Conings, W. Moons, A. Gadisa, J. D’Haen, E. Goovaerts, L. Lutsen, J. Manca, and D. Vanderzande. Effect of temperature on the morphological and photovoltaic stability of bulk heterojunction polymer:fullerene solar cells. *Solar Energy Materials and Solar Cells*, 92(7):753–760, July 2008.
- [7] N. Blouin, A. Michaud, D. Gendron, S. Wakim, E. Blair, R. Neagu-Plesu, M. Belletête, G. Durocher, Y. Tao, and M. Leclerc. Toward a rational design of poly(2,7-carbazole) derivatives for solar cells. *Journal of the American Chemical Society*, 130(2):732–42, Jan. 2008.

BIBLIOGRAPHY

- [8] N. Blouin, a. Michaud, and M. Leclerc. A Low-Bandgap Poly(2,7-Carbazole) Derivative for Use in High-Performance Solar Cells. *Advanced Materials*, 19(17):2295–2300, Sept. 2007.
- [9] J.-C. Bolsée, W. D. Oosterbaan, L. Lutsen, D. Vanderzande, and J. Manca. The Importance of Bridging Points for Charge Transport in Webs of Conjugated Polymer Nanofibers. *Advanced Functional Materials*, 23(7):862–869, Feb. 2013.
- [10] D. Bondarev and J. Zedník. Synthesis and properties of cationic poly-electrolyte with regioregular polyalkylthiophene backbone and ionic-liquid like side groups. *Journal of Polymer Science Part A: Polymer Chemistry*, 48:3073–3081, 2010.
- [11] M. Brinkmann. Structure and morphology control in thin films of regioregular poly(3-hexylthiophene). *Journal of Polymer Science Part B: Polymer Physics*, 49(17):1218–1233, Sept. 2011.
- [12] Bruker. PeakForce QNM - Quantitative Nanomechanical Property Mapping, 2010.
- [13] a. Carbone, B. Kotowska, and D. Kotowski. Space-Charge-Limited Current Fluctuations in Organic Semiconductors. *Physical Review Letters*, 95(23):236601, Nov. 2005.
- [14] Y. Chen, Z. Jiang, M. Gao, S. E. Watkins, P. Lu, H. Wang, and X. Chen. Efficiency enhancement for bulk heterojunction photovoltaic cells via incorporation of alcohol soluble conjugated polymer interlayer. *Applied Physics Letters*, 100(20):203304, 2012.
- [15] S. Cho, J. H. Seo, S. H. Park, S. Beaupré, M. Leclerc, and A. J. Heeger. A thermally stable semiconducting polymer. *Advanced materials (Deerfield Beach, Fla.)*, 22(11):1253–7, Mar. 2010.
- [16] H. Choi, J. S. Park, E. Jeong, G.-H. Kim, B. R. Lee, S. O. Kim, M. H. Song, H. Y. Woo, and J. Y. Kim. Combination of titanium oxide and

BIBLIOGRAPHY

- a conjugated polyelectrolyte for high-performance inverted-type organic optoelectronic devices. *Advanced materials (Deerfield Beach, Fla.)*, 23(24):2759–63, July 2011.
- [17] B. Conings, L. Baeten, C. De Dobbelaere, J. D’Haen, J. Manca, and H.-G. Boyen. Perovskite-Based Hybrid Solar Cells Exceeding 10% Efficiency with High Reproducibility Using a Thin Film Sandwich Approach. *Advanced materials (Deerfield Beach, Fla.)*, pages 1–6, Dec. 2013.
- [18] M. Dante, J. Peet, and T.-Q. Nguyen. Nanoscale Charge Transport and Internal Structure of Bulk Heterojunction Conjugated Polymer/Fullerene Solar Cells by Scanning Probe Microscopy. *Journal of Physical Chemistry C*, 112(18):7241–7249, May 2008.
- [19] P. S. Davids, I. H. Campbell, and D. L. Smith. Device model for single carrier organic diodes. *Journal of Applied Physics*, 82(12):6319, Dec. 1997.
- [20] S. Desbief, N. Hergué, O. Douhéret, M. Surin, P. Dubois, Y. Geerts, R. Lazzaroni, and P. Leclère. Nanoscale investigation of the electrical properties in semiconductor polymer-carbon nanotube hybrid materials. *Nanoscale*, 4(8):2705–12, Apr. 2012.
- [21] O. Douhéret and A. Swinnen. High-resolution morphological and electrical characterisation of organic bulk heterojunction solar cells by scanning probe microscopy. *Progress in Photovoltaics: Research and Applications*, (August):713–726, 2007.
- [22] O. Douhéret, a. Swinnen, M. Bresselge, I. Van Severen, L. Lutsen, D. Vanderzande, and J. Manca. High resolution electrical characterisation of organic photovoltaic blends. *Microelectronic Engineering*, 84(3):431–436, Mar. 2007.
- [23] C. Duan, C. Zhong, C. Liu, F. Huang, and Y. Cao. Highly efficient inverted polymer solar cells based on an alcohol soluble fullerene

BIBLIOGRAPHY

- derivative interfacial modification material. *Chemistry of Materials*, 2012.
- [24] E. Edri, S. Kirmayer, A. Henning, S. Mukhopadhyay, K. Gartsman, Y. Rosenwaks, G. Hodes, and D. Cahen. Why lead methylammonium tri-iodide perovskite-based solar cells require a mesoporous electron transporting scaffold (but not necessarily a hole conductor). *Nano letters*, 14(2):1000–4, Feb. 2014.
- [25] E. Edri, S. Kirmayer, S. Mukhopadhyay, K. Gartsman, G. Hodes, and D. Cahen. Elucidating the charge carrier separation and working mechanism of $\text{CH}_3\text{NH}_3\text{PbI}_{3-x}\text{Cl}_x$ perovskite solar cells. *Nature communications*, 5:3461, Jan. 2014.
- [26] Y. Gartstein and E. Conwell. High-field hopping mobility in molecular systems with spatially correlated energetic disorder. *Chemical physics letters*, 245(November):351–358, 1995.
- [27] T. Ghos, O. Malinkiewicz, B. Conings, L. Lutsen, D. J. Vanderzande, H. J. Bolink, and W. Maes. Solution-processed bi-layer polythiophene-fullerene organic solar cells. *RSC Advances*, 3(47):25197, 2013.
- [28] G. Grancini, S. Marras, M. Prato, C. Giannini, C. Quarti, F. De Angelis, M. De Bastiani, G. E. Eperon, H. J. Snaith, L. Manna, and A. Petrozza. The Impact of the Crystallization Processes on the Structural and Optical Properties of Hybrid Perovskite Films for Photovoltaics. *The Journal of Physical Chemistry Letters*, page 140926103112004, Sept. 2014.
- [29] G. Greczynski, T. Kugler, M. Keil, W. Osikowicz, M. Fahlman, and W. Salaneck. Photoelectron spectroscopy of thin films of PEDOT-PSS conjugated polymer blend: a mini-review and some new results. *Journal of Electron Spectroscopy and Related Phenomena*, 121(1-3):1–17, Dec. 2001.

BIBLIOGRAPHY

- [30] D. J. Griffiths. *Introduction to Quantum Mechanics 2nd edition*. Prentice Hall, 2004.
- [31] A. Hadipour, D. Cheyng, P. Heremans, and B. P. Rand. Electrode Considerations for the Optical Enhancement of Organic Bulk Heterojunction Solar Cells. *Advanced Energy Materials*, 1(5):930–935, Oct. 2011.
- [32] S. Hanni and D. Alexander. On the interplay between microstructure and interfaces in high-efficiency microcrystalline silicon solar cells. *Photovoltaics, IEEE Journal of*, 3(1):11–16, 2013.
- [33] A. Henning, G. Günzburger, R. Jöhr, Y. Rosenwaks, B. Bozic-Weber, C. E. Housecroft, E. C. Constable, E. Meyer, and T. Glatzel. Kelvin probe force microscopy of nanocrystalline TiO₂ photoelectrodes. *Beilstein journal of nanotechnology*, 4:418–28, Jan. 2013.
- [34] C. V. Hoven, R. Yang, A. Garcia, V. Crockett, A. J. Heeger, G. C. Bazan, and T.-Q. Nguyen. Electron injection into organic semiconductor devices from high work function cathodes. *Proceedings of the National Academy of Sciences of the United States of America*, 105(35):12730–5, Sept. 2008.
- [35] F. Huang, H. Wu, and Y. Cao. Water/alcohol soluble conjugated polymers as highly efficient electron transporting/injection layer in optoelectronic devices. *Chemical Society reviews*, 39(7):2500–21, July 2010.
- [36] J.-H. Im, I.-H. Jang, N. Pellet, M. Grätzel, and N.-G. Park. Growth of CH₃NH₃PbI₃ cuboids with controlled size for high-efficiency perovskite solar cells. *Nature nanotechnology*, (August):1–6, Aug. 2014.
- [37] M. C. Iovu, E. E. Sheina, R. R. Gil, and R. D. McCullough. Experimental Evidence for the Quasi-‘Living’ Nature of the Grignard Metathesis Method for the Synthesis of Regioregular Poly(3-alkylthiophenes). *Macromolecules*, 38(21):8649–8656, Oct. 2005.

BIBLIOGRAPHY

- [38] S. JEE, S. KIM, J. KO, and Y. YOON. Study on work function change of ITO modified by using a self-assembled monolayer for organic based devices. *Journal of the Korean Physical Society*, 49(5):2034–2039, 2006.
- [39] S. Jung, S. Ahn, J. H. Yun, J. Gwak, D. Kim, and K. Yoon. Effects of Ga contents on properties of CIGS thin films and solar cells fabricated by co-evaporation technique. *Current Applied Physics*, 10(4):990–996, July 2010.
- [40] I. Katsouras, a. Najafi, K. Asadi, a.J. Kronemeijer, a.J. Oostra, L. Koster, D. de Leeuw, and P. Blom. Charge transport in poly(p-phenylene vinylene) at low temperature and high electric field. *Organic Electronics*, 14(6):1591–1596, June 2013.
- [41] M. Kawamura, T. Yamada, N. Suyama, A. Yamada, and M. Konagai. Grain Boundary Evaluation of $\text{Cu}(\text{In}_{1-x}\text{Ga}_x)\text{Se}_2$ Solar Cells. *Japanese Journal of Applied Physics*, 49(6):062301, June 2010.
- [42] J. Kesters, T. Ghoo, H. Penxten, J. Drijkoningen, T. Vangerven, D. M. Lyons, B. Verreet, T. Aernouts, L. Lutsen, D. Vanderzande, J. Manca, and W. Maes. Imidazolium-Substituted Polythiophenes as Efficient Electron Transport Materials Improving Photovoltaic Performance. *Advanced Energy Materials*, Apr. 2013.
- [43] G. Y. Kim, J. R. Kim, W. Jo, D.-H. Son, D.-H. Kim, and J.-K. Kang. Nanoscale observation of surface potential and carrier transport in $\text{Cu}_2\text{ZnSn}(\text{S},\text{Se})_4$ thin films grown by sputtering-based two-step process. *Nanoscale research letters*, 9(1):10, Jan. 2014.
- [44] M. Knaapila, R. C. Evans, A. Gutacker, V. M. Garamus, N. K. Székely, U. Scherf, and H. D. Burrows. Conjugated polyelectrolyte (CPE) poly[3-[6-(N-methylimidazolium)hexyl]-2,5-thiophene] complexed with aqueous sodium dodecylsulfate amphiphile: synthesis, solution structure and 'surfactochromic' properties. *Soft Matter*, 7(15):6863, 2011.

BIBLIOGRAPHY

- [45] A. Kumatani, Y. Li, P. Darmawan, T. Minari, and K. Tsukagoshi. On practical charge injection at the metal/organic semiconductor interface. *Scientific reports*, 3:1026, Jan. 2013.
- [46] I. Lange, J. Blakesley, J. Frisch, A. Vollmer, N. Koch, and D. Neher. Band Bending in Conjugated Polymer Layers. *Physical Review Letters*, 106(21):1–4, May 2011.
- [47] J. Lee, J. Kong, H. Kim, S.-O. Kang, and K. Lee. Direct observation of internal potential distributions in a bulk heterojunction solar cell. *Applied Physics Letters*, 99(24):243301, 2011.
- [48] J. Li, V. Chawla, and B. Clemens. Understanding the role of grain boundaries in sulfide thin film solar cells with scanning probe microscopy. *Photovoltaic Specialists Conference (PVSC), 2012 38th IEEE*, pages 668–670, 2012.
- [49] a. Liscio, V. Palermo, D. Gentilini, F. Nolde, K. Müllen, and P. Samorì. Quantitative Measurement of the Local Surface Potential of π -Conjugated Nanostructures: A Kelvin Probe Force Microscopy Study. *Advanced Functional Materials*, 16(11):1407–1416, July 2006.
- [50] M. Liu, M. B. Johnston, and H. J. Snaith. Efficient planar heterojunction perovskite solar cells by vapour deposition. *Nature*, 501(7467):395–8, Sept. 2013.
- [51] M. T. Lloyd, D. C. Olson, P. Lu, E. Fang, D. L. Moore, M. S. White, M. O. Reese, D. S. Ginley, and J. W. P. Hsu. Impact of contact evolution on the shelf life of organic solar cells. *Journal of Materials Chemistry*, 19(41):7638, 2009.
- [52] R. S. Loewe, P. C. Ewbank, J. Liu, L. Zhai, and R. D. McCullough. Regioregular, Head-to-Tail Coupled Poly(3-alkylthiophenes) Made Easy by the GRIM Method: Investigation of the Reaction and the Origin of Regioselectivity. *Macromolecules*, 34(13):4324–4333, June 2001.

BIBLIOGRAPHY

- [53] S. J. Lou, J. M. Szarko, T. Xu, L. Yu, T. J. Marks, and L. X. Chen. Effects of additives on the morphology of solution phase aggregates formed by active layer components of high-efficiency organic solar cells. *Journal of the American Chemical Society*, 133(51):20661–3, Dec. 2011.
- [54] K. Maturová, S. V. Bavel, and M. Wienk. Morphological device model for organic bulk heterojunction solar cells. *Nano Letters*, (Gg 385):6–11, 2009.
- [55] K. Maturová, M. Kemerink, M. M. Wienk, D. S. H. Charrier, and R. a. J. Janssen. Scanning Kelvin Probe Microscopy on Bulk Heterojunction Polymer Blends. *Advanced Functional Materials*, 19(9):1379–1386, May 2009.
- [56] K. Maturová, S. S. van Bavel, M. M. Wienk, R. a. J. Janssen, and M. Kemerink. Description of the Morphology Dependent Charge Transport and Performance of Polymer:Fullerene Bulk Heterojunction Solar Cells. *Advanced Functional Materials*, 21(2):261–269, Jan. 2011.
- [57] W. Melitz, J. Shen, A. C. Kummel, and S. Lee. Kelvin probe force microscopy and its application. *Surface Science Reports*, 66(1):1–27, Jan. 2011.
- [58] D. Moerman, R. Lazzaroni, and O. Douheret. Efficient bulk heterojunction photovoltaic cells with a pre-organized poly(3-hexylthiophene) phase. *Applied Physics Letters*, 99(9):093303, 2011.
- [59] D. Moerman, N. Sebaihi, S. E. Kaviyil, P. Leclère, R. Lazzaroni, and O. Douhéret. Towards a unified description of the charge transport mechanisms in conductive atomic force microscopy studies of semi-conducting. pages 1–13, 2014.
- [60] D. Moerman, N. Sebaihi, S. E. Kaviyil, P. Leclere, R. Lazzaroni, and O. Douhéret. Towards a unified description of the charge transport mechanisms in conductive atomic force microscopy studies of semi-conducting polymers. *Nanoscale*, July 2014.

BIBLIOGRAPHY

- [61] V. Muller, B. Derjaguin, and Y. Toporov. On two methods of calculation of the force of sticking of an elastic sphere to a rigid plane. *Colloids and Surfaces*, 7(3):251–259, Aug. 1983.
- [62] D. Nečas and P. Klapetek. Gwyddion: an open-source software for SPM data analysis. *Central European Journal of Physics*, 10(1):181–188, Nov. 2011.
- [63] T. T. Ngo, D. N. Nguyen, and V. T. Nguyen. Glass transition of PCBM, P3HT and their blends in quenched state. *Advances in Natural Sciences: Nanoscience and Nanotechnology*, 3(4):045001, Sept. 2012.
- [64] K. Norrman. Stability/degradation of polymer solar cells. *Solar Energy Materials and Solar*, 2008.
- [65] M. Oehzelt, N. Koch, and G. Heimel. Organic semiconductor density of states controls the energy level alignment at electrode interfaces. *Nature communications*, 5(May):4174, Jan. 2014.
- [66] V. Palermo, M. Palma, and P. Samorì. Electronic Characterization of Organic Thin Films by Kelvin Probe Force Microscopy. *Advanced Materials*, 18(2):145–164, Jan. 2006.
- [67] C. H. Peters, I. T. Sachs-Quintana, J. P. Kastrop, S. Beaupré, M. Leclerc, and M. D. McGehee. High Efficiency Polymer Solar Cells with Long Operating Lifetimes. *Advanced Energy Materials*, 1(4):491–494, July 2011.
- [68] A. Pivrikas, G. Juška, R. Österbacka, M. Westerling, M. Viliunas, K. Arlauskas, and H. Stubb. Langevin recombination and space-charge-perturbed current transients in regiorandom poly(3-hexylthiophene). *Physical Review B*, 71(12):125205, Mar. 2005.
- [69] E. L. Ratcliff, B. Zacher, and N. R. Armstrong. Selective Interlayers and Contacts in Organic Photovoltaic Cells. *The Journal of Physical Chemistry Letters*, 2(11):1337–1350, June 2011.

BIBLIOGRAPHY

- [70] B. Ray and M. a. Alam. Random vs regularized OPV: Limits of performance gain of organic bulk heterojunction solar cells by morphology engineering. *Solar Energy Materials and Solar Cells*, 99:204–212, Apr. 2012.
- [71] O. G. Reid, K. Munechika, and D. S. Ginger. Space charge limited current measurements on conjugated polymer films using conductive atomic force microscopy. *Nano letters*, 8(6):1602–9, June 2008.
- [72] A. Rice, R. Giridharagopal, and S. Zheng. Controlling vertical morphology within the active layer of organic photovoltaics using Poly (3-hexylthiophene) nanowires and phenyl-C61-butyric acid methyl ester. *ACS nano*, (4):3132–3140, 2011.
- [73] Y. Rosenwaks, R. Shikler, T. Glatzel, and S. Sadewasser. Kelvin probe force microscopy of semiconductor surface defects. *Physical Review B*, 70(8):085320, Aug. 2004.
- [74] J. H. Seo, A. Gutacker, Y. Sun, H. Wu, F. Huang, Y. Cao, U. Scherf, A. J. Heeger, and G. C. Bazan. Improved high-efficiency organic solar cells via incorporation of a conjugated polyelectrolyte interlayer. *Journal of the American Chemical Society*, 133(22):8416–9, June 2011.
- [75] C. G. Shuttle, R. Hamilton, J. Nelson, B. C. O’Regan, and J. R. Durrant. Measurement of Charge-Density Dependence of Carrier Mobility in an Organic Semiconductor Blend. *Advanced Functional Materials*, 20(5):698–702, Mar. 2010.
- [76] M. K. Siddiki, S. Venkatesan, D. Galipeau, and Q. Qiao. Kelvin probe force microscopic imaging of the energy barrier and energetically favorable offset of interfaces in double-junction organic solar cells. *ACS applied materials & interfaces*, 5(4):1279–86, Feb. 2013.
- [77] F. So and D. Kondakov. Degradation mechanisms in small-molecule and polymer organic light-emitting diodes. *Advanced materials (Deerfield Beach, Fla.)*, 22(34):3762–77, Sept. 2010.

BIBLIOGRAPHY

- [78] R. Steim, F. R. Kogler, and C. J. Brabec. Interface materials for organic solar cells. *Journal of Materials Chemistry*, 20(13):2499, 2010.
- [79] A. Swinnen, I. Haeldermans, M. vande Ven, J. D'Haen, G. Vanhoyland, S. Aresu, M. D'Olieslaeger, and J. Manca. Tuning the Dimensions of C60-Based Needlelike Crystals in Blended Thin Films. *Advanced Functional Materials*, 16(6):760–765, Apr. 2006.
- [80] S. M. Sze and K. K. Ng. *Physics of Semiconductor Devices, 3rd Edition*. Wiley Online Library, 3 edition, 2006.
- [81] K. Vandewal, A. Gadisa, W. D. Oosterbaan, S. Bertho, F. Banishoeib, I. Van Severen, L. Lutsen, T. J. Cleij, D. Vanderzande, and J. V. Manca. The Relation Between Open-Circuit Voltage and the Onset of Photocurrent Generation by Charge-Transfer Absorption in Polymer:Fullerene Bulk Heterojunction Solar Cells. *Advanced Functional Materials*, 18(14):2064–2070, July 2008.
- [82] P. Vanlaeke, A. Swinnen, I. Haeldermans, G. Vanhoyland, T. Aernouts, D. Cheyns, C. Deibel, J. D'Haen, P. Heremans, J. Poortmans, and J. Manca. P3HT/PCBM bulk heterojunction solar cells: Relation between morphology and electro-optical characteristics. *Solar Energy Materials and Solar Cells*, 90(14):2150–2158, Sept. 2006.
- [83] J. Villarrubia. Morphological estimation of tip geometry for scanned probe microscopy. *Surface science*, 6028(94), 1994.
- [84] E. Voroshazi, B. Verreet, T. Aernouts, and P. Heremans. Long-term operational lifetime and degradation analysis of P3HT:PCBM photovoltaic cells. *Solar Energy Materials and Solar Cells*, 95(5):1303–1307, May 2011.
- [85] Q. Wang, Y. Zhou, H. Zheng, J. Shi, C. Li, C. Q. Su, L. Wang, C. Luo, D. Hu, J. Pei, J. Wang, J. Peng, and Y. Cao. Modifying organic/metal interface via solvent treatment to improve electron injection in organic

BIBLIOGRAPHY

- light emitting diodes. *Organic Electronics*, 12(11):1858–1863, Nov. 2011.
- [86] S. Wang and G. C. Bazan. Solvent-dependent aggregation of a water-soluble poly(fluorene) controls energy transfer to chromophore-labeled DNA. *Chemical communications (Cambridge, England)*, (21):2508–9, Dec. 2004.
- [87] Z. B. Wang, M. G. Helander, M. T. Greiner, J. Qiu, and Z. H. Lu. Analysis of charge-injection characteristics at electrode-organic interfaces: Case study of transition-metal oxides. *Physical Review B*, 80(23):235325, Dec. 2009.
- [88] S. Watanabe, Y. Fukuchi, M. Fukasawa, T. Sassa, A. Kimoto, Y. Tajima, M. Uchiyama, T. Yamashita, M. Matsumoto, and T. Aoyama. In Situ KPFM Imaging of Local Photovoltaic Characteristics on Structured Organic Photovoltaic Devices. *ACS applied materials & interfaces*, Jan. 2014.
- [89] S. a. L. Weber, N. Haberkorn, P. Theato, and R. Berger. Mapping of local conductivity variations on fragile nanopillar arrays by scanning conductive torsion mode microscopy. *Nano letters*, 10(4):1194–7, Apr. 2010.
- [90] Z. Xu, L. Chen, and M. Chen. Energy level alignment of poly (3-hexylthiophene):-phenyl C 61 butyric acid methyl ester bulk heterojunction. *Applied Physics Letters*, 95(1):013301, 2009.
- [91] Z. Xu, L.-M. Chen, G. Yang, C.-H. Huang, J. Hou, Y. Wu, G. Li, C.-S. Hsu, and Y. Yang. Vertical Phase Separation in Poly(3-hexylthiophene): Fullerene Derivative Blends and its Advantage for Inverted Structure Solar Cells. *Advanced Functional Materials*, 19(8):1227–1234, Apr. 2009.
- [92] T. Yang, M. Wang, C. Duan, X. Hu, L. Huang, J. Peng, F. Huang, and X. Gong. Inverted polymer solar cells with 8.4% efficiency by conju-

BIBLIOGRAPHY

- gated polyelectrolyte. *Energy & Environmental Science*, 5(8):8208, 2012.
- [93] L. Ying, P. Zalar, S. D. Collins, Z. Chen, A. a. Mikhailovsky, T.-Q. Nguyen, and G. C. Bazan. All-conjugated triblock polyelectrolytes. *Advanced materials (Deerfield Beach, Fla.)*, 24(48):6496–501, Dec. 2012.
- [94] H.-L. Yip and A. K.-Y. Jen. Recent advances in solution-processed interfacial materials for efficient and stable polymer solar cells. *Energy & Environmental Science*, 5(3):5994, 2012.
- [95] L. Zhai, R. L. Pilston, K. L. Zaiger, K. K. Stokes, and R. D. McCullough. A Simple Method to Generate Side-Chain Derivatives of Regioregular Polythiophene via the GRIM Metathesis and Post-polymerization Functionalization. *Macromolecules*, 36(1):61–64, Jan. 2003.
- [96] W. Zhang and Y. Chen. Experimental determination of conduction and valence bands of semiconductor nanoparticles using Kelvin probe force microscopy. *Journal of Nanoparticle Research*, 15(1):1334, Dec. 2012.
- [97] H. Zhou, Y. Zhang, J. Seifert, S. D. Collins, C. Luo, G. C. Bazan, T.-Q. Nguyen, and A. J. Heeger. High-Efficiency Polymer Solar Cells Enhanced by Solvent Treatment. *Advanced materials (Deerfield Beach, Fla.)*, pages 1646–1652, Jan. 2013.

Part III

Conclusions & Outlook

Chapter 5

Conclusions and Future Work

5.1 Conclusions

The goal of this thesis was to further investigate the applicability of advanced scanning probe microscopy on novel generation solar cells. To this end novel generation solar cells and absorber layers were investigated via recently developed atomic force microscopy techniques.

In a first step we were able to show that the contact potential difference as measured by KPFM indicates the height of the potential barrier between tip and sample. Moreover, whenever the barrier is sufficiently large, the injection mechanism changes from a space charge limited type (low barrier) and a Poole-Frenkel type injection (higher barrier). Additionally, and as expected, PEDOT:PSS has a significant influence on the surface potential and local charge transport characteristics. Moreover, Poole-Frenkel type injection appears to be valid for a plethora of different organic layers and blends.

CHAPTER 5. CONCLUSIONS AND FUTURE WORK

Secondary, we showed that the inclusion of an ionic interlayer in between blend and cathode resulted in an increase in power conversion efficiency. Moreover, a thorough study with PeakForce QNM and PeakForce TUNA showed that the interlayers studied in this work do not need full coverage to perform properly. Moreover, the local electrical properties on the best performing conjugated poly-electrolyte layer demonstrated that the interlayer effectively acts as a hole blocking layer resulting in less recombination at the cathode and thereby explaining the increase in short circuit current. Additionally illuminated kelvin probe force microscopy indicated that indeed charge transport is still taking place. Increasing device efficiencies should be possible by maintaining a limited thickness while increasing CPE coverage.

Lead halide based perovskite layers for photovoltaic conversion are easily characterized by AFM. KPFM substantiates that the surface potential is uniform over different grains and thereby confirming the existence of a phase pure material. In addition illuminated KPFM shows that band bending does show, however, not at all grain boundaries. From conductive AFM it can be discerned that different grains display a different current at a fixed applied bias. This difference could be the result of a bad interaction between the perovskite absorber and the TiO_2 layer or could be due to recombination within the grains. Moreover, C-AFM explicates that grain boundaries show no discernible conduction at a positive and negative bias. The negative effect of the grain boundaries suggests that reducing the boundaries should result in increased device efficiencies.

Finally we have established the validity of kelvin probe force microscopy as a tool to study the local degradation of the cathode in organic solar cells. A first foray in linking the local reduction in surface potential of the cathode to the reduced V_{oc} by annealing has been demonstrated. The results as obtained by KPFM and SEM illustrate clearly that increased annealing temperatures have a significant impact on local composition and

this effect is mainly due to the calcium and not due to local oxidation.

To me, this work beautifully illustrates the applicability and endless possibilities of advanced AFM techniques for (organic) solar cells.

5.2 Future Work

5.2.1 C-AFM on blends

In this work the injection model was determined to behave as a Poole-Frenkel type injection, however, no attempt was made on a more thorough analysis of the local current-voltage curves as this requires an extensive knowledge of the trap density in the material. A possible solution would be to attempt Monte Carlo simulations to describe the local charge transport from tip to sample taking into account both the offset in energy level between tip and sample and the hopping assisted transport. In addition it would extremely useful to be able to characterize both conductive AFM and KPFM at the same time, if current developments in AFM technology are any indication, this should be possible within the next five to ten years.

5.2.2 Interlayers

As seen in the sections on interlayers, the best functioning CPE layers do not cover the complete surface, in this case the suggestion can be made that the interlayer might act as an optical spacer. First steps towards using topography as obtained by AFM in a simulation for optical properties have been made, however, the results do not confirm nor deny any advantageous optical effects. However, as newly measured interlayers have different morphologies with height differences up to 50 nm an optical effect is very well possible. In addition it would be extremely useful to study the electrical properties of the interlayers using photoconductivity measurements as this would confirm any additional photo-current from the

interlayer, however, this would have to be done with a tip coated with a low work function metal as the interlayers are most easily processed in a standard device architecture.

5.2.3 SPM and Perovskites

Conductive AFM showed that the perovskite as analysed in this work demonstrates different conduction through different grains, the mechanism as to why is not yet completely clear. A possible route would be the use of piezoresponse force microscopy as it is well known that certain perovskites show a piezoelectric behaviour. Additionally it would be extremely useful to be able to study the local ferro-electrical properties.

5.2.4 Contact degradation

In this work contact degradation was studied with KPFM, however, extremely useful would be the ability to study the contact by simply lifting of the contact from the organic layer. A first attempt at this was made, however, none of the tapes used was able to lift of the metallic layer.

5.2.5 Illuminated KPFM

An added benefit to illuminated KPFM, as illustrated in this work, would be the ability to do spectral resolved measurements. First attempts at this were made, however, the light intensity attainable in our lab is not high enough to have an adequately measurable signal with KPFM. This problem first existed with photo-conductive AFM but was resolved by illuminating at the backside with intensities of around 300-400 sun, a similar trick for illuminated KPFM should resolve any problems related to intensity.

Part IV

Appendix

Appendix A

Experimental Details

Charge injection and extraction in Polymer/Donor:acceptor blends

Patterned ITO substrates (15 Ohm/sq, Jinfung Limited, China) were cleaned according to the following subsequent steps: sonication in soap solution, water, acetone and boiled in isopropanol. Each individual cleaning step lasted 10 minutes. The ITO substrates were thereafter treated with UV-O₃ for 15 mins to improve the wetting properties. A subset of the samples was coated with ~30 nm PEDOT:PSS (Heraeus Clevios) and annealed at 130°C for 15 min. to remove any residual moisture from the film. P3HT (Rieke Metals, Mw = 66kD and 93% regioregularity) was dissolved in ODCB with or without PCBM (Solenne) to obtain the following P3HT:PCBM ratio's: pure P3HT, 1:1, 2:1, 1:2 and pure PCBM. The P3HT(:PCBM) films were slow dried for an hour at room temperature and annealed for 10 mins at 110°C to get the optimal morphology. PCDTBT:PC₇₁BM, (PC₇₁BM from Solenne) was dissolved in ODCB to get solutions with PCDTBT:PC₇₁BM ratios of 1:1, 1:2, 1:4 and 1:8. The PTB7 was obtained from SolarisChem and used as delivered, PTB7:PC₇₁BM was dissolved in ODCB with DIO and spincoated to obtain films of ~80 nm. The DTPQx donor polymer was synthesised according to the method proposed by Vanormelingen^[4] and spincoated from chloroform. The thickness of the layers was measured by dektak. All

AFM measurements (Multimode 8 - V series controller, Bruker) were done in an inert atmosphere with a relative humidity less than 3%. The Kelvin Probe measurements were done using Pt/Ir coated tips (SCM-PIT: $k = 4$ N/m, Bruker) at a lift scan height of 10 nm at an AC bias of 3V. The conductive AFM measurements were done using Pt/Ir coated tips (PF-TUNA: $k = 0.4$ N/m, Bruker) with a deflection setpoint of 0.4 V and at current sensitivities between 10 pA/V and 100 pA/V depending on the voltage range. All presented IV curves were averaged from 5 different curves taken at a single location. The cathode of the devices consisted of 30 nm of calcium and 80 nm of aluminium, evaporated sequentially on the active layer.

Imidazolium-substituted polythiophenes as efficient electron transport materials

Synthesis of conjugated polyelectrolytes: Trimethylamine-functionalized polythiophene **P1 (P3(TMA)HT-Br)** (Figure 4.15), used as a reference interlayer material, was prepared by a literature procedure as reported by Bazan et al.^[5] Imidazolium-substituted polythiophenes P2 and P3 were prepared according to a recently reported method.^[1] Details on the synthetic procedures and characterization data are provided in the Supporting Information of a manuscript by Kesters et al.^[2]

Device fabrication: The reference BHJ solar cells were constructed using the traditional glass/ITO/PEDOT-PSS/active layer/Ca/Al architecture. To investigate the impact of the CPE layers, the Ca layer was replaced by a CPE. A control device without CPE or Ca layer was included as an additional reference. Before device processing, the indium tin oxide (ITO, Kintec, 100 nm, 20 Ohm/sq) containing substrates were cleaned using soap, demineralized water, acetone, isopropanol and a UV/O₃ treatment. Subsequently, the ITO substrates were covered by a ~30 nm thick layer of PEDOT-PSS (Heraeus Clevis) by spin-coating. Further processing was performed under nitrogen atmosphere in a glove box, starting off with an

annealing step at 130 °C for 15 min to remove any residual water. The PCDTBT donor polymer was obtained from SolarisChem ($M_n = 79$ kDa, $D = 2.4$), and used as received. PCPDT-DTTzTz was synthesized according to a previously reported method.^[1] The active layer consisting of PCDTBT:PC₇₁BM ([6,6]-phenyl C71 butyric acid methyl ester, Solenne) was spin-coated with a thickness of ~65 nm (as confirmed by DEKTAK). Blend solutions were prepared in a 1:4 ratio, with PCDTBT concentrations of 5 mg/mL, using chlorobenzene:1,2-dichlorobenzene (1:3) as a solvent mixture.^[3] For the devices containing PCPDT-DTTzTz:PC₇₁BM as the active layer, a thickness of ~70 nm was obtained through spin-coating. Blend solutions were prepared in a 1:3 ratio, with PCPDT-DTTzTz concentrations of 5 mg/mL, using chlorobenzene as a solvent.^[1] The active layer deposition step was followed by spin-coating of the CPE interlayers, aiming for thicknesses of ~5-10 nm. The CPE solutions were prepared in concentrations of 0.01, 0.02 and 0.04 w/v% in methanol. Finally, the devices were finished off with Al as the top electrode, with a thickness of ~80 nm. Thicknesses of the top electrodes of the reference device containing Ca/Al were ~ 20 and 80 nm, respectively. In the standard cell configuration, an active area of 25 mm² was obtained. To provide a better assessment of the value of the in-house prepared CPE's, the more commonly used interlayer material PFN (poly[(9,9-bis(3'-(N,N-dimethylamino)propyl)-2,7-fluorene)]) was used as well.

Device characterization: The PCEs of the BHJ solar cells were measured using a Newport class A solar simulator (model 91195A) calibrated with a silicon solar cell to give an AM 1.5g spectrum. For AFM imaging, a Bruker Multimode 8 AFM was used in PeakForce tapping mode, employing PeakForce QNM. The images were produced with a silicon tip on a nitride lever with a spring constant of 4 N m⁻¹.

EQE and reflection measurements: A commercial set-up (Bentham) was used to measure the EQE. Light from a Xe arc lamp (300-670 nm) and a

quartz halogen lamp (670-900 nm) is chopped, coupled into a monochromator and aimed at the device. The resulting current is sent through a Bentham477 current pre-amplifier, then arriving in the Bentham485 lock-in amplifier. Calibration is done with a certificated Si cell. The integration of these EQEs over the solar spectrum is listed in Table 4.9 as J_{EQE} . The same optics and measurement setup is used with a DTR6 integrating sphere to determine the reflection.

Nanoscale morphological and electrical properties of interlayers

Sample fabrication: all samples were fabricated using a standard glass - ITO - PEDOT:PSS - active layer layout, without the traditional aluminum top contact. The indium tin oxide (ITO, Kintec, 100 nm, 20 Ω /sq) containing substrates were cleaned using soap, demineralized water, acetone, isopropanol and a UV/O₃ treatment. Subsequently, the ITO substrates were covered by a 30 nm thick layer of PEDOT-PSS (Heraeus Clevis) by spin coating. Processing was performed in a glovebox with a controlled nitrogen atmosphere, starting with an annealing step at 130°C for 15 min to remove any residual water. The PCDTBT donor polymer was obtained from SolarisChem ($M_n = 79$ kDA, $D = 2.4$) and used without further purification. The active layer consisting of PCDTBT:PC₇₁BM (PC₇₁BM, Solenne) with an in blend ratio of 1 to 4 was spin coated with a thickness of 65 nm, as confirmed by DEKTAK. The active layer deposition step was followed by spin coating of the conjugated polyelectrolyte (CPE) interlayer. The CPE solution was prepared in a concentration of 0.02% in methanol.

This procedure led to a set of three different samples: a reference sample with only the active layer deposited on ITO covered glass, a methanol treated active layer on ITO covered glass and a CPE coated active layer on ITO covered glass. All of the samples were kept in an inert nitrogen atmosphere at all times.

Measurements were done on a Bruker Multimode 8 atomic force microscope in combination with a V series controller. The AFM is enclosed in a glovebox allowing for a controlled atmosphere with a maximum relative humidity of 6%. KPFM imaging was done using the surface potential setting on the AFM with long platinum/iridium coated cantilevers with a force constant of 4 N/m and a lift scan height of 7 to 15 nm. Peak-Force TUNA/QNM measurements were done using a soft conducting platinum/iridium cantilever with a force constant of 0.4 N/m.

A standard solar simulator with a xenon arc lamp was used during KPFM imaging. The light was fed into the glovebox via a high grade optical fibre, which reduced the intensity by 50 % over the visible spectrum. The light from the optical fibre was calibrated using a standard reference silicon solar cell.

All images were analysed using the NanoScope Analysis software.

Advanced scanning probe microscopy for perovskite based solar cells

Patterned ITO substrates (15 Ohm/sq, Jinfung Limited, China) were cleaned according to the following subsequent steps: sonication in soap solution, water, acetone and boiled in isopropanol. Each individual cleaning step lasted 10 minutes. The ITO substrates were thereafter treated with an O₂ plasma (50W, 3 min at 0.5 mbar). The TiO₂ blocking layer was deposited by spincoating a TiO₂ precursor at 3000 rpm for 30s, followed by 3 consecutive heating steps of 2 min. at 180°C, 2 min. at 300°C and 1 hour at 500°C. The substrates were hereafter transferred to a nitrogen filled glovebox. The perovskite precursor, as prepared according to (ref bert), 10 ml of hydroiodic acid (57% in water, sigma) was added dropwise to 24 ml of methylamine (33% in absolute ethanol, Sigma) and 100 ml ethanol under nitrogen atmosphere. A rotary evaporator was used to remove the solvent

and crystallize methyammonium iodide (MAI). The precipitate was washed with diethyl ether three times. The resulting white powder was hereafter dried on a hotplate at 65°C for 6h in air. MAI and PbCl₂ (Alfa, 99.999%) were dissolved in dimethyl sulfoxide (Sigma) in seperate vials and then mixed to obtain a precursor solution with a MAI:PbCl₂ molar ratio of 3:1. Subsequent AFM analysis was done on a Bruker Multimode 8 AFM with a V series controller in an inert atmosphere with a relative humidity < 6%. Kelvin Probe Force Microscopy measurements were done using Pt/Ir coated tips (SCM-PIT, Bruker), with a quoted force constant of 4 N/m and an electrical excitation of 3 V and a lift scan height of 15 nm. The conductive AFM measurements were done using Pt/Ir coated tips (PF-TUNA, Bruker) with a quoted force constant of 0.4 N/m at a maximum deflection setpoint of 0.3V and a current sensitivity of 100 pA/V. The illuminated KPFM measurements we done using a solar simulator (Newport) with a xenon lamp to amount to an irradiation intensity of 1 sun (as confirmed by a silicon reference cell) through a high quality optical fiber.

Visualizing thermally and atmospheric induced degradation of the cathode in polymer solar cells

Sample fabrication: all samples were fabricated using a standard glass - ITO - PEDOT:PSS - active layer layout. To this end patterned ITO substrates (15 Ohm/sq, Jinfung Limited, China) were cleaned according to the following subsequent steps: sonication in soap solution, water, acetone thereafter boiled in isopropanol and a subjected to an UV/O₃ treatment. Each individual cleaning step lasted 15 minutes. The ITO on glass substrates were then coated with ~30 nm PEDOT:PSS (Heraeus Clevios) and annealed at 130°C for 15 min. to remove any residual moisture from the film. P3HT (Rieke Metals, Mw = 66kD and 93% regioregularity) was dissolved in ODCB together with PCBM (Solenne) to obtain P3HT:PCBM in a 0.9:1 ratio. The films were thereafter slow dried for an hour at room temperature and annealed for 10 mins at 110°C to get the optimal morphology.

BIBLIOGRAPHY

The PCEs of the BHJ solar cells were measured using a Newport class A solar simulator (model 91195A) calibrated with a silicon solar cell to give an AM 1.5g spectrum. All AFM measurements (Multimode 8 - V series controller, Bruker) were done in an inert atmosphere with a relative humidity less than 6% unless otherwise stated. The Kelvin Probe measurements were done using Pt/Ir coated tips (SCM-PIT: $k = 4 \text{ N/m}$, Bruker) at a lift scan height of 10 nm at an AC bias of 3V. The SEM-EDX study has been performed with a Philips XL-30 FEG-SEM. The EDX detector is a Si(Li) detector, relevant acceleration voltages are mentioned in the corresponding text.

Bibliography

- [1] T. Ghoo, O. Malinkiewicz, B. Conings, L. Lutsen, D. J. Vanderzande, H. J. Bolink, and W. Maes. Solution-processed bi-layer polythiophene-fullerene organic solar cells. *RSC Advances*, 3(47):25197, 2013.
- [2] J. Kesters, T. Ghoo, H. Penxten, J. Drijkoningen, T. Vangerven, D. M. Lyons, B. Verreet, T. Aernouts, L. Lutsen, D. Vanderzande, J. Manca, and W. Maes. Imidazolium-Substituted Polythiophenes as Efficient Electron Transport Materials Improving Photovoltaic Performance. *Advanced Energy Materials*, Apr. 2013.
- [3] J. H. Seo, A. Gutacker, Y. Sun, H. Wu, F. Huang, Y. Cao, U. Scherf, A. J. Heeger, and G. C. Bazan. Improved high-efficiency organic solar cells via incorporation of a conjugated polyelectrolyte interlayer. *Journal of the American Chemical Society*, 133(22):8416–9, June 2011.
- [4] W. Vanormelingen, J. Kesters, P. Verstappen, J. Drijkoningen, J. Kudrjasova, S. Koudjina, V. Liégeois, B. Champagne, J. Manca, L. Lutsen, D. Vanderzande, and W. Maes. Enhanced open-circuit voltage in polymer solar cells by dithieno[3,2-b:2',3'-d]pyrrole N-acylation. *Journal of Materials Chemistry A*, 2(20):7535, Apr. 2014.

BIBLIOGRAPHY

- [5] S. Wang and G. C. Bazan. Solvent-dependent aggregation of a water-soluble poly(fluorene) controls energy transfer to chromophore-labeled DNA. *Chemical communications (Cambridge, England)*, (21):2508–9, Dec. 2004.

